ORNL/TM-2019/1119

Development of Nanoprecipitates-Strengthened Advanced Ferritic Alloys for Nuclear Reactor Applications

OAK RIDGE NATIONAL LABORATORY
MANAGED BY UT BATTELLE
FOR U.S. DEPARTMENT OF ENERGY

Lizhen Tan
Tianyi Chen
Ying Yang
Oak Ridge National Laboratory

Li He
Kumar Sridharan
University of Wisconsin-Madison

Approved for public release.
Distribution is unlimited.

February 28, 2019

OAK RIDGE NATIONAL LABORATORY
MANAGED BY UT-BATTELLE FOR THE US DEPARTMENT OF ENERGY

DOCUMENT AVAILABILITY

Reports produced after January 1, 1996, are generally available free via US Department of Energy (DOE) SciTech Connect.

Website www.osti.gov

Reports produced before January 1, 1996, may be purchased by members of the public from the following source:

National Technical Information Service
5285 Port Royal Road
Springfield, VA 22161
Telephone 703-605-6000 (1-800-553-6847)
TDD 703-487-4639
Fax 703-605-6900
E-mail info@ntis.gov
Website http://classic.ntis.gov/

Reports are available to DOE employees, DOE contractors, Energy Technology Data Exchange representatives, and International Nuclear Information System representatives from the following source:

Office of Scientific and Technical Information
PO Box 62
Oak Ridge, TN 37831
Telephone 865-576-8401
Fax 865-576-5728
E-mail reports@osti.gov
Website http://www.osti.gov/contact.html

This report was prepared as an account of work sponsored by an agency of the United States Government. Neither the United States Government nor any agency thereof, nor any of their employees, makes any warranty, express or implied, or assumes any legal liability or responsibility for the accuracy, completeness, or usefulness of any information, apparatus, product, or process disclosed, or represents that its use would not infringe privately owned rights. Reference herein to any specific commercial product, process, or service by trade name, trademark, manufacturer, or otherwise, does not necessarily constitute or imply its endorsement, recommendation, or favoring by the United States Government or any agency thereof. The views and opinions of authors expressed herein do not necessarily state or reflect those of the United States Government or any agency thereof.

ORNL/TM-2019/1119
M2CA-15-TN-OR0402025

FY 2015 Consolidated Innovative Nuclear Research (CINR)
Nuclear Energy Enabling Technologies (NEET): Reactor Materials

DEVELOPMENT OF NANOPRECIPITATES-STRENGTHENED ADVANCED FERRITIC ALLOYS FOR NUCLEAR REACTOR APPLICATIONS

Lizhen Tan, Tianyi Chen, Ying Yang
Oak Ridge National Laboratory

Li He, Kumar Sridharan
University of Wisconsin-Madison

Date Published: February 28, 2019

Prepared by
OAK RIDGE NATIONAL LABORATORY
Oak Ridge, TN 37831-6283
managed by
UT-BATTELLE, LLC
for the
US DEPARTMENT OF ENERGY
under contract DE-AC05-00OR22725

CONTENTS

LIST OF FIGURES v
LIST OF TABLES ix
ACKNOWLEDGMENTS xi
EXCUTIVE SUMMARY xiii
1. INTRODUCTION 1
2. METHODS AND EXPERIMENTS 2
    2.1 COMPUTATIONAL ALLOY DESIGN 2
    2.2 EXPERIMENTAL METHODS 4
        2.2.1 Alloy fabrication 4
        2.2.2 Mechanical tests 5
        2.2.3 Microstructural characterization 6
        2.2.4 Ion irradiation 6
        2.2.5 Other 7
3. ALLOY DOWN-SELECTION 8
    3.1 FERRITIC ALLOYS 8
    3.2 FERRITIC-MARTENSITIC STEELS 10
    3.3 ALLOY DOWN-SELECTION 10
    3.4 DOWN-SELECTED ALLOYS 13
4. MECHANICAL PROPERTIES OF DOWN-SELECTED ALLOYS 14
    4.1 TENSILE PROPERTIES 14
    4.2 CHARPY IMPACT TOUGHNESS 15
    4.3 CREEP RESISTANCE 15
    4.4 SUMMARY 17
5. MICROSTRUCTURAL CHARACTERIZATION OF DOWN-SELECTED ALLOYS 18
    5.1 REFERENCE ALLOY T91 18
    5.2 ALLOY BL-Nb 19
    5.3 ALLOY TTZ2M 24
    5.4 ALLOYS FTT1 and FTN1 25
    5.5 SUMMARY 28
6. ION IRRADIATION OF DOWN-SELECTED ALLOYS 29
    6.1 DEFOCUSED BEAM 29
        6.1.1 Fe^{2+} irradiation at 350°C 29
        6.1.2 Fe^{2+} irradiation at 475°C 31
    6.2 RASTERING BEAM 33
    6.3 NANOINDENTATION 35
    6.4 MICROSTRUCTURES 36
        6.4.1 FTN1 (NA) irradiated at 350°C 36
        6.4.2 FTT1 (TA) irradiated at 350°C 37
        6.4.3 T91 irradiated at 350°C 38
        6.4.4 FTN1 (NA) irradiated at 475°C 39
        6.4.5 FTT1 (TA) irradiated at 475°C 40
        6.4.6 T91 irradiated at 475°C 40
        6.4.7 TTZ2M irradiated at 475°C (rastering beam) 40
        6.4.8 BL-Nb irradiated at 475°C (rastering beam) 41
    6.5 SUMMARY 45
7. CONCLUSIONS 47
REFERENCES 49
Appendix A. PUBLICATIONS 50

LIST OF FIGURES

Figure 1. Calculated liquidus surfaces of (a) Fe-Cr-Zr and (b) Fe-Ni-Zr systems. 2

Figure 2. Isopleth sections in the Fe-Cr-Ni-Zr system with (a) fixed Cr at 13 at% and Zr at 33.3 at%; (b) fixed Cr at 13 at% and Ni at 5 at%. 3

Figure 3. Fe-12Cr-Ni-Zr isothermal section at 1000 °C (black lines) and 700 °C (red lines) with the symbols denoting four alloys of Fe-12Cr-3Zr-3.3Ni, Fe-12Cr-3Zr-6.5Ni, Fe-12Cr-6Zr-4.5Ni, and Fe-12Cr-6Zr-9Ni to be experimentally studied......................................3

Figure 4. (a) BF-TEM image of Z3N7 aged at 700°C for 1275 h and representative SAED patterns of (b) Fe_2Zr_C15, (c) Fe-Cr matrix, (d) Ni_7Zr_2, and (e) $Fe_{23}Zr_6$ phases.............................4

Figure 5. Geometry of type SS-3 miniature specimens for tensile and creep tests.......................................5

Figure 6. Geometry of half-size Charpy specimen for impact toughness testing. 6

Figure 7. Temperature-dependent dilatometer determined phase transformation temperatures of FTN1 (NA) and FTT1 (TA)......................................7

Figure 8. Calculated temperature-dependent phase fractions in five designed ferritic alloys of (a) Z2N13, (b) Z1N33A, (c) BL-NbZr, (d) BL-Nb, and (e) BL-Mo.....................................9

Figure 9. Calculated temperature-dependent phase fractions in three designed 9Cr ferritic-martensitic steels of (a) 53T1, 63T1, and TTZ2M, compared with (b) a commercial T91 heat. 10

Figure 10. Vickers hardness (HV1) results of ferritic alloys Z2N13, Z1N33A, BL-NbZr, BL-Nb, BL-Mo and ferritic-martensitic steels 53T1, 63T1, and TTZ2M. 11

Figure 11. Temperature-dependent (a) yield strength and (b) total elongation of ferritic alloys Z2N13, Z1N33A, BL-NbZr, BL-Nb, BL-Mo and ferritic-martensitic steels 53T1, 63T1, and TTZ2M, compared with T91......................................11

Figure 12. Creep life of ferritic alloys Z1N33A, BL-NbZr, BL-Nb, BL-Mo and ferritic-martensitic steels 53T1, 63T1, and TTZ2M tested at 650°C and 120 MPa..................................12

Figure 13. Radiation hardening measured by nanoindentation at a depth of 1 μm for ferritic alloys Z2N13, Z1N33A, BL-NbZr, BL-Nb, BL-Mo and ferritic-martensitic steels 53T1, 63T1, and TTZ2M irradiated with Fe2+ up to 220 dpa at 350 and 475°C. 13

Figure 14. Temperature-dependent (a) yield strength, (b) tensile strength, (c) uniform elongation, and (d) total elongation of the ferritic (BL-Nb) and ferritic-martensitic (TTZ2M, FTN1, and FTT1) steels, compared to literature data of T91. FTN1-T and FTT1-T are a heat-treated version of FTN1 and FTT1, respectively. 14

Figure 15. Temperature-dependent Charpy absorbed energy of the ferritic (BL-Nb) and ferritic-martensitic (TTZ2M, FTN1, FTT1, and the heat-treated version FTN1-T and FTT1-T) steels, compared to literature data of Grade 91 heat 30176. 15

Figure 16. Creep strain-time curves for the down-selected alloys BL-Nb, TTZ2M, FTN1, and FTT1 compared with T91 tested at 650°C and 120 MPa (dashed) and 100 MPa (solid)...............16

Figure 17. Stress-dependent minimum creep rates of alloys BL-Nb, TTZ2M, FTN1, and FTT1 compared with T91 tested at 650°C......................................17

Figure 18. (a-c) HAADF images of the tab-section T91 creep-tested at 650°C and 100 MPa and (d-f) EDS maps of (c). 18

Figure 19. BF-STEM images with the [001] zone from the gauge section of T91 creep-tested at 650°C and (a) 120 and (b) 100 MPa. 19

Figure 20. (a) BF-STEM and (b) HAADF images near the [001] zone of the bcc matrix in the gauge section of the BL-Nb sample creep-tested at 650°C and 100 MPa. 19

Figure 21. (a) BF-STEM and (b) HAADF images near the [001] zone of the bcc matrix in the gauge section of the BL-Nb sample creep-tested at 650°C and 100 MPa. 20

Figure 22. (a) BF and (b-d) DF TEM images in the gauge section of the BL-Nb sample creep-tested at 650°C and 100 MPa. 20

Figure 23. (a) A SAED pattern obtained from the matrix of the as-received sample. (b) A DF-TEM image of the coherent precipitates. The EDS mappings of (c) Ni and (d) Al of the as-received sample, and the Ni mappings from the (e) thermal-aged and (f) deformed regions of the 120 MPa creep sample, and the (g) thermal-aged and (h) deformed regions of the 100 MPa creep sample. 21
Figure 24. Time-dependent radius (R) in cubic power of B2-NiAl particles under the thermal aging and stressed conditions at 650°C. 22
Figure 25. EDS analyzed relative Ni-Al ratio of B2-NiAl particles at the as-received condition and the 650°C aged and stressed conditions. 22
Figure 26. Laves phase precipitates in the bcc matrix presented in (a) BF-TEM image, (b) SAED pattern of the [**111**] zone of the matrix, (c-d) DF-TEM images using the spots marked by the circle and square in (b), respectively 23
Figure 27. Laves phase precipitates presented in: (a) and (d) HAADF images, (b) and (e) EDS mapping of Nb, and (c) and (f) EDS mapping of W, for (a-c) the as-received condition and (d-f) the 1852-hour thermal-aged and stressed condition. 23
Figure 28. The evolution of W-Nb atomic ratio in the Laves precipitates. 24
Figure 29. (a) BF- and (b) DF-TEM images showing the microstructure and precipitate distributions in the as-received TTZ2M alloy. 24
Figure 30. (a-c) HAADF images of TTZ2M creep-tested at 650°C and 100 MPa and (d) EDS map of (c). 25
Figure 31. BF-STEM images imaged with the [001] zone from the gauge section of TTZ2M creep-tested at 650°C and (a) 120 and (b) 100 MPa. 25
Figure 32. Optical micrographs of (a) FTT1 and (b) FTN1 and their heat-treated version (c) FTT1-T and (d) FTN1-T. 26
Figure 33. Optical micrograph of FTN1-T showing overall grain structure. 26
Figure 34. Creep-tested FTT1 at 650°C and 100 MPa: (a) BF-TEM image at the tab section, (b) BF-TEM image at the gauge section, (c) DF-TEM image at the gauge section, and (d) BF-STEM image at the gauge section. 27
Figure 35. 3.7 MeV iron induced damage and implanted iron concentration in FTN1 (NA), FTT1 (TA), T91 (red). The damage and implantation depth profiles were calculated using the Kinchin-Pease Model in the SRIM software. *Ed* is atom displacement energy. 29
Figure 36. Temperature and flux during 3.7 MeV iron 350°C irradiation. (a) Irradiation run 1 of FTT1 (TA); (b) Irradiation run 2 of FTN1 (NA) and T91. 30
Figure 37. Samples after 350°C, 250 dpa Fe^{2+} irradiation. (a) Run 1 of FTT1 (TA). (b) Run 2 of T91 and FTN1 (NA). Arrows indicate irradiation boundary. The lower part of T91 and upper part of FTN1 (NA) are irradiated. 30
Figure 38. Al implantation in the 350°C irradiated FTN1 (NA) and T91 samples. ABF images of cross-sectional (a) FTN1 (NA) and (b) T91 with the red lines illustrating the EDS line scan paths for the (c) EDS depth profile and SRIM calculated Al composition from surface. 31
Figure 39. Temperature and flux during 3.7 MeV iron 475 °C irradiation. (a) Irradiation run 3 of FTT1 (TA). (b) Irradiation run 4 of FTN1 (NA) and T91. 32
Figure 40. Samples after 475 °C, 250 dpa Fe^{2+} irradiation: (a) FTT1 (TA); (b) FTN1 (NA); (c) T91. Arrows indicate irradiation area. 32
Figure 41. (a) Cross-sectional ABF image and (b) EDS line scan profile across the red line in (a) of Fe^{2+}-irradiated FTN1 (NA) up to 250 dpa at 475°C showing Cu-rich particles at ~1.1 µm depth. 33
Figure 42. 4 MeV iron induced damage in BL-Nb (79Fe-12Cr-3W-3Ni-3Al). The damage and implantation profiles were calculated using the Kinchin-Pease Model in the SRIM software. *Ed* is atom displacement energy. 34
Figure 43. Temperature and flux during 4 MeV iron irradiation (a) run 1 and (b) run 2 of BL-Nb 34

Figure 44. Nanoindentation hardness of ion-irradiated samples: defocused-beam up to 250 dpa at 350°C for (a) FTN1 (NA) and (b) T91 and at 475°C for (c) FTN1 (NA) and (d) T91; rastered-beam up to 220 dpa at 475°C for (e) TTZ2M and (f) BL-Nb. 35
Figure 45. Cross-sectional ABF images of FTN1 (NA) after 350ºC ion irradiation: (a) Overview and (b) Damaged region at 0.54 μm depth with normal direction parallel to [100]. 36
Figure 46. Precipitates in FTN1 (NA): (a) Undamaged region with the arrow-pointed 1 as $(Cr,W)_{23}C_6$ and 2 as a Ti, W, Nb-rich carbide; (b) Damaged region at 0.54 μm showing the particles of $M_{23}C_6$. 37
Figure 47. Cross-sectional ABF images of FTT1 (TA) after 350°C ion irradiation: (a) Overview and (b) Damaged region at 0.5 μm depth with normal direction parallel to [100]. 37
Figure 48. DF image showing MX type precipitates in FTT1 (TA) after 350°C ion irradiation at 0.6 μm depth. 38
Figure 49. Cross-sectional ABF images of T91 after irradiation at 350°C: (a) Overview and (b) Dislocation loops under <111> zone at an irradiation depth of 0.55 μm. 38
Figure 50. Precipitates in T91. (a) Undamaged. (b) 350 °C irradiation damaged region. 1 is $M_{23}C_6$. 2 is V, Nb-rich MX. 39
Figure 51. Cross-sectional ABF images of FTN1 (NA) irradiated at 475°C: (a) Overview of damaged (top part) and undamaged structure; (b) <100> dislocation loops at 0.55 μm depth. 39
Figure 52. Cross-sectional ABF images of FTT1 (TA) irradiated at 475°C: (a) Overview of damaged (top part) and undamaged structure; (b) Dislocation loops at 0.7 μm depth and (c) corresponding SAED pattern. 40
Figure 53. Cross-sectional HAADF image of T91 irradiated at 475°C along the <111> zone. Arrow indicates damage depth. 40
Figure 54. TTZ2M irradiated at 475°C along the <111> zone: (a) BF-TEM overview image and (b-c) ABF-STEM images at ~0.6 μm depth. 41
Figure 55. B2-NiAl precipitates in the unirradiated region: (a) DF-TEM image from the [100] zone as indicated in the electron diffraction pattern of the inset, (b) HAADF image, and (c) EDS line scan compositional profiles across the particle pointed by the arrow in (b). 41
Figure 56. Images of B2-NiAl particles in the irradiated region: DF-TEM images at (a) 0.15–0.6 μm depth and (b) 1.15–1.6 μm depth. The images were taken with the $(001)_{NiAl}$ diffraction from the [100] zone axis as shown in the inset of (a); (c) HAADF image at 0.86 μm from surface with the inset of an FFT of the original image. 42
Figure 57. TEM characterization of BL-Nb after Fe^{2+} ion irradiation at 475°C: (a-b) Cross-sectional ABF images along <100>; (c) Nanobeam SAED pattern of particle A in (b) with red and blue circles indicating matrix and particle diffraction spots, respectively; (d) EDS measured compositional profile along particle B in (b). 43
Figure 58. TEM characterization of irradiated particles in BL-Nb after Fe^{2+} ion irradiation at 475°C: (a) ABF image along <100> with the image center at 1.2 μm depth (~200 dpa); (b) ABF image along <100> with the image center at 0.83 μm depth (~164 dpa); (c-d) EDS peak intensity profile along the arrow line cross the damaged particle in (b). Dashed and solid arrows in (c) indicate widths of particle and core, respectively. 44
Figure 59. Irradiation induced particles. (a) ABF image at 0.9 μm depth, about 180 dpa. (b) EDS peak intensity profile along the arrow in (a). (c) HAADF image of a particle at 0.78 μm depth, about 150 dpa. 44
Figure 60. TEM characterization of a partially damaged micron-scale particle: (a) ABF image showing a contrast line inside the particle, as indicated by two short white arrows, at 1.5 μm depth (~30 dpa near the end of damage range); (b) Nanobeam electron diffraction patterns of points A and B labeled in (a); (c) EDS measured compositional profile along red arrow line in (a), with a dashed line indicating the ABF contrast line location. 45

LIST OF TABLES

Table 1. Designed ferritic alloys. 8
Table 2. Designed ferritic-martensitic steels...10
Table 3. Down-selected steels and reference steel. 13
Table 4. Minimum creep rates (h^{-1}) of the designed alloys compared to T91 tested at 650°C. 16
Table 5. Mean size of Laves phase under different conditions at 650°C...23

ACKNOWLEDGMENTS

This research was sponsored by the U.S. Department of Energy (DOE), Office of Nuclear Energy (NE), the Nuclear Energy Enabling Technologies (NEET) program, Reactor Materials FY 2015 Award. We gratefully acknowledge the support provided by Sue Lesica of DOE-NE and Stuart Maloy of Los Alamos National Laboratory.

The authors are grateful to Tom Geer, Douglas Stringfield, Dorothy Coffey, Gregory Cox, and Eric Manneschmidt of Oak Ridge National Laboratory (ORNL) for sample preparation and mechanical testing. Kevin Field and Xiang Chen of ORNL are appreciated for technical review of this report.

EXCUTIVE SUMMARY

By using the experimentally justified and optimized thermodynamic database, five ferritic steels and three ferritic-martensitic steels were designed for property screening, including Vickers hardness, tensile, creep, and radiation hardening, which led to the down-selection of one ferritic steel (BL-Nb) and one ferritic-martensitic steel (TTZ2M) for further investigation. Based on the TTZ2M, two large-scale ferritic-martensitic heats, i.e., FTT1 and FTN1, were produced at an industrial steelmaking facility, which are in contrast to the small laboratory heats BL-Nb and TTZ2M. Other than the standard normalization and tempering condition of the ferritic-martensitic steels, a heat-treated condition was explored for the FTT1 and FTN1, which is named as FTT1-T and FTN1-T, respectively. Two-step aging was applied to BL-Nb to favor the precipitation of Laves and B2-NiAl phases. Tensile, Charpy impact, and creep tests were conducted on the samples of the steels in air, using a commercial heat of T91 as a reference. Microstructural characterization was primarily conducted using transmission electron microscopy and energy dispersive x-ray spectroscopy with occasional uses of optical microscopy and scanning electron microscopy.

Alloys BL-Nb, TTZ2M, FTN1, and FTT1 exhibited noticeable enhancements in strength, Charpy impact toughness, and creep resistance compared to T91, except for BL-Nb having significantly lower impact toughness than T91. For example, the new alloys showed up to ~170–350 MPa increases in yield/tensile strength than T91 at test temperatures of ~23–700°C. The heat-treated condition FTT1-T and FTN1-T exhibited comparable mechanical properties, with slightly lower strength but noticeably higher Charpy impact toughness than their standard condition.

Microstructure characterizations of the creep-ruptured samples indicated noticeable recovery of T91 with diminished lath/block/packet sub-structures and reduced dislocations. In contrast, the large number of B2-NiAl and Laves $Fe_2(W,Nb)$ engineered in BL-Nb and the high-density of ultrafine Ti-rich precipitates in TTZ2M and FTT1 helped retain their sub-structures and dislocations during the creep tests. The creep of FTN1 is still running, which is expected to have more of the beneficial precipitates because of its lower minimum creep rate and longer creep life than FTT1. The refined grains (~10 μm) in the untested FTN1-T and FTT1-T compared to the larger prior-austenite grains (≥ ~50 μm) of the standard condition would explain the enhanced Charpy impact toughness of the heat-treated condition with compromised yield/tensile strength and creep resistance.

FTN1 and FTT1 showed comparable radiation resistance, superior to T91 irradiated under the same conditions at 350 and 475°C to a peak dose of 250 dpa, in terms of stabilities of grain structures, dislocations, precipitates, and radiation-hardening. For example, noticeably diminished martensitic sub-boundaries, formation of Z-phase by transformation from MX precipitates, and the greatest radiation-hardening were observed in T91. Although a direct comparison between the rastered-beam (TTZ2M and BL-Nb) and defocused-beam (FTN1, FTT1, and T91) irradiated samples is not available, the radiation resistance of TTZ2M and BL-Nb was not significantly different from the FTN1 and FTT1. However, BL-Nb did show instability of Lave phase, e.g., amorphization of coarse Laves precipitates and disintegration of fine (~100 nm) Laves precipitates to form ultrafine (~8 nm) Cr/Nb-rich particles.

In summary, the large-scale industrial heats FTN1 and FTT1 showed comparable or superior mechanical properties compared with the small laboratory heat TTZ2M, which suggest the property sustainability and scale-up fabrication feasibility of the developed ferritic-martensitic steels. The systematic study indicates the successful development of the new ferritic-martensitic steels FTN1 and FTT1 for reactor applications, which have performance noticeably superior to T91.

1. INTRODUCTION

Advanced nuclear reactors as well as the life extension of light water reactors require advanced alloys capable of satisfactory operations up to neutron damage levels approaching 200 displacements per atom (dpa) [1]. Extensive studies, including fundamental theories, have demonstrated the superior resistance to radiation-induced swelling in ferritic-martensitic (FM) and ferritic steels, primarily inherited from their body-centered cubic (bcc) structure [2]. However, the use of the FM or ferritic steels is rendered difficult due to their poorer creep strengths at temperatures higher than ~600°C. Another crucial problem of FM and ferritic steels is pronounced matrix hardening when irradiated at low temperatures ($<0.3T_m$, melting temperature), leading to an increase in the ductile to brittle transition temperature (DBTT) and a decrease in the fracture toughness. Therefore, the purpose of this project is to develop advanced ferritic alloys, which contain a high number-density of novel nanoprecipitates with a strong tendency to amorphization, to achieve significantly enhanced radiation resistance and high temperature strength. Two pathways were pursued to achieve the goal.

The first pathway is implemented by Laves phase with a high amorphization tendency. In our previous work [3], novel Fe-Cr-Zr ferritic alloys strengthened by Fe_2Zr-based Laves phase precipitates showed superior strength, ductility, and creep resistance at high temperatures, however, a consistent improvement on their radiation resistance data has yet to be achieved. Preliminary self-ion irradiation at 400°C exhibited amorphization of some phases in the Fe-Cr-Zr ferritic alloys. With the high amorphization tendency of Laves phase, other types of precipitates such as B2-NiAl and general MX (M=metal, X=C/N) were engineered into the new alloys. The second pathway follows the general 9Cr FM steel guideline to modify alloy compositions for increased densities of fine precipitates.

After routine screening of the microstructures, basic mechanical properties such as tensile, Charpy impact toughness, and creep resistance, and self-ion (Fe^{2+}) irradiation studies, a few alloys have been down-selected for detailed property and microstructure studies to understand the evolution of Laves and other types of precipitates and their influence on properties. To demonstrate the producibility and result repeatability, two of the alloys were fabricated at an industrial facility.

This report summarizes the work of this project, which describes the methods and experiments used in this project, reports the alloy down selection activities, and details the mechanical properties, microstructural characterization, and ion irradiation results of the down-selected alloys.

2. METHODS AND EXPERIMENTS

2.1 COMPUTATIONAL ALLOY DESIGN

The selection of alloying elements and the design of experimental alloy compositions were aided by computational thermodynamics. The essence of computational thermodynamics, i.e., the CALPHAD (CALculation of PHAse Diagram) approach [4], was to construct phase diagrams of multicomponent systems based on well assessed thermodynamic functions of Gibbs energy of phases. In the prior NEET project, a thermodynamic database containing major elements of Fe, Cr, Zr and minor elements of Mo, W, Si, Nb, C was developed and validated by experimental data [5]. Nickel was also included in this database but needs to be further validated by experimental data. This database was used as a starting point for alloy design. The experimental data generated from these alloys in this project were used to validate the calculated results.

Computational screening on isopleth of Fe_2Zr–Fe_2X (X=Mo, W, and Nb) found all these alloying elements increase the liquidus temperature of Fe_2Zr. In contrast, Ni addition into the Fe-Cr system decreases the liquidus temperature of Fe_2Zr [6]. The major difference between Ni and other alloying elements such as Mo, Nb and W is that the former mainly substitutes the Fe in the first sublattice while the others substitute the Zr in the second sublattice. Therefore, Ni was selected as an element that has potential to promote the amorphous forming ability of Fe_2Zr. Based on the preliminary Fe-Cr-Zr-Ni database, we calculated the liquidus surface of the Fe-Cr-Zr and Fe-Ni-Zr and compared them side by side in Figure 1a and b. The results suggest the Fe-Ni-Zr liquidus surface is more suppressed than that of Fe-Cr-Zr.

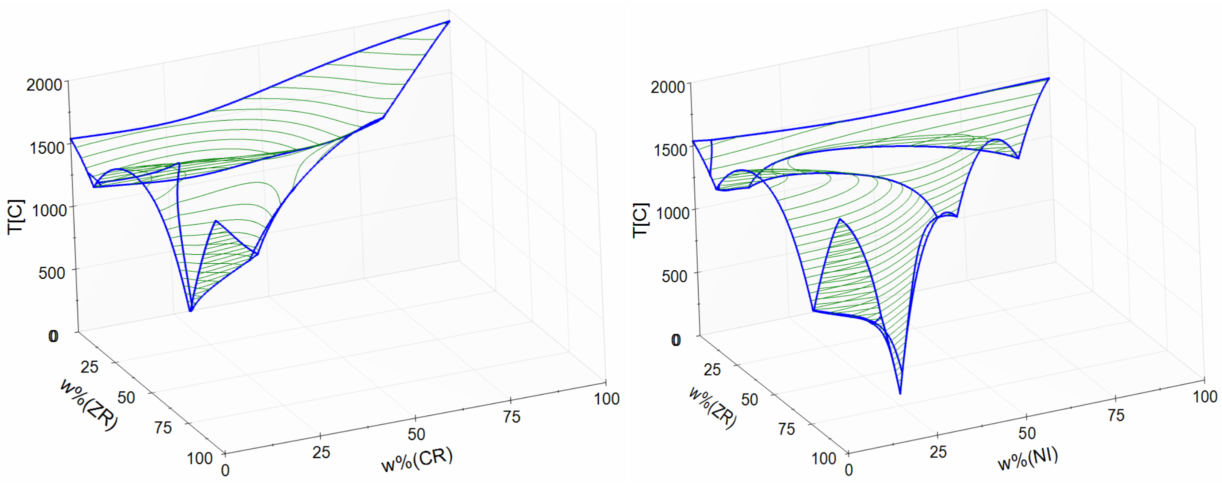

Figure 1. Calculated liquidus surfaces of (a) Fe-Cr-Zr and (b) Fe-Ni-Zr systems.

While it is difficult to visualize the liquidus surface in a quarternary system, we can plot different isopleth sections to see how Ni affects the liquidus surface. Two isopleth section in the Fe-rich region were calculated and plotted in Figure 2a and b. One is the isopleth section with fixed Zr concentration at 33.3 at%. This isopleth essentially plots the phase diagram along M_2Zr (M=Fe,Cr, Ni) direction. We also need to fix another variable to obtain the 2D diagram. The Cr concentration is fixed at 12 wt%, as this amount of Cr is desired to reach desirable corrosion resistance. The results indicate when increasing Ni concentration, the temperature of liquidus surface is decreasing. The second isopleth plots the phase diagram with fixed Cr and Ni concentration, in which a deep eutectic between Bcc(Fe) and Laves_C15 presents. Thermodynamic calculation suggests that adding Ni to the Fe-Cr-Zr alloy suppresses the liquidus surface in Fe-rich region, thus fulfills our design goal. However, these results are exclusively from calculation. We need to validate the calculation results from experiments. Isothermal sections of Fe-Cr-Ni-

Zr at 1000 and 700°C were calculated with fixed Cr concentration at 12 wt%. The calculated results are shown in Figure 3 with the red line denoting phase boundaries at 700°C, and the black line for 1000 °C. Four alloy compositions close to the phase boundary were selected for experimental study including isothermal annealing at 1000 and 700 °C. Annealing at two temperatures can help us to get an idea how stable the phase boundary vs temperature and whether to introduce an entropy term when modeling the Gibbs energy function.

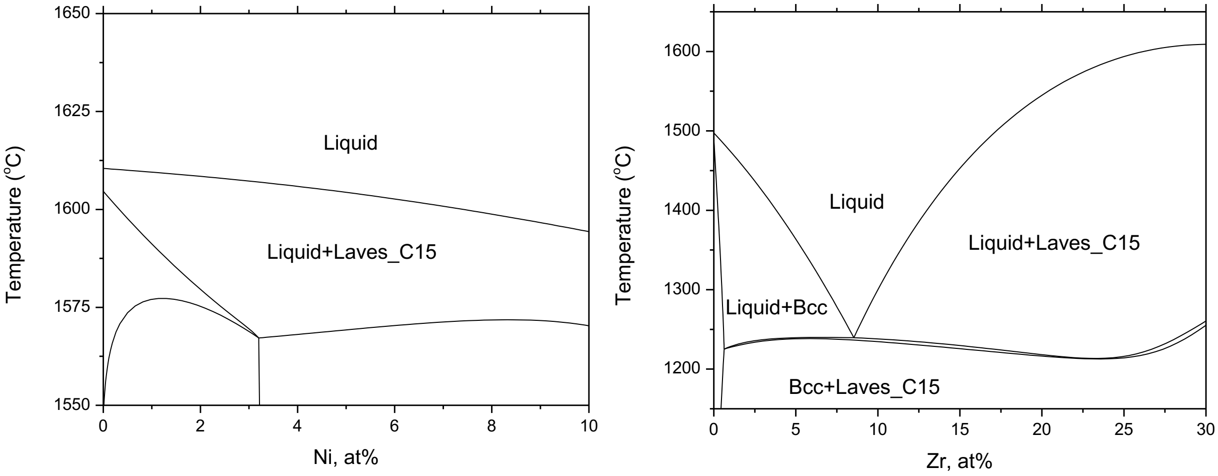

Figure 2. Isopleth sections in the Fe-Cr-Ni-Zr system with (a) fixed Cr at 13 at% and Zr at 33.3 at%; (b) fixed Cr at 13 at% and Ni at 5 at%.

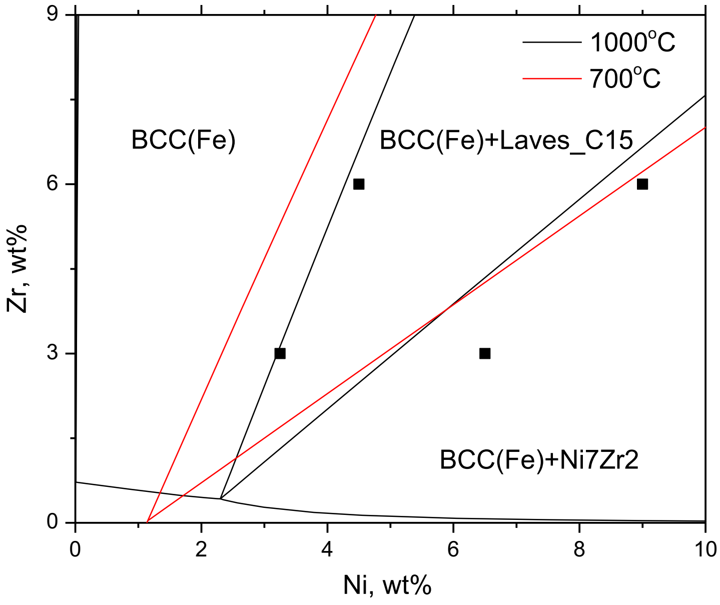

Figure 3. Fe-12Cr-Ni-Zr isothermal section at 1000 °C (black lines) and 700 °C (red lines) with the symbols denoting four alloys of Fe-12Cr-3Zr-3.3Ni, Fe-12Cr-3Zr-6.5Ni, Fe-12Cr-6Zr-4.5Ni, and Fe-12Cr-6Zr-9Ni to be experimentally studied.

As suggested in Figure 3, four ferritic alloys, named as Z3N4 (Fe-12Cr-3Zr-3.3Ni), Z3N7 (Fe-12Cr-3Zr-6.5Ni), Z6N5 (Fe-12Cr-6Zr-4.5Ni), and Z6N9 (Fe-12Cr-6Zr-9Ni), were fabricated by vacuum arc-melting to investigate the effect of Ni and Zr content on phase stability. The microstructures of the as-cast materials were compared with that of the aged conditions at 700°C for 1275 h and 1000°C for 336 h. Scanning electron microscopy (SEM), transmission electron microscopy (TEM), and energy dispersive x-ray spectroscopy (EDS) characterizations revealed the morphology, fraction, and composition of $(Fe,Ni)_2Zr$, $(Fe,Ni)_{23}Zr_6$, and $(Ni,Fe)_7Zr_2$ precipitates in the matrix of the four alloys. Figure 4 shows an example of alloy Z3N7 after 1275 h aging at 700°C in a bright-field (BF) TEM image with selected area electron diffraction (SAED) patterns of the three types of precipitates and the matrix in a body-centered cubic (bcc) structure.

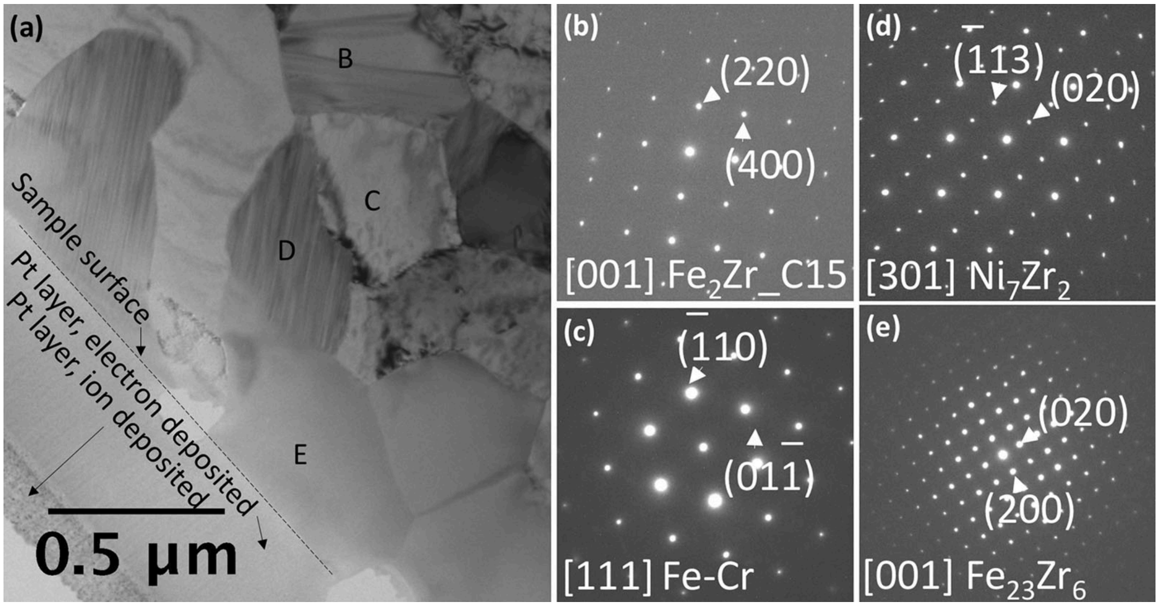

Figure 4. (a) BF-TEM image of Z3N7 aged at 700°C for 1275 h and representative SAED patterns of (b) Fe_2Zr_C15, (c) Fe-Cr matrix, (d) Ni_7Zr_2, and (e) $Fe_{23}Zr_6$ phases.

The experiments indicated extensive solubility of Ni in the intermetallic phases $Fe_{23}Zr_6$ and Fe_2Zr_C15. It was also found that Ni stabilizes the Laves Fe_2Zr_C15 structure more than the C36 and C14 structures. This work suggested that the phase equilibrium in the Fe-rich Fe-Cr-Ni-Zr system is featured by large solubilities of Ni in Fe_2Zr_C15, $Fe_{23}Zr_6$, and Fe in Ni_7Zr_2, as well as the coexistence of the three phases of bcc (matrix) + Fe_2Zr_C15 + $Fe_{23}Zr_6$ [6,7]. After the experimental verification and modification, the thermodynamic database was used to calculate temperature-dependent phase fractions to design specific alloys for property screening, which are presented in the next section.

2.2 EXPERIMENTAL METHODS

2.2.1 Alloy fabrication

Small laboratory heats of experimental alloys were fabricated by vacuum arc-melting and casting into ingots with a size of 2.5 cm × 2.5 cm × ~12 cm using a water-cooled copper mold, which were subjected to hot rolling to ~0.8 cm thick "plates" at temperatures above 1050°C, and finally annealed, tempered or aged at specific temperatures, guided by respective thermodynamic calculations of the alloys.

After down-selection, two large scale heats, named as FTN1 and FTT1 with a size of 7.6 cm × 15.2 cm × ~38 cm, were fabricated by vacuum induction melting at an industrial facility, which hot-rolled to 1.9 cm at 1150°C, followed by annealing at 1170°C for 30 min and tempering at 750°C for 30 min with air cooling.

2.2.2 Mechanical tests

Mechanical tests of the designed steels include tensile, Charpy impact, and creep. Type SS-3 miniature specimens with a gauge section of 7.62 × 1.52 × 0.76 mm were machined from the steels for tensile and creep tests, with the specimen length aligned with the longitudinal direction of the alloy heats. Half-size Charpy V-notch specimens with a size of 5 × 5 × 25.4 mm and a 1-mm deep 45° V-notch at the length center were machined from the steels in the transverse–longitudinal orientation. The geometries of type SS-3 miniature specimen and half-size Charpy specimen are shown in Figure 5 and Figure 6, respectively.

- Tensile tests were conducted in air using shoulder loading at a crosshead-controlled strain rate of 0.001 s^{-1} from room temperature up to 800°C in accordance with the American Society of Testing and Materials (ASTM) Standard E8/E8M-13a (*Standard Test Methods for Tension Testing of Metallic Materials*) and E21/E21M-09 (*Standard Test Methods for Elevated Temperature Tension Tests of Metallic Materials*).
- Charpy impact tests were performed in air on a Tinius Olsen Charpy 300 ft-lb machine according to the ASTM Standard E23-12c (*Standard Test Methods for Notched Bar Impact Testing of Metallic Materials*). Measurement validation of the Charpy machine was performed on an annual basis through testing of specimens with certified values to verify the accuracy of the machine; the certified specimens were obtained from the National Institute of Standards and Technology (NIST).
- Creep tests were conducted in air using shoulder load primarily at 650°C with different loads, following the ASTM Standard E139-11 (*Standard Test Methods for Conducting Creep, Creep-Rupture, and Stress-Rupture Tests of Metallic Materials*). Creep strains were monitored with extensometers attached to the shoulders of the specimens.

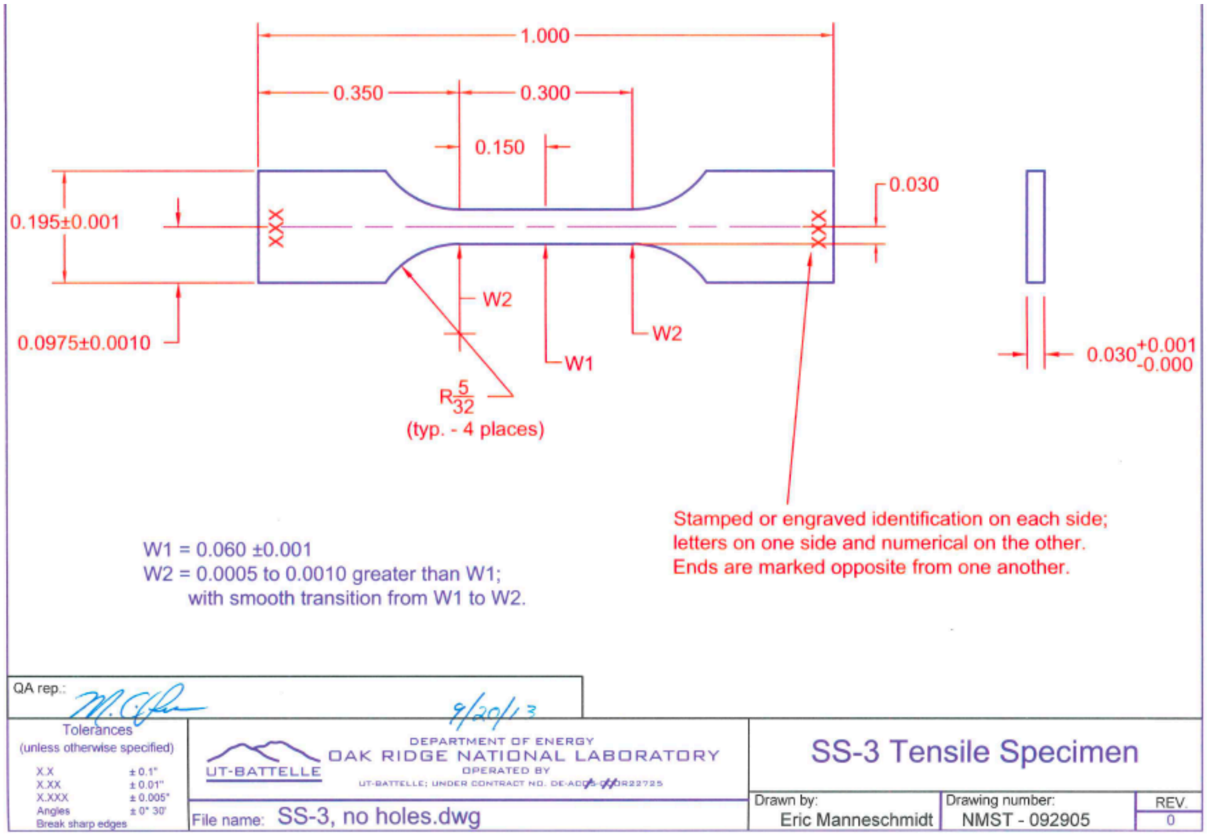
1.000
0.350
0.300
0.150
0.030
0.195±0.001
0.0975±0.0010
W2
W2
W1
R5/32
(typ. - 4 places)
0.030 +0.001 -0.000
Stamped or engraved identification on each side; letters on one side and numerical on the other.
Ends are marked opposite from one another.
W1 = 0.060 ±0.001
W2 = 0.0005 to 0.0010 greater than W1; with smooth transition from W1 to W2.
QA rep.:
9/20/13
Tolerances (unless otherwise specified)
X.X ± 0.1"
X.XX ± 0.01"
X.XXX ± 0.005"
Angles ± 0° 30'
Break sharp edges
UT-BATTELLE
DEPARTMENT OF ENERGY
OAK RIDGE NATIONAL LABORATORY
OPERATED BY
UT-BATTELLE; UNDER CONTRACT NO. DE-AC05-00OR22725
File name: SS-3, no holes.dwg
SS-3 Tensile Specimen
Drawn by: Eric Manneschmidt
Drawing number: NMST - 092905
REV. 0

Figure 5. Geometry of type SS-3 miniature specimens for tensile and creep tests.

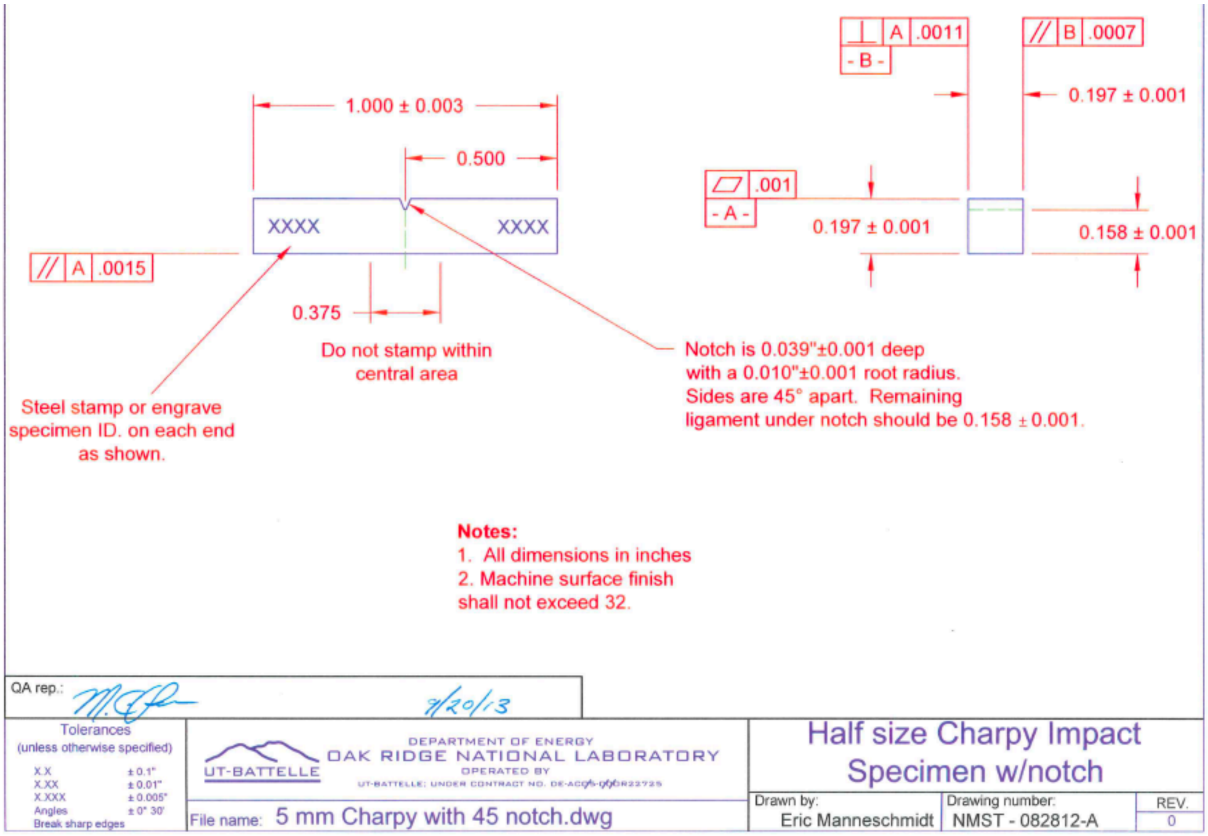
⊥ A .0011
- B -
// B .0007
0.197 ± 0.001
1.000 ± 0.003
0.500
▱ .001
- A -
0.197 ± 0.001
0.158 ± 0.001
XXXX
XXXX
// A .0015
0.375
Do not stamp within central area
Notch is 0.039"±0.001 deep with a 0.010"±0.001 root radius. Sides are 45° apart. Remaining ligament under notch should be 0.158 ±0.001.
Steel stamp or engrave specimen ID. on each end as shown.
Notes:
1. All dimensions in inches
2. Machine surface finish shall not exceed 32.
QA rep.: 9/20/13
Tolerances (unless otherwise specified)
X.X ± 0.1"
X.XX ± 0.01"
X.XXX ± 0.005"
Angles ± 0° 30'
Break sharp edges
UT-BATTELLE
DEPARTMENT OF ENERGY
OAK RIDGE NATIONAL LABORATORY
OPERATED BY
UT-BATTELLE; UNDER CONTRACT NO. DE-AC05-00OR22725
File name: 5 mm Charpy with 45 notch.dwg
Half size Charpy Impact Specimen w/notch
Drawn by: Eric Manneschmidt
Drawing number: NMST - 082812-A
REV. 0

Figure 6. Geometry of half-size Charpy specimen for impact toughness testing.

2.2.3 Microstructural characterization

TEM and EDS were primarily employed to investigate the as-received, mechanically tested, and ion-irradiated samples. Both conventional and scanning TEM, i.e., CTEM and STEM, imaging techniques were used, which produce BF, dark-field (DF), high-angle annular dark-field (HAADF) images, together with SAED and fast Fourier transform (FFT) patterns for crystallographic identification. As will be detailed later, such investigation provides insight understanding of the roles of precipitates in strengthening the materials. Focus-ion beam (FIB) technique was used to prepare electron transparent lamellae for TEM characterization. Two TEM lamellae were lifted out from each creep-ruptured sample, with one lamella from the gauge section (~1.2 mm away from the fracture end) to represent the microstructure evolved to the steady-state deformation and the other lamella from the tab section considered as stress-free thermally aged condition. Other than FIB-TEM/EDS, optical microscopy and SEM were occasionally used.

2.2.4 Ion irradiation

Self-ion (Fe^{2+}) irradiation experiments were conducted at the ion beam lab of the University of Wisconsin-Madison. The irradiation experiments were primarily performed at 350 and 475°C with a nominal peak damage up to 250 dpa. The selection of 350°C was to evaluation low-temperature radiation hardening because more radiation defects, e.g., dislocation loops, tend to form at lower temperatures. The selection of 475°C was to evaluate swelling as well as radiation hardening because the peak swelling temperature for ferritic and ferritic-martensitic steels was reported around this temperature. Rastering ion beam was mainly used in the alloy down-selection process for the small laboratory heats. However, defocused ion beam was employed for the large-scale industrial heats FTN1 and FTT1 in the latest irradiation experiments because literatures reported that rastering beam could suppress radiation-induced swelling.

Post-irradiation examinations were conducted through nanoindentation measurements and microstructural characterization. Nanoindentation was conducted at room temperature on the ion-irradiated samples as well as their unirradiated counterparts to evaluate radiation-induced hardening.

2.2.5 Other

Dilatometry using Dynamic Systems Inc. Gleeble System 3500 was used to determine phase transformation temperatures of the two large-scale industrial heats FTN1 and FTT1, with simplified names of NA and TA, respectively, as shown in Figure 7.

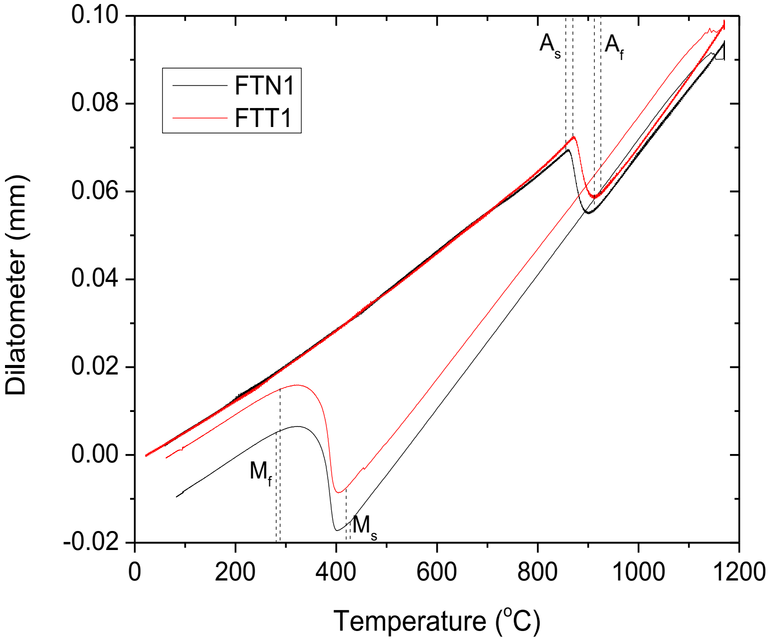

Figure 7. Temperature-dependent dilatometer determined phase transformation temperatures of FTN1 (NA) and FTT1 (TA).

Other than the standard heat treatment condition described in Section-2.2.1, a special heat treatment was applied to part of alloys FTN1 (NA) and FTT1 (TA) and designated as FTN1-T and FTT1-T, respectively, by two cycles of 15 min annealing at 970°C followed by water quench after the standard normalization and before the final tempering. The annealing temperature was ~50°C above the austenite finish temperature (A_f or Ac3) determined by Gleeble dilatometry with the test results of NA and TA as shown in Figure 7. The brief secondary annealing is believed to be able to refine grain size by converting martensitic packet and also likely block boundaries into austenitic grain boundaries.

3. ALLOY DOWN-SELECTION

3.1 FERRITIC ALLOYS

The previous study of ferritic alloys with a high Zr content, e.g., alloy Z6 (9Cr-1W-11Zr), showed noticeably improved high-temperature strength and creep resistance but deteriorated room-temperature ductility and toughness, attributable to the high Zr content [8]. Therefore, the Zr content was significantly reduced in the new alloys. The designed new ferritic alloys with nominal compositions in wt% are listed in Table 1, which were screened in this project. By using the recently developed thermodynamic database [5,6], the temperature-dependent phase fraction in the alloys was calculated.

Table 1. Designed ferritic alloys.

Alloy ID	Nominal composition in wt% (with Fe balance)
Z2N13	12Cr-3W-1Ni-1.5Zr
Z1N33A	12Cr-3W-3Ni-3Al-1Zr
BL-NbZr	12Cr-3W-3Ni-3Al-1Nb-0.15Zr
BL-Nb	12Cr-3W-3Ni-3Al-1Nb
BL-Mo	12Cr-3W-3Ni-3Al-1Mo

Figure 8 shows the calculated results of the ferritic alloys listed in Table 1, which have a ferrite (α) matrix. Alloy Z2N13 in Figure 8a shows primarily conventional C14-type Laves phase because of the presence of W and the C15-type Laves phase because of the decent amount of Zr, together with a small amount of austenite (γ) in a narrow temperature window. In contrast, the addition Al with increased amount of Ni leads to the formation of B2-phase, e.g., NiAl, in Z1N33A (Figure 8b), BL-NbZr (Figure 8c), BL-Nb (Figure 8d), and BL-Mo (Figure 8e), which does not have austenite (γ). Comparing the effect of Zr on phase stability in Figure 8a-c, it suggests that a small amount of Zr would stabilize Ni_7Zr_2, e.g., BL-NbZr, while a larger amount of Zr tends to preferentially stabilize C15-type Laves.

The ferritic alloys were primarily solution-annealed at 1200°C for 10 min in argon atmosphere and hot-rolled at 1000–1100°C with 75% thickness reduction, followed by air cooling. The Z1N33A, BL-NbZr, BL-Nb, and BL-Mo were subjected to an aging at 650°C for 5 h, followed by air cooling, to favor B2-NiAl precipitates formation.

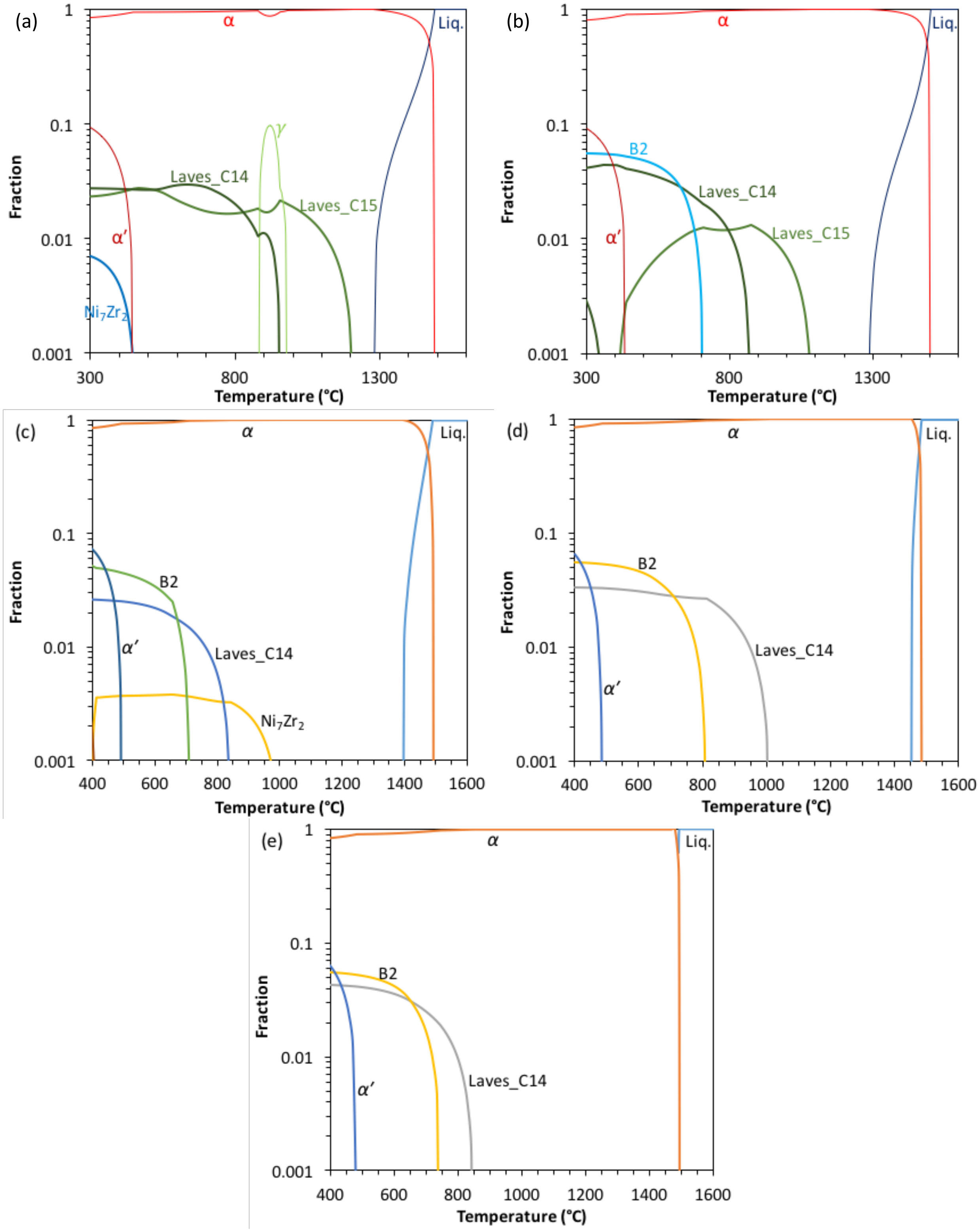

Figure 8. Calculated temperature-dependent phase fractions in five designed ferritic alloys of (a) Z2N13, (b) Z1N33A, (c) BL-NbZr, (d) BL-Nb, and (e) BL-Mo.

3.2 FERRITIC-MARTENSITIC STEELS

Three 9Cr ferritic-martensitic steels were designed, with analyzed compositions listed in Table 2. The analyzed compositions of the steels have varied atomic ratios of C/(Ti+Ta) to be ~3.8 for 53T1 (i.e., heat 91TT), ~2.1 for 63T1 (i.e., heat 91TTa), and ~2.2 for TTZ2M. In comparison, a standard T91, e.g., Fe-8.4Cr-0.9Mo-0.45Mn-0.28Si-0.21Ni-0.22V-0.08Nb-0.1C-0.05N, has an atomic ratio (C+N)/(V+Nb) of ~2.3. The analyzed compositions of 53T1 and 63T1 had the content of Ti and C significantly deviated from the designed compositions.

Table 2. Designed ferritic-martensitic steels.

Alloy ID	Analyzed composition in wt% (with Fe balance)
53T1 (91TT)	8.6Cr-1.3W-0.1Ti-0.15V-0.1Ta-0.13C
63T1 (91TTa)	8.6Cr-1.3W-0.15Ti-0.15V-0.1Ta-0.1C
TTZ2M	8.6Cr-1.4W-0.1Ti-0.1V-0.05Nb-0.1C

The calculated temperature-dependent phase fractions in the steels are shown in Figure 9. In contrast to the reference steel T91 in Figure 9b with the formation of Z-phase, e.g., Cr(V,Nb)N, to be transformed from the MX (M=V/Nb, X=C/N) phase, the three designed steels in Figure 9a do not have Z-phase because of the lack of nitrogen in the new steels. The varied C/(Ti+Ta) ratios primarily lead to the different fractions of MX (M=Ti/Ta, X=C) phase and the different austenite temperature window.

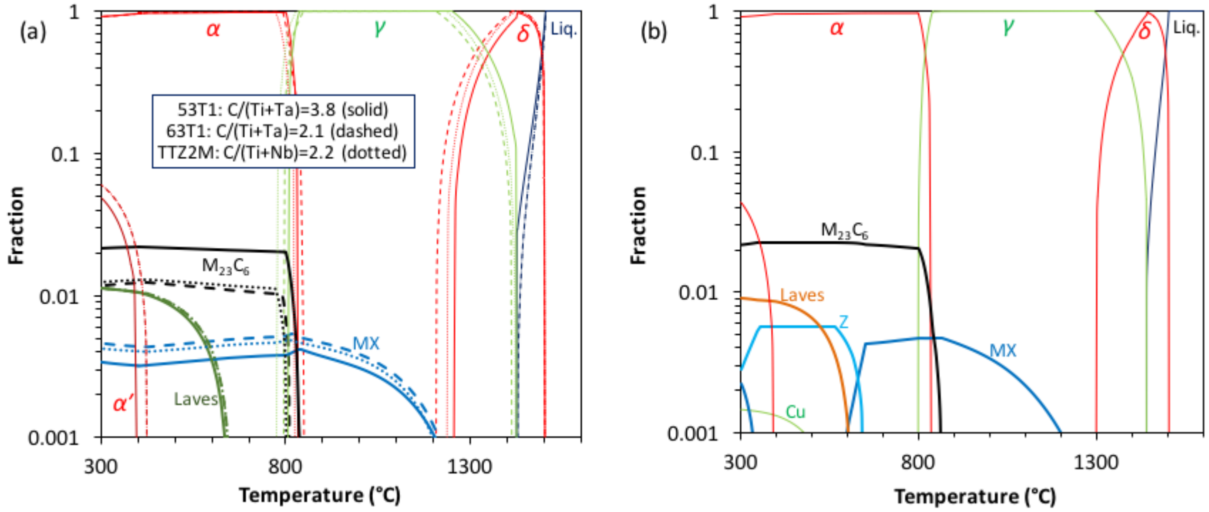

Figure 9. Calculated temperature-dependent phase fractions in three designed 9Cr ferritic-martensitic steels of (a) 53T1, 63T1, and TTZ2M, compared with (b) a commercial T91 heat.

The ferritic-martensitic steels were solution annealed at 1130°C for 50 min in reducing atmosphere, and then hot-rolled at 1100°C to 70% thickness reduction, finally normalized at 1100°C for 20 min followed by tempering at 750°C for 30 min with air cooling.

3.3 ALLOY DOWN-SELECTION

Vickers hardness (Figure 10), tensile property (Figure 11), creep resistance (Figure 12), and radiation hardening (Figure 13) of the designed ferritic alloys and ferritic-martensitic steels were screened for alloy down-selection. The ferritic alloys, except for alloy Z2N13, showed generally greater Vickers hardness than the ferritic-martensitic steels. Alloys BL-Nb and TTZ2M exhibited the greatest Vickers hardness for the ferritic and ferritic-martensitic alloys, respectively.

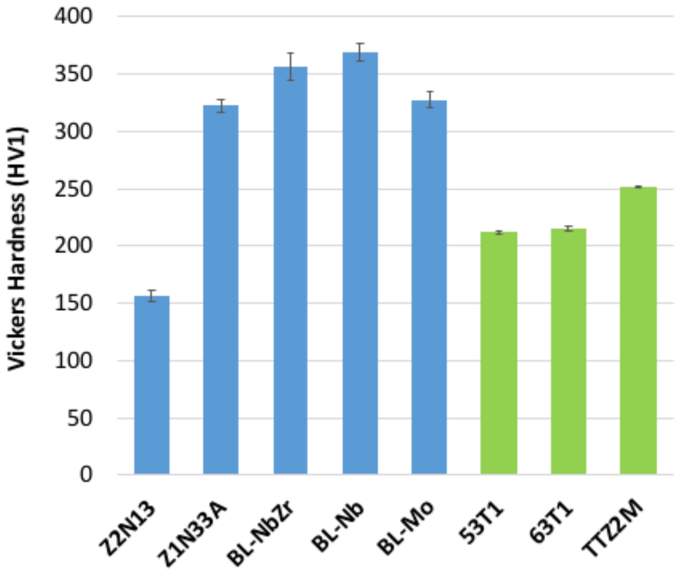

Figure 10. Vickers hardness (HV1) results of ferritic alloys Z2N13, Z1N33A, BL-NbZr, BL-Nb, BL-Mo and ferritic-martensitic steels 53T1, 63T1, and TTZ2M.

Generally consistent with the relative Vickers hardness results, the lowest hardness of alloy Z2N13 showed the lowest yield strength as shown in Figure 11a. The greater hardness of alloys BL-NbZr and BL-Nb led to the highest yield strength at low temperatures < 500°C. However, alloy TTZ2M exhibited higher yield strength than BL-Mo, which is more pronounced at temperatures > 500°C. The lower hardness of 53T1 and 63T1 led to lower yield strength than TTZ2M. All the alloys, except for Z2N13, showed yield strength greater than T91, which compromised their total elongations as shown in Figure 11b. The "instability" of Z1N33A with abnormally low yield strength and total elongation at room temperature was attributed to the inhomogeneous distribution of a large amount of coarse Zr-rich Laves phase.

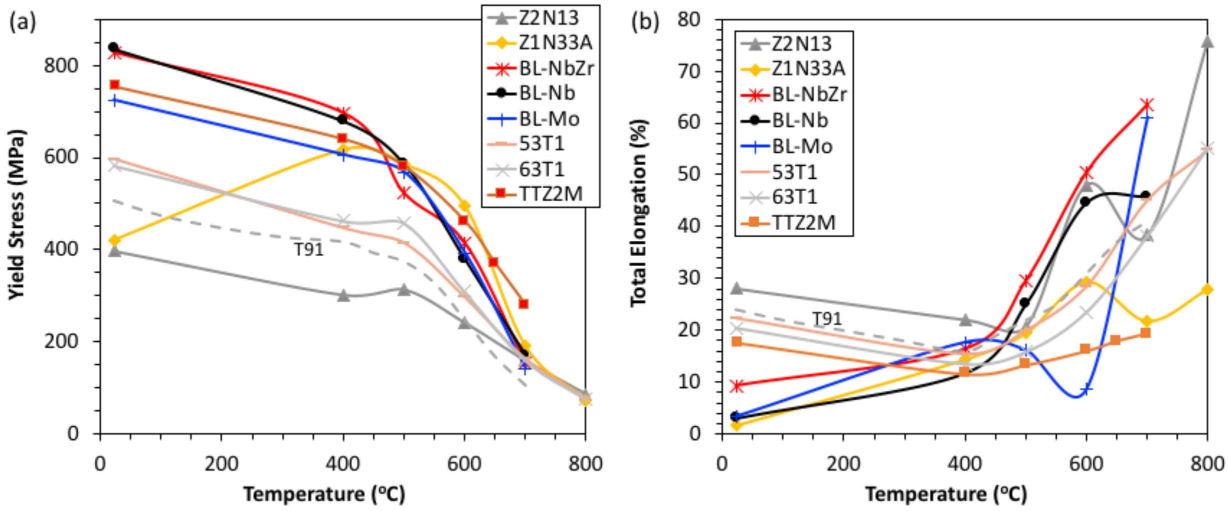

Figure 11. Temperature-dependent (a) yield strength and (b) total elongation of ferritic alloys Z2N13, Z1N33A, BL-NbZr, BL-Nb, BL-Mo and ferritic-martensitic steels 53T1, 63T1, and TTZ2M, compared with T91.

Quick screening of the creep resistant of the alloys was conducted at 650°C and 120 MPa. Alloy Z2N13 was not screened because of its lowest hardness and yield strength. Figure 12 indicates the longest creep life of BL-Nb and TTZ2M for ferritic and ferritic-martensitic alloys, respectively, which are significantly longer than the creep life of T91. Alloy BL-Mo showed the shortest creep life, which was attributable to its largest grain size without enough coarse precipitates, e.g., Fe_2(W,Mo) Laves phase, to pin the boundaries although it has a high density of fine and ultrafine precipitates of B2-NiAl. In contrast to the generally high shear modulus (~135–221 GPa) of the other types of precipitates such as Fe_2W Laves, $Cr_{23}C_6$, TiC, and TaC in the ferritic and ferritic-martensitic alloy, the low shear modulus of B2-NiAl at ~70 GPa has a low strengthening effect and would not effectively prevent the migration of grain boundaries. The small amount of Zr alloying in BL-NbZr led to some coarse Zr-containing Laves phase in an irregular shape, resulting in a premature failure with a short creep life, which is also evidenced by the abnormally reduced yield strength of BL-NbZr at 500°C in Figure 11a. Similarly, alloy Z1N33A with a noticeably higher content of Zr slightly enhanced the creep resistance compared to BL-NbZr but has more pronounced premature failure due to the inhomogeneous distribution of Fe_2Zr-type precipitates. Although 53T1 and 63T1 had slightly greater yield strength than T91 at 650°C, their creep lives at 650°C were slightly shorter than T91, which suggests the thermal instability of the two alloys.

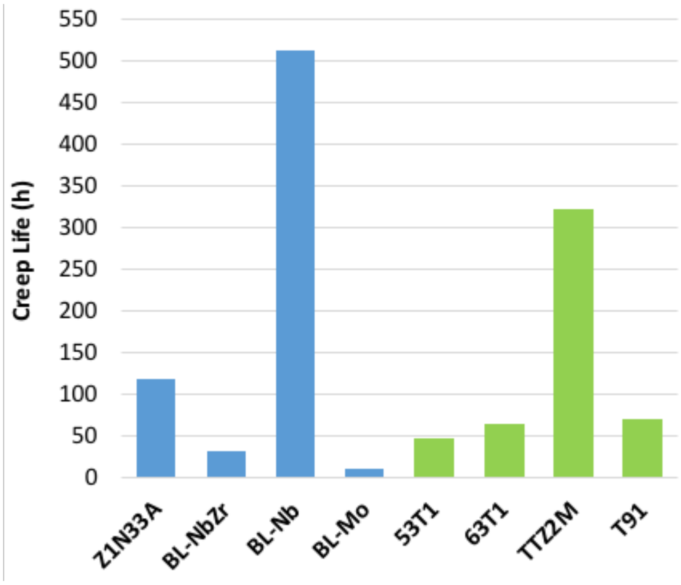

Figure 12. Creep life of ferritic alloys Z1N33A, BL-NbZr, BL-Nb, BL-Mo and ferritic-martensitic steels 53T1, 63T1, and TTZ2M tested at 650°C and 120 MPa.

Self-ion (Fe^{2+}) irradiation was conducted on the samples of the designed alloys using rastering beam at 350 and 475°C for up to 220 dpa. Nanoindentation was measured at different depth on the irradiated and unirradiated surfaces of the samples. Radiation hardening was evaluated at 1 μm indentation depth because of the maximum irradiation-influenced depth of ~1.6 μm according to the Stopping and Range of Ions in Matter (SRIM) simulations. Figure 13 indicates the ~20–25% radiation hardening for alloys Z2N13 and Z1N33A irradiated at 350°C. TTZ2M had a similar radiation hardening level but with a noticeably smaller standard deviation for the 350°C irradiation. The 53T1 and 63T1 showed distinct radiation hardening levels, i.e., ~9% vs ~49%, respectively, for the 350°C irradiation, although they had mostly identical mechanical properties as presented in Figure 10–12. The 475°C irradiation revealed minimal radiation hardening in TTZ2M with a minimal standard deviation. The ferritic alloys showed slightly greater radiation hardening with Z1N33A having the greatest radiation hardening to ~9.5%.

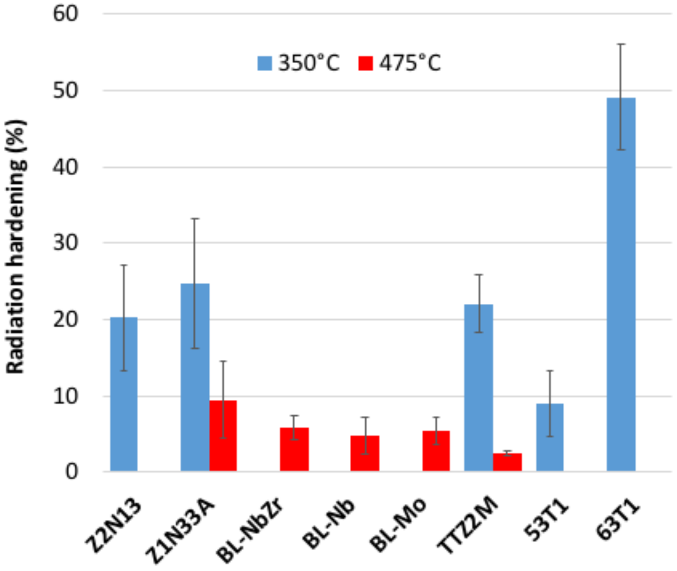

Figure 13. Radiation hardening measured by nanoindentation at a depth of 1 µm for ferritic alloys Z2N13, Z1N33A, BL-NbZr, BL-Nb, BL-Mo and ferritic-martensitic steels 53T1, 63T1, and TTZ2M irradiated with Fe2+ up to 220 dpa at 350 and 475°C.

3.4 DOWN-SELECTED ALLOYS

Based on the mechanical properties and radiation hardening screening of the designed alloys as presented in the previous section, one ferritic alloy (BL-Nb) and one ferritic-martensitic steel (TTZ2M) were down-selected. The poor performance of 53T1 and 63T1 compared with TTZ2M was attributable to the alloy compositions, which were analyzed to be significantly deviated from the designed concentrations for Ti and C. Referring to the TTZ2M, two scale-up heats of ferritic-martensitic steels, named as FTN1 (or NA) and FTT1 (or TA), were procured with a weight of ~60 lbs. per heat in contrast to the ~1 lb. of a laboratory heat, which were fabricated using an industrial vacuum induction melting facility. The nominal compositions in weight percentage (wt.%) of the down-selected steels and scale-up heats, together with a reference steel T91, are listed in Table 3.

Table 3. Down-selected steels and reference steel.

Alloy ID	Nominal composition (with Fe balance)	Fabrication	Alloy type
BL-Nb	12Cr-3W-3Ni-3Al-1Nb	Small laboratory heat by arc-melting/casting	Ferritic
TTZ2M	8.6Cr-1.4W-0.1V-0.1Ti-0.05Nb-0.1C		Ferritic-martensitic
FTN1 (NA)	8.6Cr-1.4W-0.1V-0.1Ti-0.05Nb-0.1C	Large industrial heat by vacuum induction melting	
FTT1 (TA)	8.6Cr-1.4W-0.1V-0.1Ti-0.05Ta-0.1C		
T91 *	8.4Cr-0.9Mo-0.2V-0.1Nb-0.1CN	Commercial heat	

* Used as a reference during the ion irradiation experimental study. Literature data of T91 and Grade 91 are used as references for mechanical tests.

Alloys FTN1 (NA) and FTT1 (TA) have phase constitutions similar to TTZ2M as shown in Figure 9a. Guided by the thermodynamic calculations, alloys FTN1 (NA) and FTT1 (TA) were hot-forged to 0.75”-thick plates at 1100°C, followed by normalization at 1170°C for 20 minutes and tempering at 750°C for 1 h with air cooling.

4. MECHANICAL PROPERTIES OF DOWN-SELECTED ALLOYS

4.1 TENSILE PROPERTIES

Figure 14 plots the temperature-dependent yield strength, tensile strength, uniform elongation, and total elongation of the four alloys. Literature data of T91 are included as a reference [9]. The four alloys, BL-Nb, TTZ2M, FTT1, and FTN1, generally exhibited greater strength with somewhat compromised total elongation compared with T91. The ferritic steel BL-Nb showed slightly higher strengths with lower total elongations than the ferritic-martensitic steels TTZ2M, FTT1, and FTN1 at temperatures below 500°C, above which the relationship became opposite. The abnormal change in the strength of FTN1 and in the uniform elongation of BL-Nb at 400 and 500°C may suggest the presence of inhomogeneous microstructures in the two alloys. The heat-treated version FTT1-T and FTN1-T exhibited nearly identical strengths lower than their standard version with comparable elongations higher than their standard version.

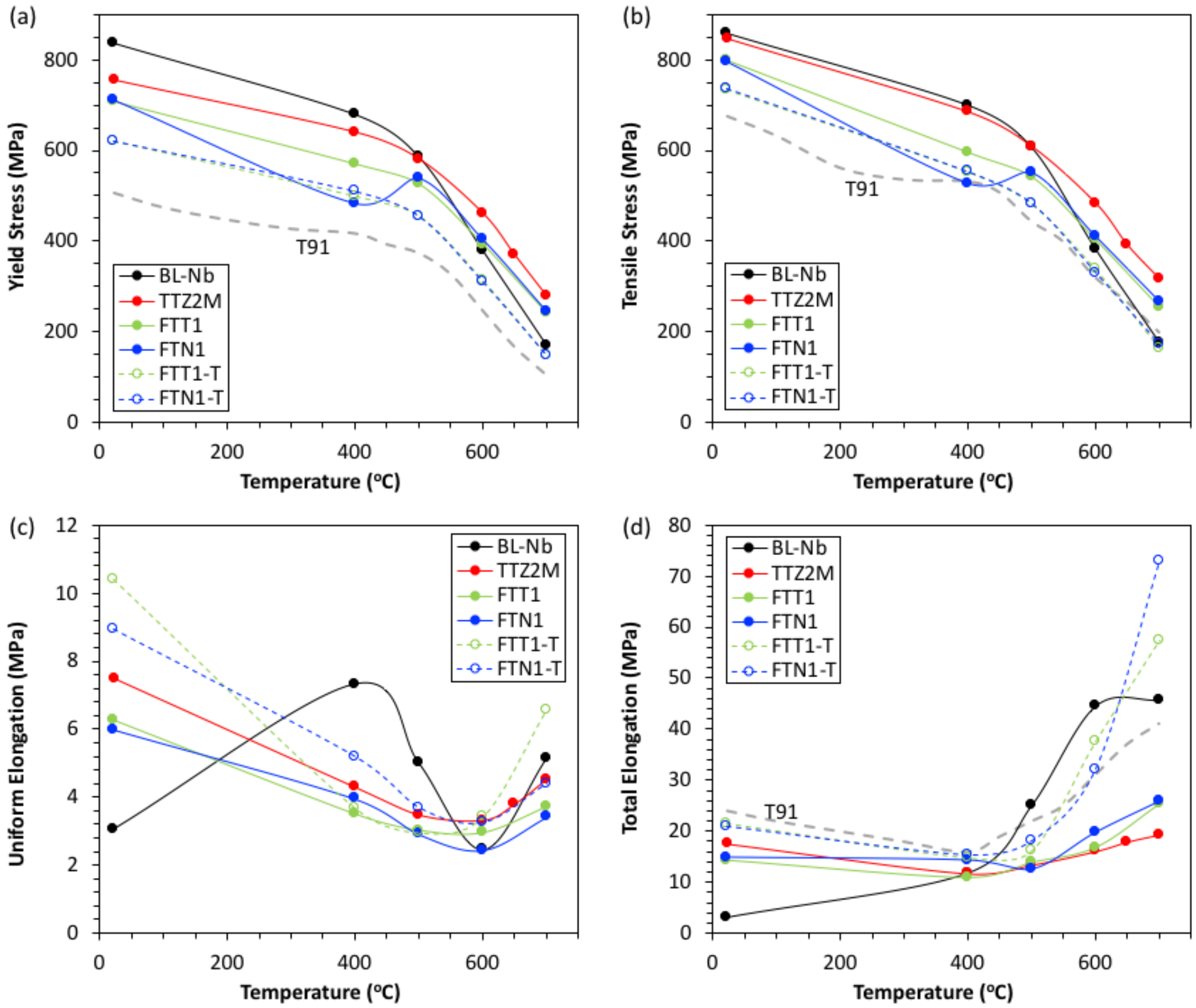

Figure 14. Temperature-dependent (a) yield strength, (b) tensile strength, (c) uniform elongation, and (d) total elongation of the ferritic (BL-Nb) and ferritic-martensitic (TTZ2M, FTN1, and FTT1) steels, compared to literature data of T91. FTN1-T and FTT1-T are a heat-treated version of FTN1 and FTT1, respectively.

4.2 CHARPY IMPACT TOUGHNESS

Figure 15 plots the temperature-dependent absorbed energy for the interested steels, with Grade 91 heat 30176 as a reference [10]. To obtain the ductile-brittle transition temperature (DBTT) and upper-shelf energy (USE), the data were fitted by the general hyperbolic tangent function $E = a + b \tanh [(T - T_0)/c]$, where T is test temperature and a, b, c, and T_0 are regression coefficients. T_0 gives the mathematical DBTT, corresponding to the mean value of USE and the lower-shelf energy (LSE), i.e., USE/2 assuming LSE = 0 in Figure 15. Comparison of the materials with the same sample size and orientation indicates the comparable Charpy impact toughness of FTT1 and FTN1, which is superior to TTZ2M and significantly greater than Grade 91. The forging process applied to the large-scale heats FTT1 and FTN1 might have benefited their superior Charpy impact toughness compared with the lab-scale TTZ2M without forging. The heat-treated version FTT1-T and FTN1-T showed gradual decrease of absorbed energy with decreasing temperature, which is in contrast to the sharp decrease of the standard version but similar to the behavior of austenitic steels. Following the NRC regulatory guide of 68-J of full-size Charpy specimens for pressure vessels, the corresponding threshold energy would be 8.5-J for the half-size Charpy specimens assuming linear relationship between the energy and the nominal fracture volume of $(Wb)^{3/2}$, where W is the specimen width and b is the ligament depth beneath the V-notch. Consequently, the DBTT of TTZ2M, FTT1, and FTN1 are 20 to 60°C lower than that of Grade 91 of –47°C. While the DBTT of FTT1-T and FTN1-T are well below –150°C. Ferritic steel BL-Nb exhibited the lowest impact toughness with USE comparable to general oxide-dispersion-strengthened ferritic alloys.

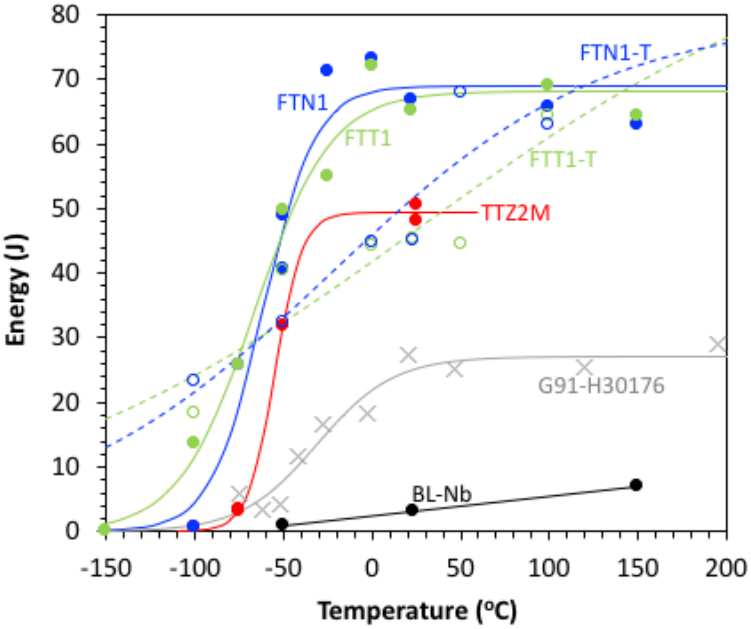

Figure 15. Temperature-dependent Charpy absorbed energy of the ferritic (BL-Nb) and ferritic-martensitic (TTZ2M, FTN1, FTT1, and the heat-treated version FTN1-T and FTT1-T) steels, compared to literature data of Grade 91 heat 30176.

4.3 CREEP RESISTANCE

Figure 16 plots the creep strain as a function of creep time for the down-selected steels BL-Nb, TTZ2M, FTN1, and FTT1 compared with a commercial heat of T91, which were tested using type SS-3 miniature specimens in air at 650°C and 100 and 120 MPa. Other conditions such as 110 MPa were also tested but are not reported here because only T91 and TTZ2M were tested. The test of FTN1 under 100 MPa at 650°C is still running during the preparation of this report. The creep curves indicate the superior creep resistance of the down-selected steels compared to reference steel T91.

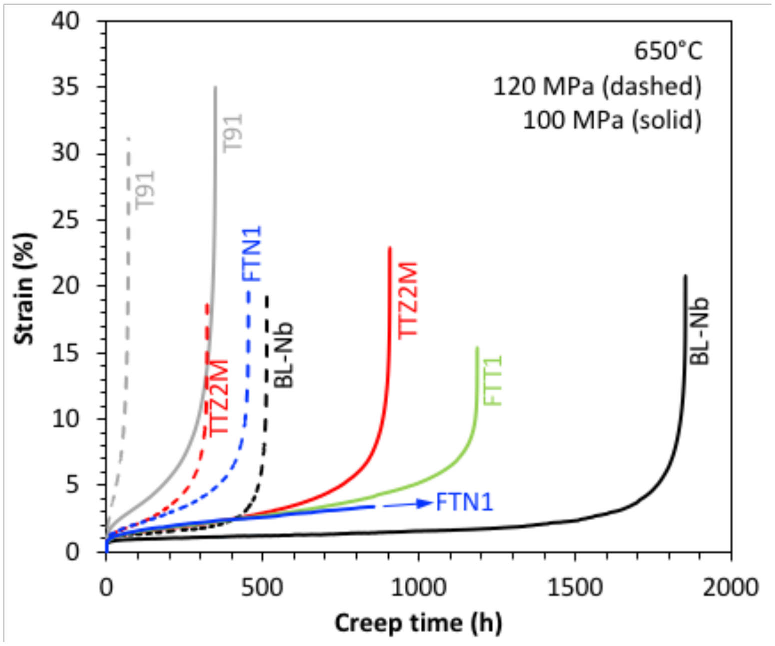

Figure 16. Creep strain-time curves for the down-selected alloys BL-Nb, TTZ2M, FTN1, and FTT1 compared with T91 tested at 650°C and 120 MPa (dashed) and 100 MPa (solid).

The creep curves were analyzed to deduce their minimum creep rates and the ratios of creep-rupture life of BL-Nb, TTZ2M, FTN1, and FTT1 over that of T91 at 650°C, which are summarized in Table 4. The minimum creep rate as a function of stress is plotted in Figure 17. The alloys showed similar slopes of the fitting lines for the alloys. Alloy BL-Nb had the lowest minimum creep rates compared to the highest minimum creep rates of T91. The ferritic-martensitic steels had comparable minimum creep rates. The creep-rupture lives of the down-selected steels were 2.60 to 7.29 times of that of T91. The ferritic steel BL-Nb exhibited the best creep resistance. The large-scale heats FTT1 and FTN1 showed slightly superior creep resistance than the small laboratory heat TTZ2M. Alloy FTN1 tends to be slightly superior to FTT1 and TTZ2M in terms of creep rupture life and minimum creep rate.

Table 4. Minimum creep rates (h^{-1}) of the designed alloys compared to T91 tested at 650°C.

Alloy	Minimum creep rate (h^{-1})		Creep-rupture life ratio over T91	
	120 MPa	100 MPa	120 MPa	100 MPa
BL-Nb	1.93×10^{-5}	5.68×10^{-6}	7.29	5.32
TTZ2M	8.72×10^{-5}	2.97×10^{-5}	4.57	2.60
FTN1	7.65×10^{-5}	2.16×10^{-5}	6.45	NA
FTT1	NA	2.87×10^{-5}	NA	3.41
T91	1.04×10^{-3}	1.72×10^{-4}	1	1

NA: not available during the preparation of the report.

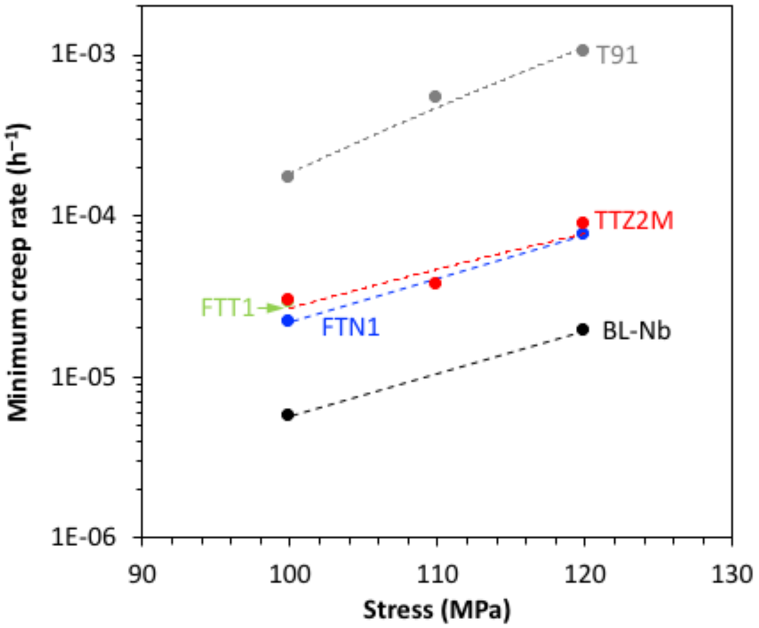

Figure 17. Stress-dependent minimum creep rates of alloys BL-Nb, TTZ2M, FTN1, and FTT1 compared with T91 tested at 650°C.

4.4 SUMMARY

The down-selected alloys BL-Nb, TTZ2M, FTN1, and FTT1 exhibited noticeable enhancements in strength, Charpy impact toughness, and creep resistance compared to T91, except for BL-Nb having significantly lower impact toughness than T91. The results of the basic mechanical tests are summarized below:

- The ferritic steel BL-Nb had the highest strength and creep resistance but the worst Charpy impact toughness.
- The ferritic-martensitic steels TTZ2M, FTN1, and FTT1 had noticeably enhanced strength, creep resistance, and Charpy impact toughness compared to reference steel T91.
- The heat-treated condition FTN1-T and FTT1-T exhibited comparable tensile properties and Charpy impact toughness, which have lower strength but noticeably higher Charpy impact toughness than their standard condition.
- The large-scale industrial heats FTN1 and FTT1 had slightly inferior tensile properties but slightly superior creep resistance and Charpy impact toughness compared to the small laboratory heat TTZ2M, which suggest the property sustainability and scale-up fabrication feasibility of the developed ferritic-martensitic steels.

5. MICROSTRUCTURAL CHARACTERIZATION OF DOWN-SELECTED ALLOYS

5.1 REFERENCE ALLOY T91

Figure 18 shows the tab-section microstructures of T91 creep-tested at 650°C and 100 MPa in HAADF images and EDS maps, which indicate noticeable recovery of the pre-existing lath sub-structures, especially for the grains near sample surfaces (top of Figure 18a) in contrast to some of the grains in the substrate (Figure 18b). Primary two types of precipitates, likely to be $Cr_{23}C_6$ and (Nb,V)(C,N), were suggested by EDS mapping (Figure 18d-f) of Figure 18c, which have sizes of ~150 nm and ~20–100 nm and densities of $\sim 3\times10^{19}$ and $\sim 1\times10^{20}$ m^{-3}, respectively. The real densities of the precipitates in T91 are expected to be lower because Figure 18c was the only local area having such a high density of precipitates.

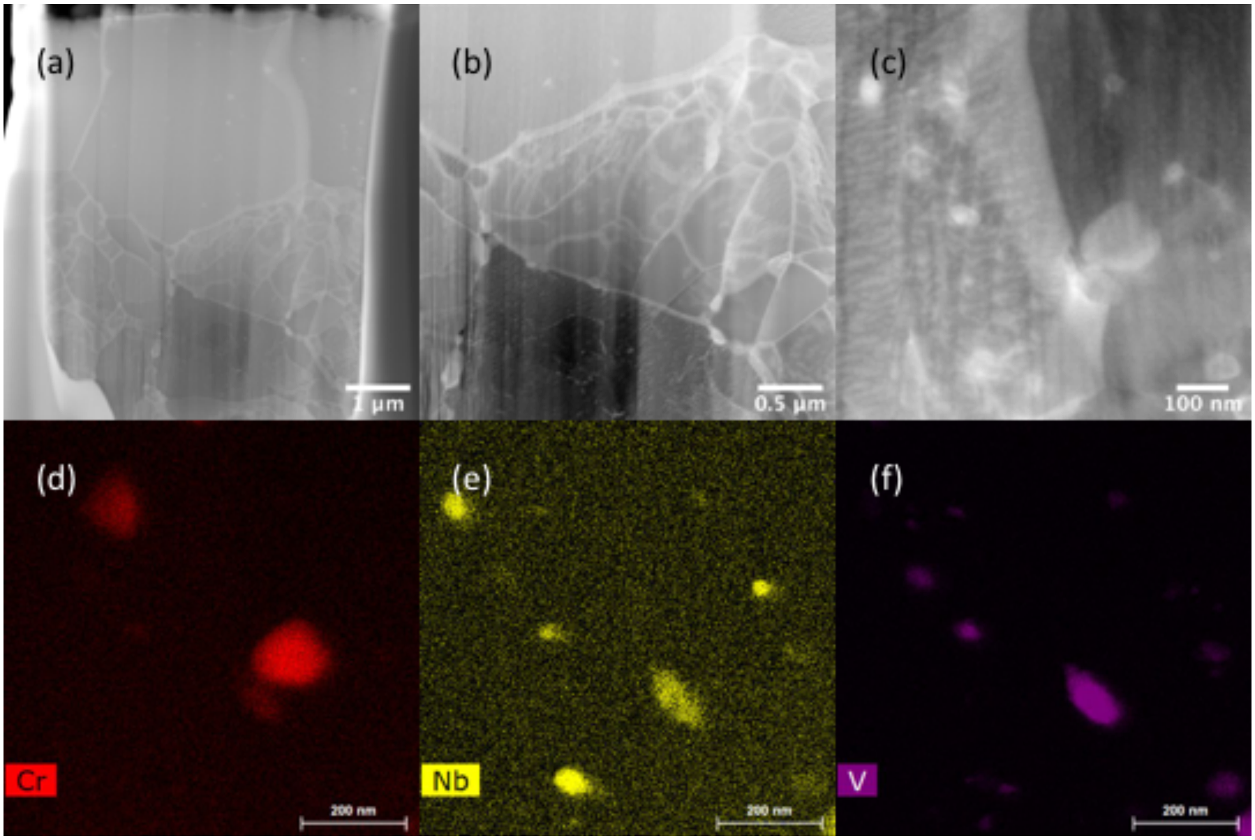

Figure 18. (a-c) HAADF images of the tab-section T91 creep-tested at 650°C and 100 MPa and (d-f) EDS maps of (c).

Figure 19 shows the dislocation structures in the STEM BF images obtained at the [001] zone of the grains from the gauge section of T91 creep-tested at 120 and 100 MPa. In general, the dislocation densities are very low, with 7.5×10^{13} and 2.9×10^{13} m^{-2} for the 120 and 100 MPa conditions, respectively, which are nearly one order of magnitude lower than the free dislocation density in the as-received condition. The low dislocation density might be attributable to the limited precipitates that could not retain the dislocations at 650°C. The lower stress and longer exposure time resulted in less and shorter dislocation sections.

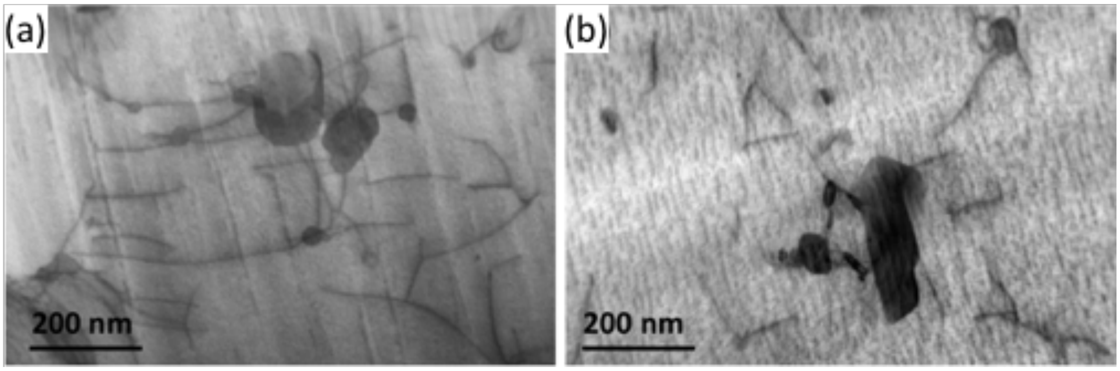

Figure 19. BF-STEM images with the [001] zone from the gauge section of T91 creep-tested at 650°C and (a) 120 and (b) 100 MPa.

5.2 ALLOY BL-Nb

Figure 20 shows the microstructures of BL-Nb, indicating the coarsened grains near the surfaces beneath the FIB-deposited Pt-layer and the retained sub-micrometer grains in the substrate in Figure 20a. EDS mapping of Figure 20b revealed two types of precipitates as NiAl and Fe$_2$(W,Nb) with comparable densities of $\sim 6\times10^{19}$ and $\sim 7\times10^{19}$ m^{-3}, respectively. The Ni-map was coincident with the Al-map in Figure 20c and the Nb-map was coincident with the W-map in Figure 20d. Unlike NiAl primarily in a spherical shape (~40–180 nm) dispersed in matrix, Fe$_2$(W,Nb) is in an irregular shape (~45–230 nm in length) primarily pinning the fine grain boundaries as shown in Figure 20e. The white Fe$_2$(W,Nb) particles are diminished in the near surface grains, which might have facilitated the coarsening of the near surface grains. However, the fate of the Fe$_2$(W,Nb) in the near surface grains is not clear yet.

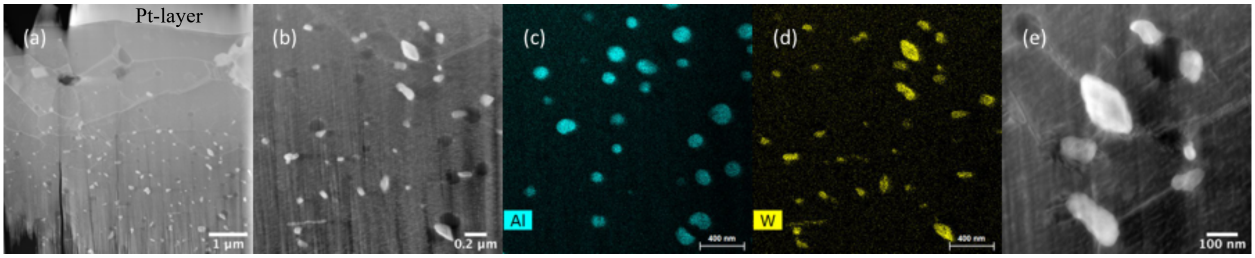

Figure 20. (a) BF-STEM and (b) HAADF images near the [001] zone of the bcc matrix in the gauge section of the BL-Nb sample creep-tested at 650°C and 100 MPa.

Figure 21 shows the bright-field (BF) STEM and high-angle annular dark field (HAADF) images taken near the [001] zone of the matrix in the gauge section of the BL-Nb sample creep-tested at 650°C and 100 MPa. The line features are dislocations and the particles are of the Laves phase. Having a mean Z number close to that of the matrix, the B2-NiAl particles are not obvious in the BF-STEM and HAADF images. Dislocations are not uniformly distributed. The subgrain at the bottom left corner contains a higher density of dislocations. Straight dislocation segments were observed, with some of them being marked by white triangles. Referring to the inserted diffraction pattern, the marked dislocation segments are on the <110> planes. It is also frequently observed that one end of the dislocation is tied to the particles, suggesting that some dislocations were generated at the particle-matrix interfaces.

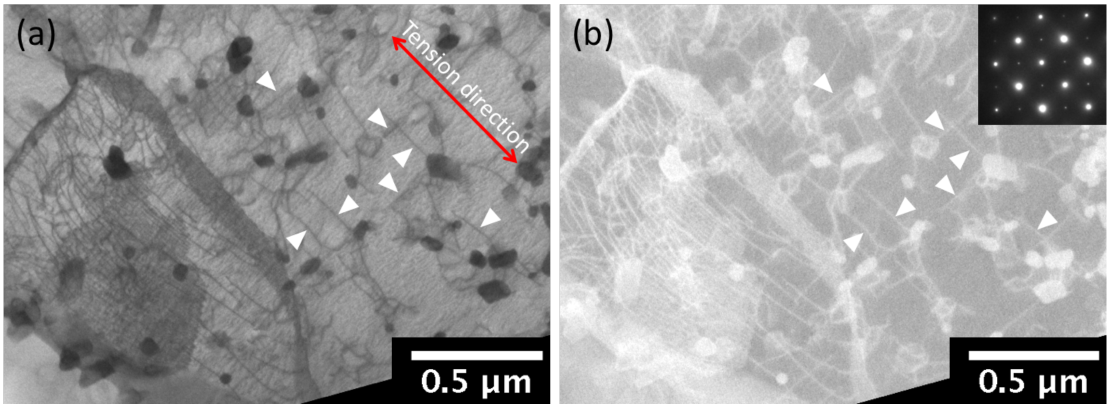

Figure 21. (a) BF-STEM and (b) HAADF images near the [001] zone of the bcc matrix in the gauge section of the BL-Nb sample creep-tested at 650°C and 100 MPa.

Dislocation-particle interactions were observed in the samples. The dislocation line marked by a white arrow in Figure 22a appears to be interacting with a B2-NiAl particle. The DF-TEM image of Figure 22b from the same region of Figure 22a highlights the B2-NiAl particles. The B2-NiAl precipitate marked by a white arrow in Figure 22b is located at the cusp of the dislocation shown in Figure 22a. Due to the obstacle effect of the B2-NiAl particle, the dislocation line bends over the B2-NiAl particle, as shown in the DF-TEM image of Figure 22c obtained at the (200) beam condition. Figure 22d is obtained at the (110) beam condition showing that some segments of the dislocation line is not on contrast. This indicates that the Burgers vector of the dislocation changed due to its interaction with the B2 precipitate. As a result of the interactions, defects were developed in the B2-NiAl precipitates, as shown by the dark stripes inside of the B2-NiAl particles in Figure 22b.

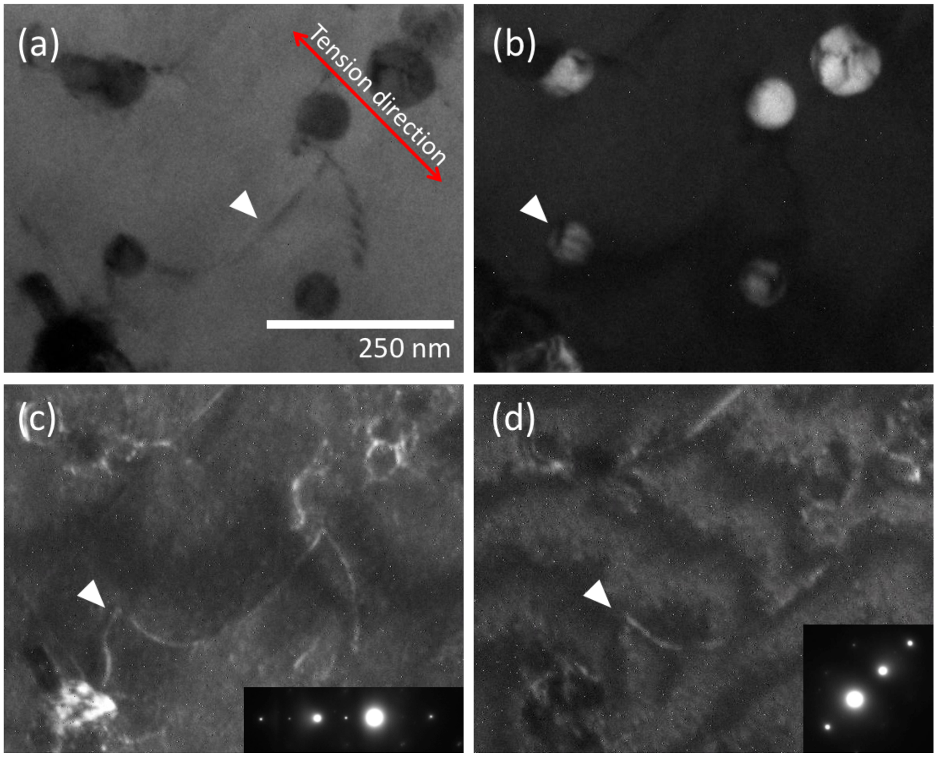

Figure 22. (a) BF and (b-d) DF TEM images in the gauge section of the BL-Nb sample creep-tested at 650°C and 100 MPa.

Figure 23 shows the evolution of B2 precipitates induced by thermal aging (end section of the creep sample without stress) and creep stresses (gauge section of the creep sample). Figure 23a presents the electron diffraction pattern obtained from the matrix of the as-received sample. The dashed rectangle marks the diffraction pattern of the bcc structured matrix on its [011] zone. The super lattice spots of the bcc pattern are visible, attributed to the presence of the coherent B2 precipitates. The (±100) spots of the B2 precipitates in Figure 23a are marked by the solid circles. Figure 23b is a dark-field (DF) micrograph imaged using the (100) spot of the B2 phase. The bright spherical features are the B2 precipitates uniformly distributed in the bcc matrix. The chemical composition of the precipitates was investigated using EDS technique. The EDS maps of Ni and Al in the as-received sample are presented in Figure 23c and d, respectively. The crystal structure identification and the chemical composition investigation of the precipitates indicate that the precipitates are NiAl phase having a B2 structure. The diameter of the precipitates is measured to be 16 ± 3 nm. Figure 23e-h present the Ni map to show the distribution of B2 precipitates in the creep-ruptured samples of 120 MPa in (e-f) and 100 MPa in (g-h). Figure 23e-g were captured from the thermal-aged region and Figure 23f-h from the deformed (gauge) region. After the thermal aging for 512 and 1852 hours, the diameters of the B2 precipitates increased to 77 ± 25 and 122 ± 41 nm, as shown in Figure 23e and g, respectively. The mean diameter of the precipitates measured from the deformed region is slightly larger than that from the thermal-aged region, i.e., 81 ± 23 and 127 ± 37 nm for the 100 and 120 MPa samples, respectively.

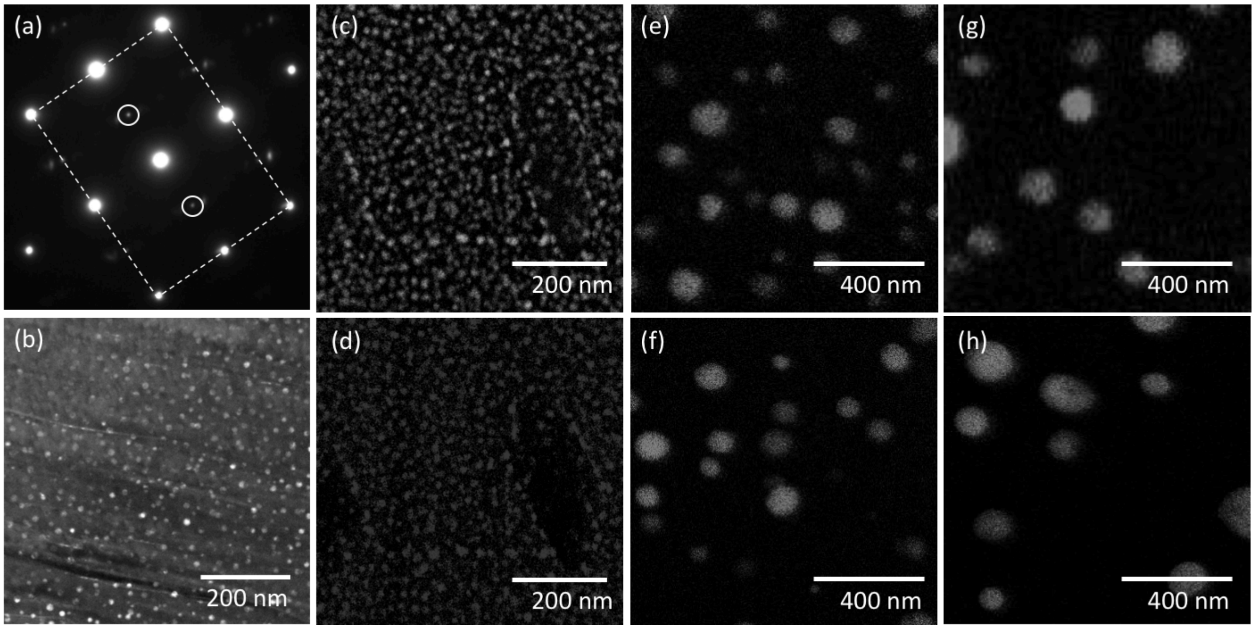

Figure 23. (a) A SAED pattern obtained from the matrix of the as-received sample. (b) A DF-TEM image of the coherent precipitates. The EDS mappings of (c) Ni and (d) Al of the as-received sample, and the Ni mappings from the (e) thermal-aged and (f) deformed regions of the 120 MPa creep sample, and the (g) thermal-aged and (h) deformed regions of the 100 MPa creep sample.

Following the size analysis in Figure 23, Figure 24 plots B2-NiAl particle radius (R) in cubic power as a function of time (t), which shows that stress enhances the coarsening of B2-NiAl precipitates. The kinetic constants (k) of the thermal aged and stressed conditions are estimated to be 125 and 138 nm^3/h, respectively, according to $k=(R^3-R_0^3)/t$.

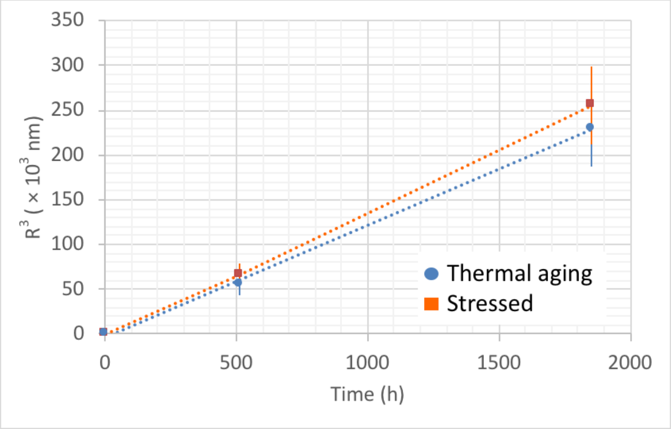

Figure 24. Time-dependent radius (R) in cubic power of B2-NiAl particles under the thermal aging and stressed conditions at 650°C.

Other than coarsening kinetics, the chemistry evolution of B2-NiAl particles were also investigated using EDS mapping under the STEM mode. The EDS-mapped B2-NiAl particles that are standalone without overlapping with other particles were analyzed by excluding the interference from matrix chemistry. Figure 25 shows the relative Ni-Al ratios of B2-NiAl particles in thermal aged and stressed conditions, normalized to the ratio of the as-received condition, of the 1852 h creep-ruptured sample. The compositional change in B2-NiAl precipitates induced by thermal aging and stress is not significant.

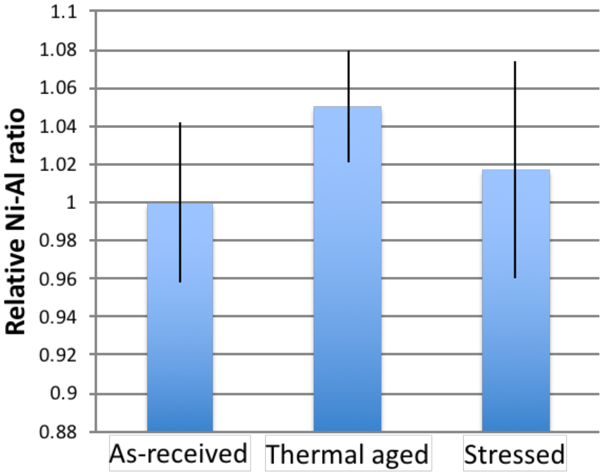

Figure 25. EDS analyzed relative Ni-Al ratio of B2-NiAl particles at the as-received condition and the 650°C aged and stressed conditions.

Figure 26a shows the precipitates of the Laves phase in the as-received condition. The precipitates have facet interface {110} planes of the bcc matrix and irregular morphology. The electron diffraction pattern of the area containing precipitates of the Laves phase is shown in Figure 26b, where the stronger and weaker spots are attributed to the electron diffraction of the matrix and the Laves precipitates, respectively. The alignment between the diffraction patterns of the precipitates and the matrix indicates a planar coherency relationship between the lattice planes of the precipitates and the {110} planes of the bcc. When imaged using different diffraction spots of the precipitates, for instance, the spots marked by the circle and the square in Figure 26b, different precipitates are highlighted in the corresponding DF images in Figure 26c and d, respectively. This indicate that different precipitates are coherent to different lattice planes of the bcc matrix.

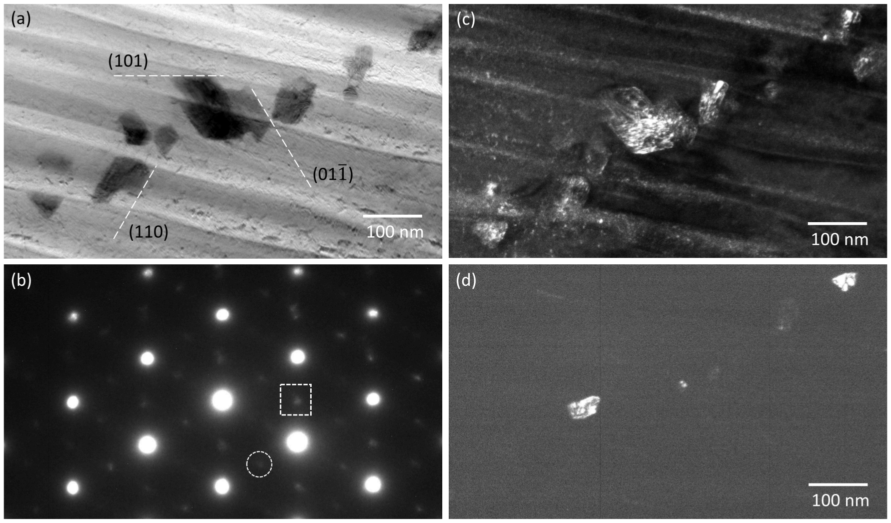

Figure 26. Laves phase precipitates in the bcc matrix presented in (a) BF-TEM image, (b) SAED pattern of the [$\bar{1}$11] zone of the matrix, (c-d) DF-TEM images using the spots marked by the circle and square in (b), respectively.

As shown in Figure 27, the chemical composition of the Laves precipitates was determined to be $Fe_2(Nb,W)$. EDS quantification shows a W-Nb atomic ratio of 0.87 : 1. The EDS maps in Figure 27b-c show that Nb and W are not uniformly distributed in the precipitates. W is slightly enriched in the shell of the precipitates, particularly at some portion of the precipitate-matrix interface. The slight segregation of Nb and W still presents in the creep-tested samples, as shown in Figure 27d-f. The mean sizes of the Laves precipitates in different samples are summarized in Table 5. The differences in the precipitate sizes are within the experimental error.

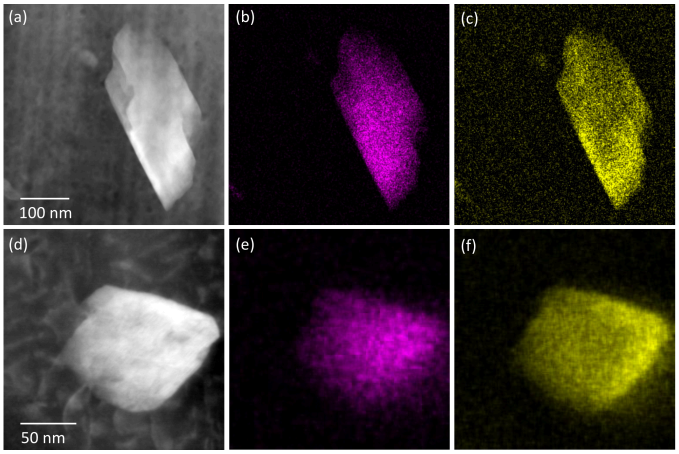

Figure 27. Laves phase precipitates presented in: (a) and (d) HAADF images, (b) and (e) EDS mapping of Nb, and (c) and (f) EDS mapping of W, for (a-c) the as-received condition and (d-f) the 1852-hour thermal-aged and stressed condition.

Table 5. Mean size of Laves phase under different conditions at 650°C.

Condition	As-received	512-h thermal aged	512-h 120 MPa	1852-h thermal aged	1852-h 100 MPa
Mean size (nm)*	70 ± 30	80 ± 30	70 ± 40	70 ± 30	80 ± 30

* Geometric mean value of a long and short axes of the precipitates. The uncertainty is the standard deviation.

As shown in Figure 28, the W-Nb atomic ratios in the Laves phase are higher in the thermal-aged samples than the as-received sample. This implies that precipitation of Fe_2W on the existing $Fe_2(Nb,W)$ precipitates took place during the thermal annealing. Figure 28 also shows that the most significant change in the W-Nb atomic ratio occurred within the shorter time 512 hours of thermal aging, suggesting that the driving force for continuous precipitation of the Laves phase was the supersaturation of tungsten, which was decreased with time.

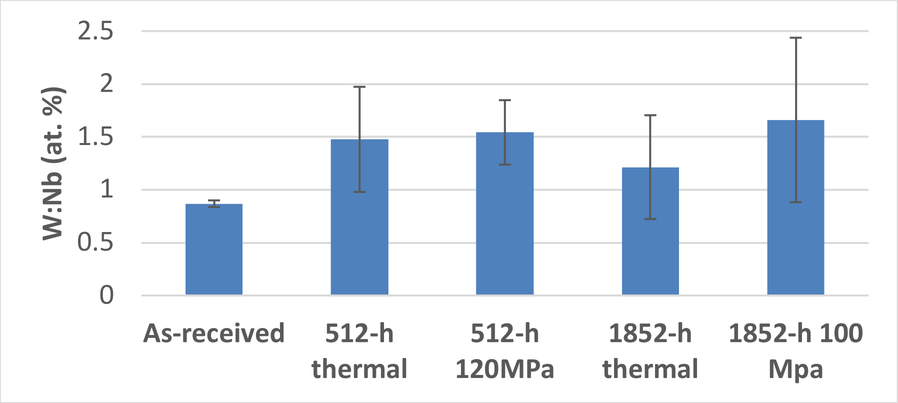

Figure 28. The evolution of W-Nb atomic ratio in the Laves precipitates.

5.3 ALLOY TTZ2M

Figure 29 shows TEM images of the microstructure of the as-received TTZ2M alloy. The insert in Figure 29a shows the electron diffraction pattern of the beam condition that yielded the micrograph. Two sets of secondary reflections are identified and labeled for $M_{23}C_6$ and MX in addition to the primary reflections of $\{200\}_{bcc}$ matrix. The distance relationships of the secondary reflections were found to be in agreement with $M_{23}C_6$ and MX with lattice parameters of 1.089 and 0.414 nm, respectively, assuming the lattice parameter of matrix (bcc) as 0.287 nm. The DF image in Figure 29b was imaged using the $M_{23}C_6$ $(33\bar{1})$ diffraction spot, yielding the bright features in Figure 29b showing the distribution of the coherent precipitates with a size of 5-10 nm.

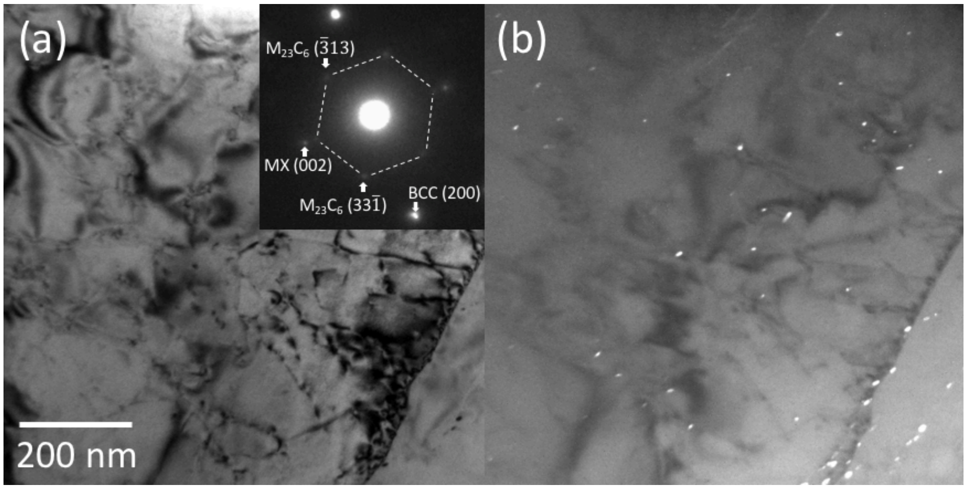

Figure 29. (a) BF- and (b) DF-TEM images showing the microstructure and precipitate distributions in the as-received TTZ2M alloy.

The microstructures of TTZ2M after the creep test at 100 MPa are shown in Figure 30, which indicate that the lath and dislocation sub-structures were mostly retained after the creep test. A high density (~4×10^{21} m^{-3}) of Ti-rich nanoprecipitates (likely to be TiC) with sizes < ~20 nm exists in the sample, most of which are pinning dislocations. Other than the dominant Ti-rich nanoprecipitates, Cr-rich (likely $Cr_{23}C_6$) and Ti-rich (likely TiN) coarse precipitates were occasionally observed.

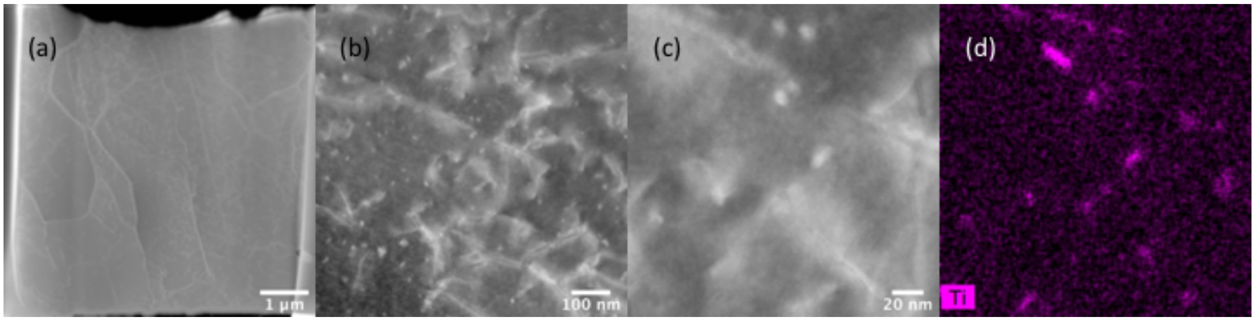

Figure 30. (a-c) HAADF images of TTZ2M creep-tested at 650°C and 100 MPa and (d) EDS map of (c).

Figure 31a-b show the STEM BF images from the gauge section of the samples after creep tests under the stresses of 120 and 100 MPa, respectively. Dislocation features developed in both samples with a density of 2.1×10^{14} and 1.3×10^{14} m^{-2} for the 120 and 100 MPa conditions, respectively. In addition, the black dot features dispersed in the matrix are believed to be the carbide precipitates, which seem to interact with the dislocations and possibly impeded their motion. The dislocation structures appear to be more tangled for the 100 MPa stressed sample than the 120 MPa stressed sample.

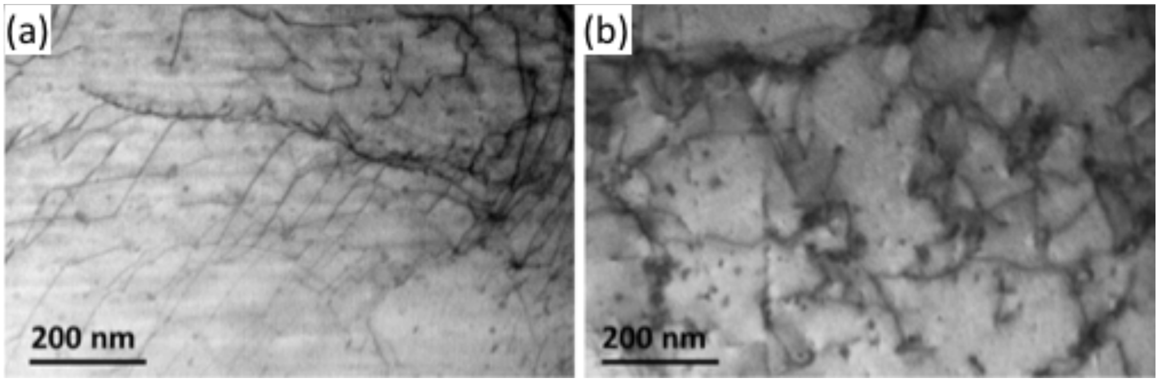

Figure 31. BF-STEM images imaged with the [001] zone from the gauge section of TTZ2M creep-tested at 650°C and (a) 120 and (b) 100 MPa.

5.4 ALLOYS FTT1 and FTN1

Figure 32 shows the optical micrographs of the standard normalized and tempered condition of FTT1 and FTN1, as well as the heat-treated condition FTT1-T and FTN1-T. Conventional tempered martensite structures developed in the standard condition with grain size on the order of 50 µm or larger. In contrast, the heat-treated condition shows noticeably refined grains with sizes on the order of 10 µm. The refined grains are attributed to the noticeably enhanced Charpy impact toughness with DBTT way below –150°C and USE above 76 J compared to the standard condition with DBTT of –90°C and –107°C and USE of ~69 J.

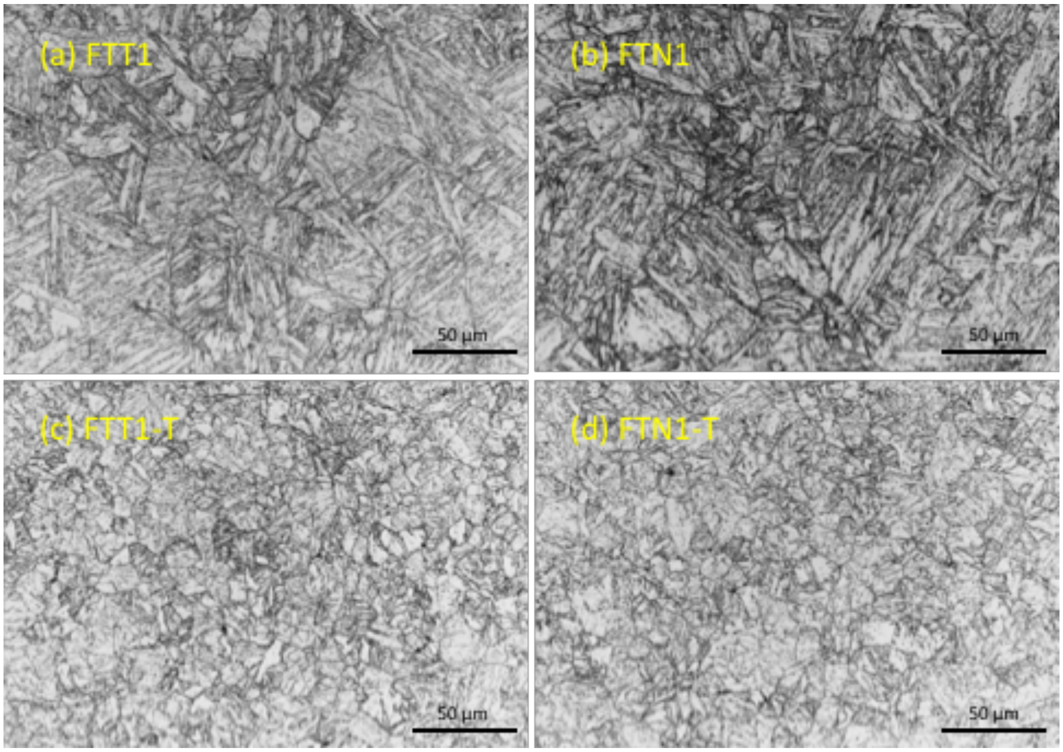

Figure 32. Optical micrographs of (a) FTT1 and (b) FTN1 and their heat-treated version (c) FTT1-T and (d) FTN1-T.

The overall grain structure of FTN1-T at a lower magnification is shown in Figure 33, which indicates few large grains close to the top-left corner. The presence of some large grains would explain the Charpy impact curve of FTN1-T in Figure 15, tending to have a ductile-brittle transition unlike FTT1-T having a nearly linear fitting curve.

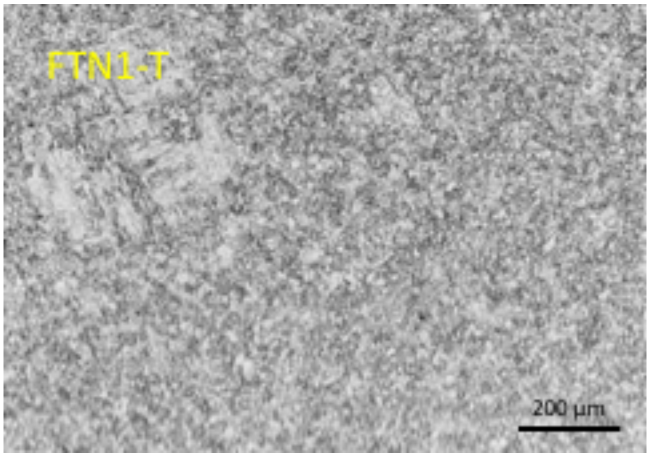

Figure 33. Optical micrograph of FTN1-T showing overall grain structure.

The FTT1 sample, creep-tested at 650°C and 100 MPa, was characterized. Figure 34 shows the BF and DF TEM and STEM images taken from the [001] zone axis, expect for the DF-TEM image in Figure 34c taken from the (020) two-beam condition near [001] zone axis. The dark region in Figure 34a-b are the [001] on-zone region, with the grey region deviated from the on-zone condition. Martensitic lath structure, with a lath width < 200 nm, retained in the tab section (Figure 34a) after nearly 1200 h exposure at 650°C. In contrast, the stress in the gauge section (Figure 34b) impaired the lath structure and initiated the formation of polygonal ferrite grains, with the lower-left grain in a size of ~1.1 µm in Figure 34b as an example. The ferrite grains are noticeably smaller than that (~3 µm) at the tab-section of T91 creep-tested at the same condition as shown in Figure 18a, suggesting superior heat resistance of FTT1 compared to T91. The DF-TEM image from the gauge section in Figure 34c shows nanoprecipitates in a pair of parallel white streaks, which is somewhat resemble butterflies or coffee beans, suggesting coherent relationship with the matrix, i.e., aligned with g_{020} of bcc. The white streaks have length in the range of ~3–12 nm. Similar to the rel-rod method determining radiation-induced Frank-loops in austenitic stainless steels, a factor of four was applied to the characterized density in the one of the four {200} two-beam conditions near the [001] zone axis, leading to the precipitate density of $(2.8 \pm 0.5) \times 10^{21}$ m^{-3}. BF-STEM image from the gauge section in Figure 34d reveals a high-density of dislocation, suggesting the intensive role of dislocations in the ferritic-martensitic steel under the creep test at 650°C.

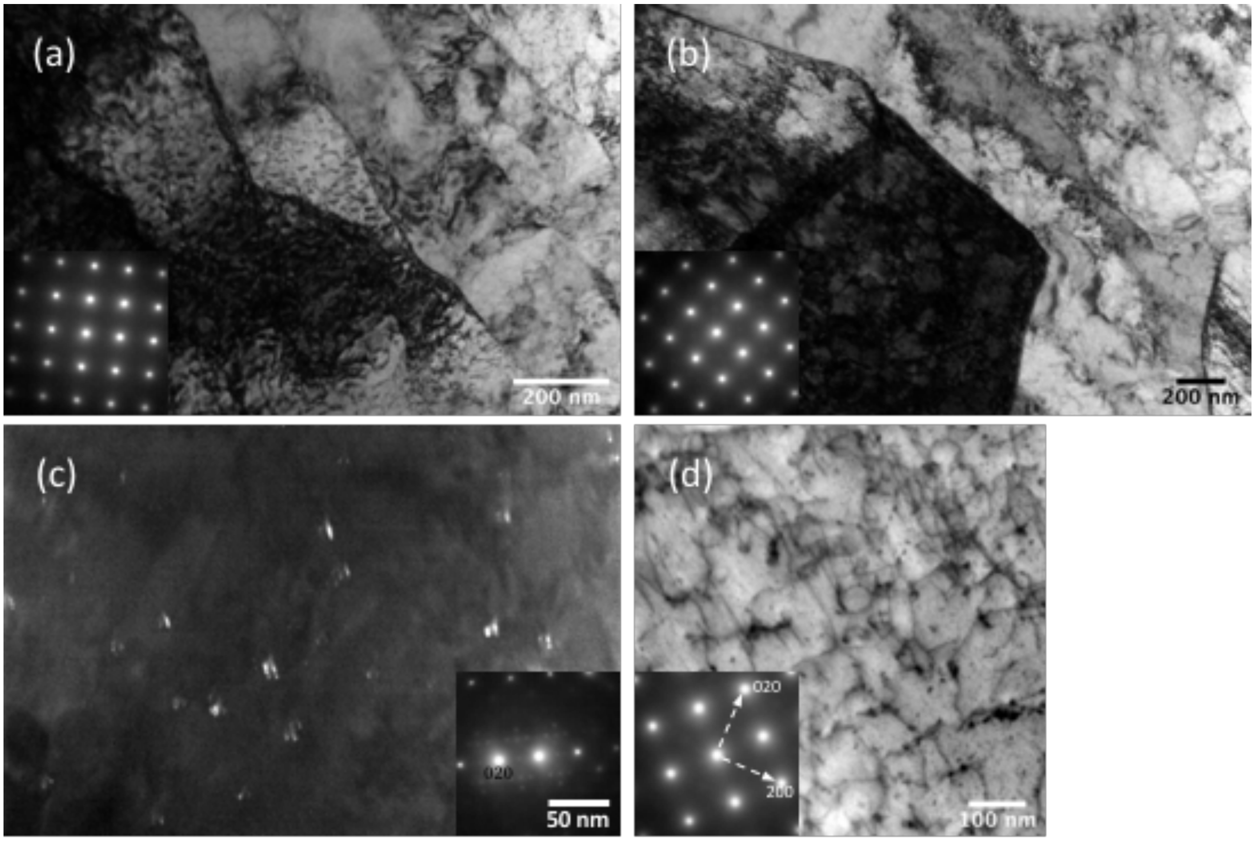

Figure 34. Creep-tested FTT1 at 650°C and 100 MPa: (a) BF-TEM image at the tab section, (b) BF-TEM image at the gauge section, (c) DF-TEM image at the gauge section, and (d) BF-STEM image at the gauge section.

The creep test of a FTN1 sample at 650°C and 100 MPa is running, and thus its microstructural characterization was not available during the preparation of this report, which will be completed for journal paper publication for comparing with the FTT1 sample. The heat-treated version FTN1-T and FTT1-T were not creep tested yet, but are expected to have creep resistance inferior to their standard counterpart FTN1 and FTT1 as suggested by their tensile properties in Figure 14.

5.5 SUMMARY

Microstructure characterizations of the creep-ruptured samples indicate noticeable recovery of T91 with diminished lath/block/packet sub-structures and reduced dislocations to the order of 10^{13} m^{-2}. The limited precipitates with a density on the order of 10^{19} m^{-3} would not effectively help retain the dislocations and the sub-structures at 650°C. In contrast, the large number of B2-NiAl and Laves $Fe_2(W,Nb)$ with about comparable sizes on the order of 100 nm and a combined density on the order of 10^{20} m^{-3} after the creep tests helped retain sub-grain structures of BL-Nb, although the size/density and the chemistry of the precipitates evolved during the creep tests. Similarly, the high-density (on the order of 10^{21} m^{-3}) of ultrafine (< ~20 nm) precipitates in TTZ2M and FTT1 helped retain the sub-structures and dislocations during the creep tests.

The microstructures of the untested condition indicated refined grains (~10 µm) for the heat-treated version FTN1-T and FTT1-T compared to the general ~50 µm or larger prior-austenite grains of the standard condition (FTN1 and FTT1) with tempered martensite structures. The refined grains would explain the enhanced Charpy impact toughness of the heat-treated version with compromised yield/tensile strength and creep resistance.

6. ION IRRADIATION OF DOWN-SELECTED ALLOYS

Rastering ion beam was used for the small laboratory heats, e.g., BL-Nb and TTZ2M, in previous irradiation experiments. However, defocused ion beam was employed for the large-scale industrial heats FTN1 and FTT1 in the latest irradiation experiments because literatures reported that rastering beam could suppress radiation-induced swelling. Samples of T91 were irradiated together with the other alloys during the rastering or defocused beam irradiation experiments.

6.1 DEFOCUSED BEAM

6.1.1 Fe^{2+} irradiation at 350°C

Two runs of 3.7 MeV Fe^{2+} irradiation for samples TA (FTT1) (run 1), NA (FTN1) and T91 (run 2) at 350°C to a peak damage of 250 dpa were performed with defocused and non-rastering ion beam, with irradiation parameters as:

- **Energy and Irradiating Ion Species:** defocused 3.7 MeV Fe^{2+} defocused beam. Aluminum implantation was found, as shown in Figure 38.
- **Damage Level**: peak damage 251 dpa in TA, NA, and T91 at ~1.0 μm depth, as shown in Figure 35.
- **Irradiation Temperature**: 351 ± 1°C for run 1 on TA, as shown in Figure 36a, and 351 ± 4°C for run 2 on NA and T91, as shown in Figure 36b.
- **Irradiation Flux**: $(7.5 \pm 0.6) \times 10^{12}$ ion/cm^2/s (run 1, Figure 36a) and $(8 \pm 3) \times 10^{12}$ ion/cm^2/s (run 2, Figure 36b). The large standard deviation of flux in run 2 came from the beam current spikes as shown in Figure 36b.
- **Vacuum/Base Pressure**: $(3.4 - 5.5) \times 10^{-7}$ Torr (base), $1.3 \times 10^{-6} - 4 \times 10^{-7}$ Torr (irradiation vacuum)

Figure 35 shows the damage depth profile of 3.7 MeV Fe^{2+} irradiation in the alloys. To achieve a peak damage of ~250 dpa, a fluence of 2.43×10^{17} Fe^{2+}/cm^2 was used. The peak damage took place at ~1.0 μm under surface. A sample of an austenitic alloy 2AT35 with a nominal composition of Fe-35Ni-3Al-2Ti was irradiated in the run-1 with the TA sample to study radiation effects on the stability of the $L1_2$-Ni_3Al nanoprecipitates for another project.

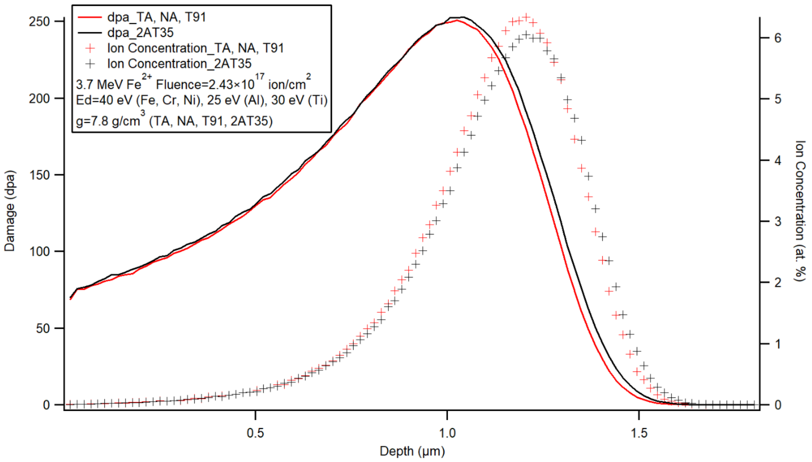

Figure 35. 3.7 MeV iron induced damage and implanted iron concentration in FTN1 (NA), FTT1 (TA), T91 (red). The damage and implantation depth profiles were calculated using the Kinchin-Pease Model in the SRIM software. *Ed* is atom displacement energy.

Irradiation temperature and flux are shown in Figure 36. Temperature is average readings of two thermocouples welded at opposite corners of the sample stage. Flux was calculated from ion beam current and beam confining aperture size (0.5 cm × 0.5 cm = 0.25 cm^2). Flux spikes resulted from spikes of ion current or possibly secondary electron currents. In run 2, there were high ion current / flux spikes, as shown in Figure 36b. The source of the beam instability was uncertain.

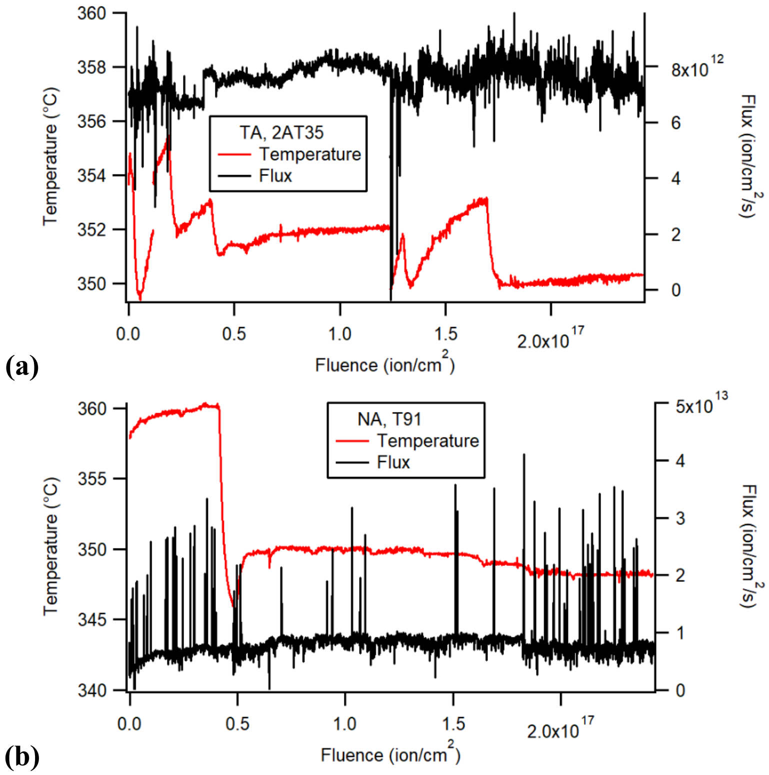

Figure 36. Temperature and flux during 3.7 MeV iron 350°C irradiation. (a) Irradiation run 1 of FTT1 (TA); (b) Irradiation run 2 of FTN1 (NA) and T91.

Figure 37 shows sample pictures after irradiation. Samples were partially irradiated as the irradiation area in one run was about 0.5 cm × 0.5 cm. There is no visible irradiation boundary on TA and 2AT35 as shown in Figure 37a. The irradiated area in Figure 37b is darker while unirradiated parts are of silver color.

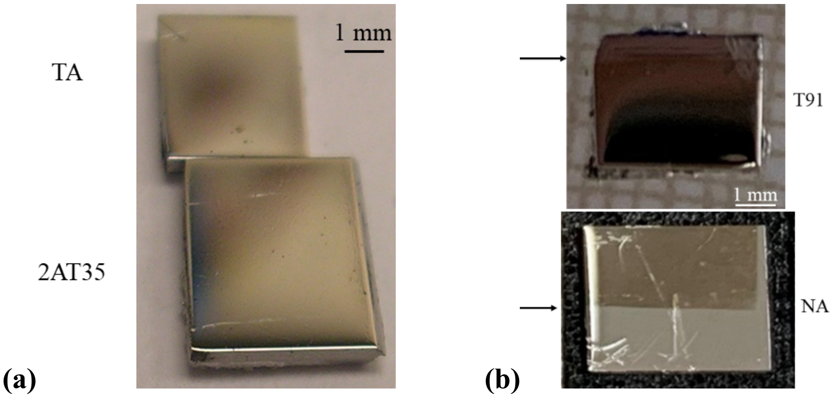

Figure 37. Samples after 350°C, 250 dpa Fe^{2+} irradiation. (a) Run 1 of FTT1 (TA). (b) Run 2 of T91 and FTN1 (NA). Arrows indicate irradiation boundary. The lower part of T91 and upper part of FTN1 (NA) are irradiated.

Figure 38 shows Al concentration measured with transmission electron microscopy (TEM) and EDS in NA and T91 after the irradiation. Following the red lines on the annular bright-field (ABF) images on Figure 38a-b, EDS depth profiles are shown in Figure 38c with Al peak concentration at depth of ~1 µm. It has to be high energy Al ions to reach this implantation peak depth. The ion beam for the irradiation of NA and T91 thus was possibly consisted of significant Al ions. Al concentration calculated with SRIM is shown in Figure 38c assuming Al^+ ions of 2.47 MeV and 4.86×10^{17} ion/cm^2.

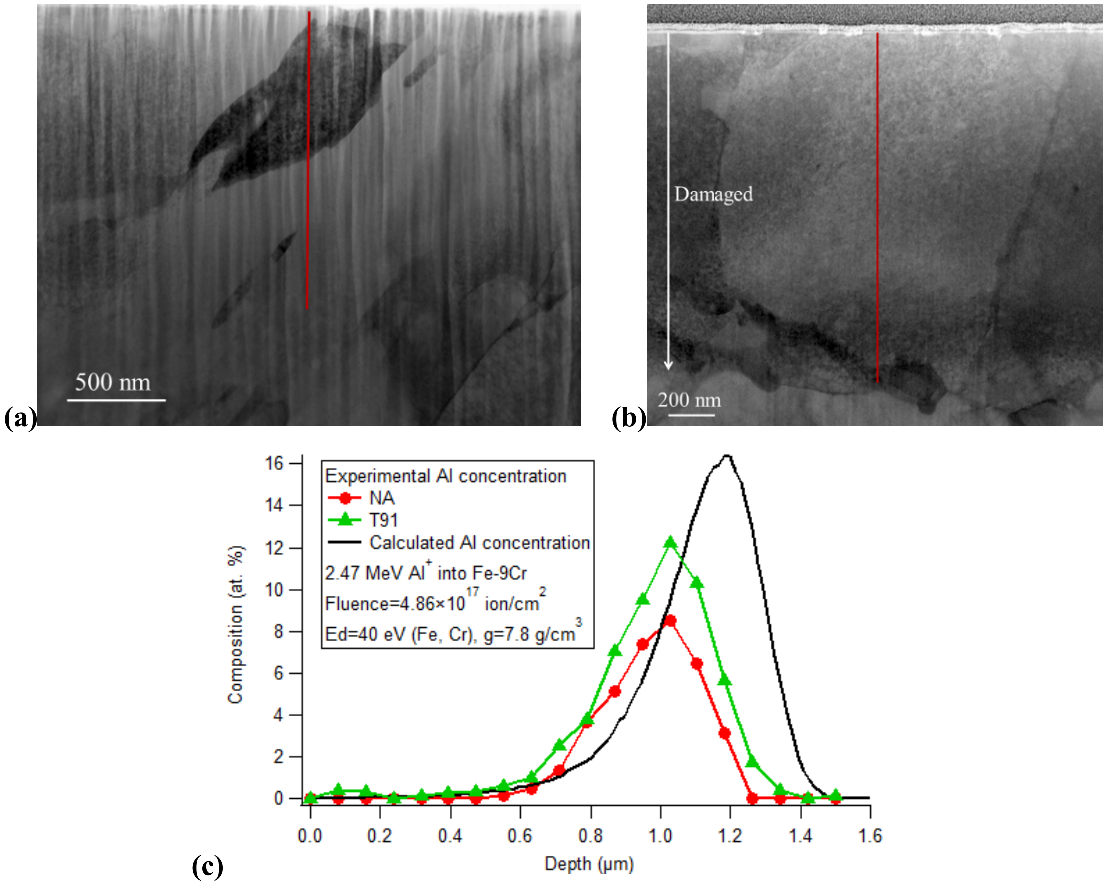

Figure 38. Al implantation in the 350°C irradiated FTN1 (NA) and T91 samples. ABF images of cross-sectional (a) FTN1 (NA) and (b) T91 with the red lines illustrating the EDS line scan paths for the (c) EDS depth profile and SRIM calculated Al composition from surface.

6.1.2 Fe^{2+} irradiation at 475°C

A new Fe cathode was used in the following two runs of 3.7 MeV Fe^{2+} irradiation of samples TA (run 3), NA and T91 (run 4) at 475°C to a peak damage of ~250 dpa with defocused, non-rastering ion beam. Temperature was measured by average of two-thermocouple readings attached to the opposite corners of the irradiation sample stage. Irradiation parameters are the following:

- **Energy and Irradiating Ion Species:** defocused 3.7 MeV Fe^{2+} defocused beam. Cu implantation is found, as shown in Figure 41.
- **Damage Level**: peak damage ~250 dpa at ~1.0 µm depth, as shown in Figure 35.
- **Fluence**: 2.43×10^{17} ion/cm^2 (run 3), 2.39×10^{17} ion/cm^2 (run 4).

- **Irradiation Temperature**: 474 ± 2°C for run 3 on TA, as shown in Figure 39a, and 474 ± 2°C for run 4 on NA and T91, as shown in Figure 39b.
- **Irradiation Flux**: $(8 \pm 2) \times 10^{12}$ ion/cm^2/s (run 3, Figure 39a) and $(7 \pm 1) \times 10^{12}$ ion/cm^2/s (run 4, Figure 39b).
- **Vacuum/Base Pressure**: 4×10^{-7} Torr (base), $2 \times 10^{-6} – 4.5 \times 10^{-7}$ Torr (irradiation vacuum)

To achieve a peak damage of ~250 dpa, a fluence of 2.4×10^{17} Fe^{2+}/cm^2 was used. The peak damage took place at ~1.0 μm under surface. Irradiation temperature and flux are shown in Figure 39. Flux was calculated from ion beam current and beam confining aperture size (0.5 cm × 0.5 cm = 0.25 cm^2). Flux spikes resulted from spikes of ion current or possibly secondary electron currents.

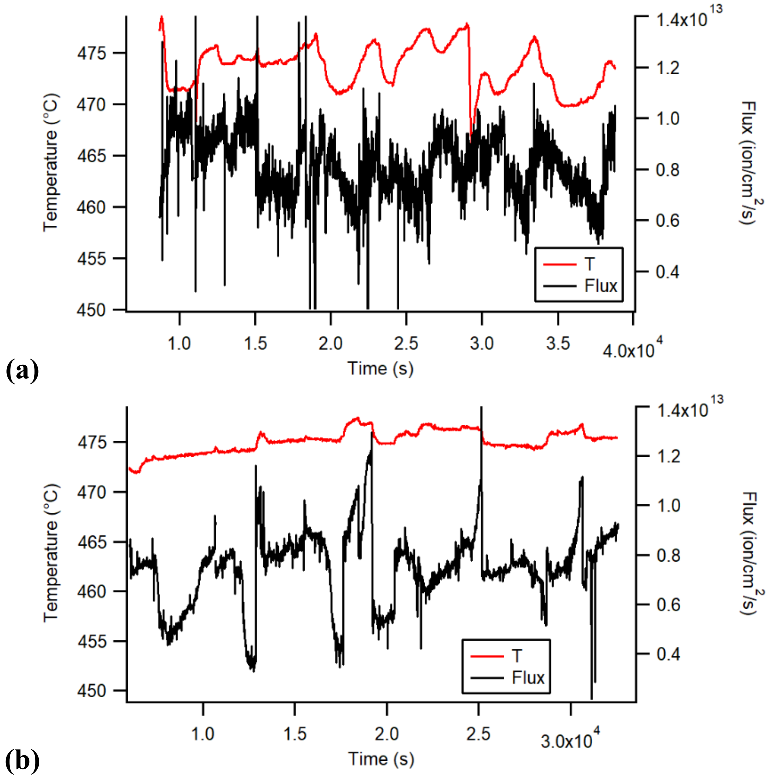

Figure 39. Temperature and flux during 3.7 MeV iron 475 °C irradiation. (a) Irradiation run 3 of FTT1 (TA). (b) Irradiation run 4 of FTN1 (NA) and T91.

Figure 40 shows sample pictures after irradiation. Samples were partially irradiated as the total irradiation area for two samples was about 0.5 cm × 0.5 cm. The irradiated area is darker while unirradiated parts are of silver color.

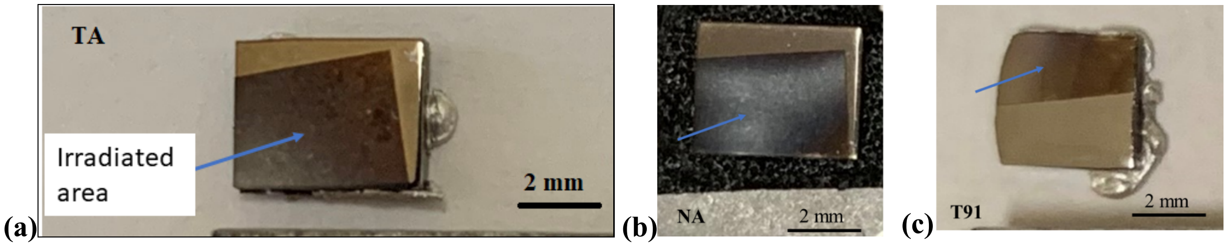

Figure 40. Samples after 475 °C, 250 dpa Fe^{2+} irradiation: (a) FTT1 (TA); (b) FTN1 (NA); (c) T91. Arrows indicate irradiation area.

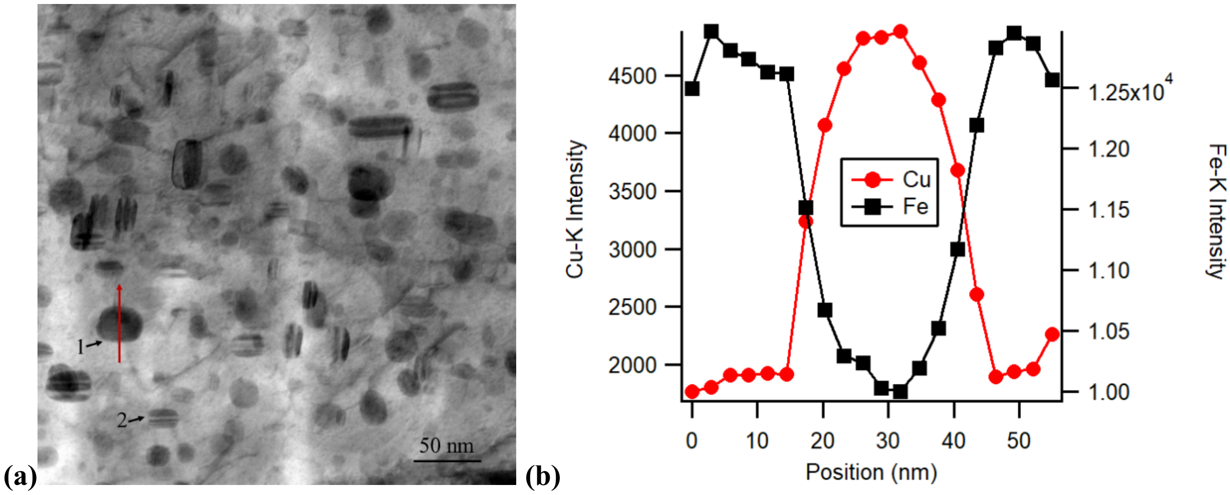

Figure 41. (a) Cross-sectional ABF image and (b) EDS line scan profile across the red line in (a) of Fe^{2+}-irradiated FTN1 (NA) up to 250 dpa at 475°C showing Cu-rich particles at ~1.1 µm depth.

Cu is the material of cathode jacket. It is possible that the injector and switch magnets did not correctly select Fe^{2+} only but instead mixture of Fe^{2+} and Cu^{2+}. This issue is under inspection. On the other hand, no Al implantation is found from the run 4 samples.

In summary, defocused beam ion irradiation was employed. However, two issues arose with the defocused Fe^{2+} ion beam irradiations:

- Al ion contamination in NA and T91 irradiated at 350°C. It is associated with Fe depletion in the cathode. With a new Fe cathode, there is no Al found in the 475°C irradiated sample NA.
- Cu ion contamination in NA irradiated at 475°C. Cu is the material of cathode jacket. We are inspecting magnetic settings to solve the issue.

The comparison of FTN1 (NA) and FTT1 (TA) samples to the reference T91 samples irradiated under the same conditions could provide meaningful indications regarding their relative radiation resistance despite the unexpected Al/Cu contamination preventing the results from direct comparison to literature data of similar steels.

6.2 RASTERING BEAM

The irradiation condition of the rastering beam ion irradiation was:

- **Energy and Irradiating Ion Species:** 4.0 MeV Fe^{2+} irradiation
- **Damage Level:** peak damage 217 dpa at 1.11 µm depth, as shown in Figure 42.
- **Irradiation Temperature:** about 475°C (474 ± 3°C for run 1 as shown in Figure 43a, and 472 ± 2°C for run 2 as shown in Figure 43b).
- **Irradiation Flux:** (6.4 ± 0.8) × 10^{12} ion/cm^2/s (run 1) and (6.6 ± 0.9) × 10^{12} ion/cm^2/s (run 2).
- **Vacuum/Base Pressure:** 5 × 10^{-7} Torr (base), 2.6 × 10^{-6} – 5.8 × 10^{-7} Torr (irradiation vacuum)

Figure 42 shows the damage profile of 4.0 MeV Fe^{2+} irradiation in BL-Nb with a nominal composition of 79Fe-12Cr-3W-3Ni-3Al. To achieve a damage of 100 dpa at 0.48 µm where the damage profile is relatively flat (damage vs. depth slope is relatively small), a fluence of 2.14×10^{17} Fe^{2+}/cm^2 was used. The peak damage is 217 dpa at 1.1 µm under surface. Similar calculation was conducted for TTZ2M, which generated nearly identical damage and implantation depth profiles.

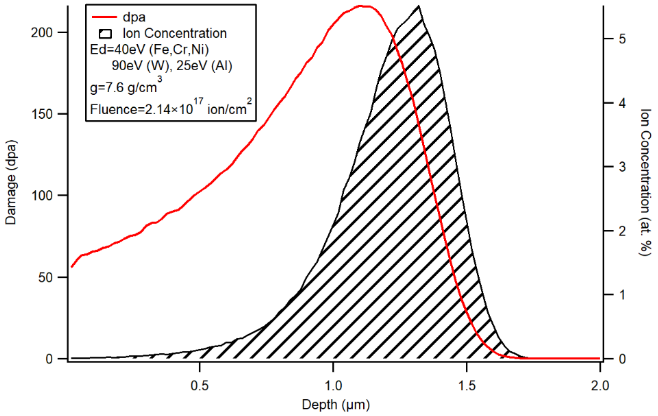

Figure 42. 4 MeV iron induced damage in BL-Nb (79Fe-12Cr-3W-3Ni-3Al). The damage and implantation profiles were calculated using the Kinchin-Pease Model in the SRIM software. *Ed* is atom displacement energy.

Irradiation temperature and flux are shown in Figure 43. Temperature is average value of two-thermocouple readings from opposite corners of the sample stage. Flux was calculated from ion beam current and beam scanning area (2 cm^2). Occasional positive or negative flux spikes resulted from spikes of ion current or possibly secondary electron currents. In run 1, temperature is 474 ± 3°C and flux is $(6.4 \pm 0.8) \times 10^{12}$ ion/cm^2/s. In run 2, temperature is 472 ± 2°C and flux is $(6.6 \pm 0.9) \times 10^{12}$ ion/cm^2/s.

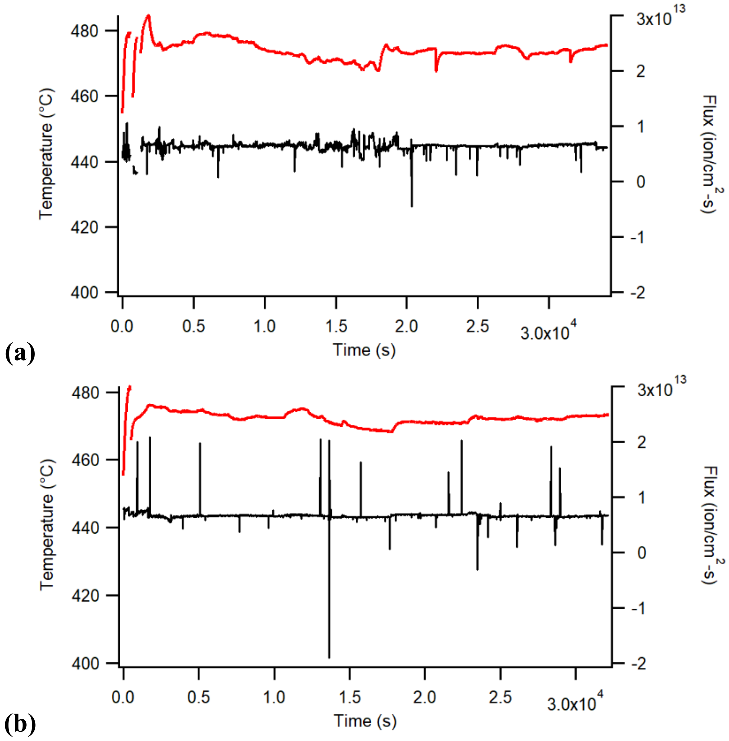

Figure 43. Temperature and flux during 4 MeV iron irradiation (a) run 1 and (b) run 2 of BL-Nb.

6.3 NANOINDENTATION

A Hysitron TI-950 TriboIndenter with a Berkovich tip and a High Load transducer was used to measure hardness of alloys at a displacement control mode. Ten indentation measurements were performed at each displacement. Average and standard deviation results are reported in Figure 44. Measurement was made on both irradiated and unirradiated area (masked during irradiation). The masked area did not experience irradiation but experienced the same thermal history as the irradiated area. Hardness of unirradiated and irradiated area are plotted in Figure 44 for the defocused-beam-irradiated up to 250 dpa for (a) NA at 350°C, (b) T91 at 350°C, (c) NA at 475°C, (d) T91 at 475°C, and the rastered-beam-irradiated up to 220 dpa for (e) TTZ2M and (f) BL-Nb at 475°C. The sample T91 irradiated at 350°C has a very small unirradiated area near the sample edge that did not have reliable hardness result. Therefore, results of as-received T91 are plotted in Figure 44b with the irradiated hardness.

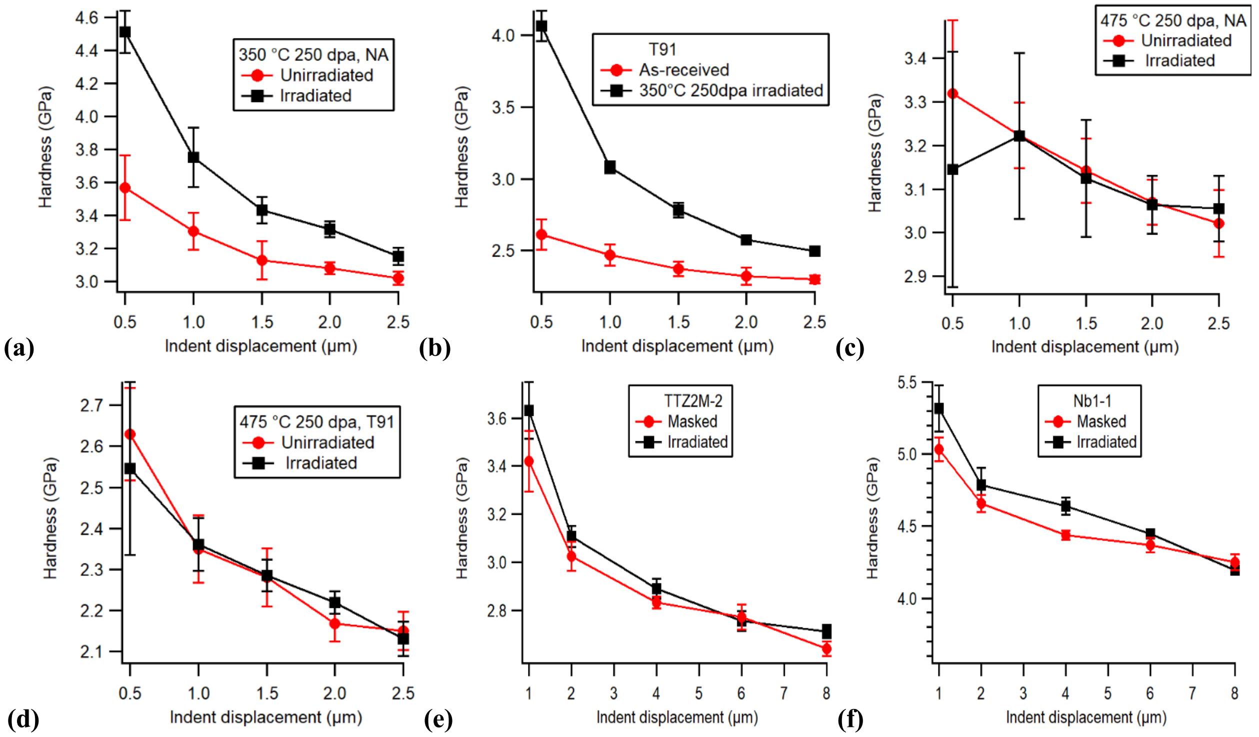

Figure 44. Nanoindentation hardness of ion-irradiated samples: defocused-beam up to 250 dpa at 350°C for (a) FTN1 (NA) and (b) T91 and at 475°C for (c) FTN1 (NA) and (d) T91; rastered-beam up to 220 dpa at 475°C for (e) TTZ2M and (f) BL-Nb.

The results of irradiation induced hardening for FTN1 (NA), T91, TTZ2M, and BL-Nb are:

- Ion irradiation up to 250 dpa (peak damage depth at ~1 µm) at 350°C increased the hardness of FTN1 (NA) by 26.4 ± 7.8 %, as measured at 0.5 µm indent displacement, which is about half of the hardening in T91 by 55.7 ± 7.5 %, assuming the hardness of as-received T91 does not change significantly after heating at 350°C for 10.6 hours (irradiation timespan).
- Hardness appears similar for unirradiated and irradiated FTN1 (NA) and T91 up to 250 dpa at 475°C, except for the larger deviations of the hardness data of NA.
- The rastered-beam-irradiated TTZ2M and BL-Nb up to 220 dpa at 475°C showed comparable slight hardening by ~6 ± 5 % and ~6 ± 3 %, respectively, as measured at 1 µm indent displacement. The

radiation-hardening of TTZ2M and BL-Nb is believed to be measurably larger than the defocused-beam-irradiated FTN1 (NA) and T91 because the hardening at 0.5 µm of TTZ2M and BL-Nb (not measured) is expected to be greater than that at 1 µm.

In summary, irradiation at 350°C to 250 dpa induced significant hardening in both FTN1 (NA) and T91. Hardening in FTN1 (NA) was about half of that in T91. Irradiation up to 250 dpa at 475°C did not induce noticeably hardening in FTN1 (NA) and T91, but the rastered-beam-irradiated TTZ2M and BL-Nb showed slightly larger hardening at 475°C.

6.4 MICROSTRUCTURES

6.4.1 FTN1 (NA) irradiated at 350°C

Figure 45 shows cross-sectional ABF images of the 350°C-irradiated FTN1 (NA) sample. Irradiation damaged the sample from surface to ~1.5 µm deep, as denoted in Figure 45a. There are dislocation loops in the damaged region, as shown in dark spot contrast along [100] zone in Figure 45b at 0.54 µm depth. The size of dislocation loops that are visible under [100] zone is 3.0 ± 1.5 nm with a dislocation loop density of 9×10^{22} m^{-3}.

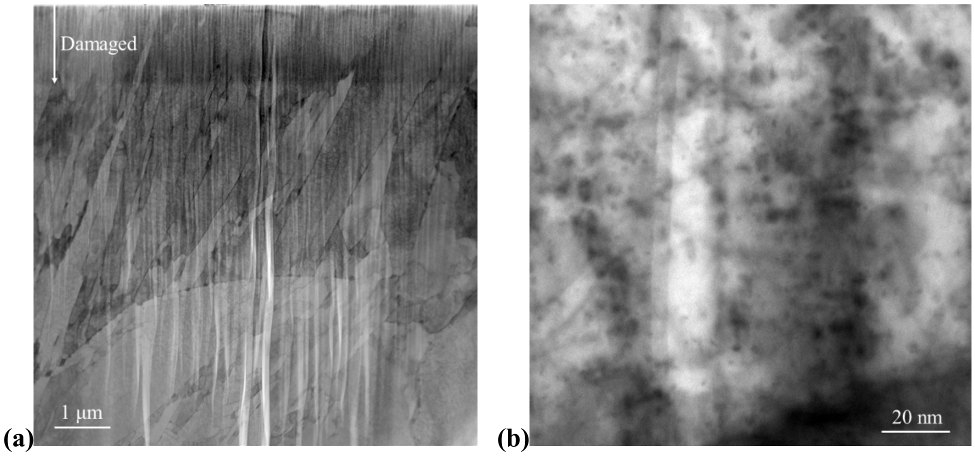

Figure 45. Cross-sectional ABF images of FTN1 (NA) after 350ºC ion irradiation: (a) Overview and (b) Damaged region at 0.54 µm depth with normal direction parallel to [100].

Precipitates in FTN1 (NA) are shown in Figure 46. Two types of precipitates were found in the undamaged region, as shown in Figure 46a: $M_{23}C_6$ (about 97Cr-2.5W-0.5V metal components, at. %), and finer Ti, W, Nb-rich carbide (about 72Ti-25W-3Nb metal components, at.%). In the damaged region as shown in Figure 46b, Ti, W, Nb-rich carbide has not been found. It may be because the contrast of dislocation loops made it harder to find these particles. $M_{23}C_6$ remains crystalline at the irradiation depth of 1.11 µm (~240 dpa).

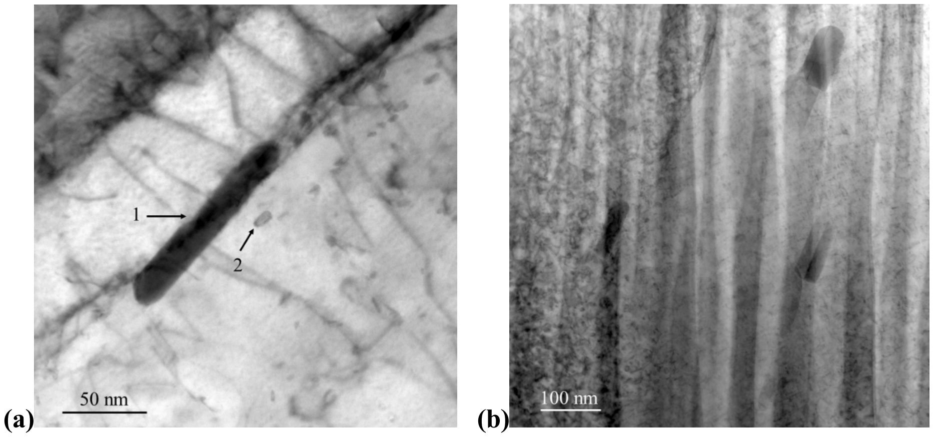

Figure 46. Precipitates in FTN1 (NA): (a) Undamaged region with the arrow-pointed 1 as $(Cr,W)_{23}C_6$ and 2 as a Ti, W, Nb-rich carbide; (b) Damaged region at 0.54 µm showing the particles of $M_{23}C_6$.

In summary, the FTN1 (NA) sample has lath grain boundaries, dislocations, Cr-rich $M_{23}C_6$ and fine Ti, W-rich carbides. Irradiation up to 250 dpa at 350°C created dislocation loop sizes of 3.0 ± 1.5 nm with a dislocation loop density of 9×10^{22} m^{-3} at 0.54 irradiation depth (~140 dpa). No cavities were found in the irradiated FTN1 (NA).

6.4.2 FTT1 (TA) irradiated at 350°C

Figure 47 shows the cross-sectional ABF images of FTT1 (TA) irradiated up to 250 dpa at 350°C. Irradiation generated a damaged zone about 1.1 µm and beyond from surface as indicated by the brighter horizontal band in Figure 47a. Tempered martensite structure retained well after the irradiation. Few dislocation loops, primarily shown as tiny black dots are shown in Figure 47b, which are noticeably less dense than that in Figure 46b for FTN1 (NA). Higher magnification characterization is needed to have statistical loop size and density.

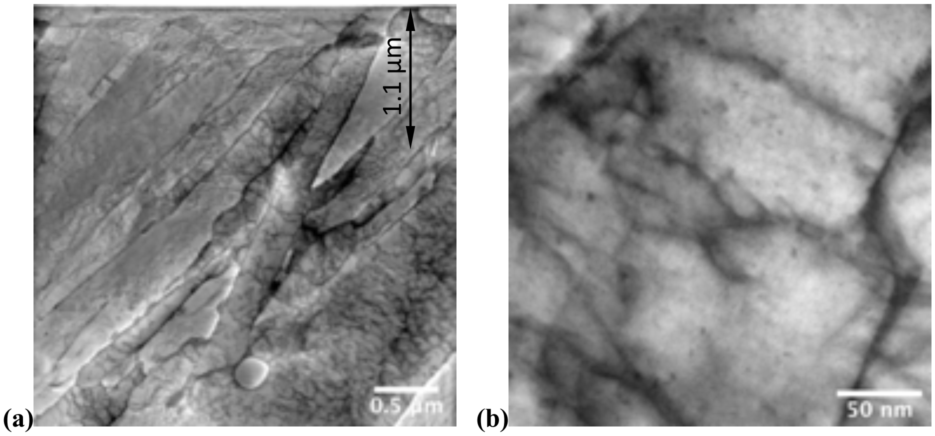

Figure 47. Cross-sectional ABF images of FTT1 (TA) after 350°C ion irradiation: (a) Overview and (b) Damaged region at 0.5 µm depth with normal direction parallel to [100].

Precipitates in FTT1 (TA) have Cr-rich $M_{23}C_6$ and Ti-rich MX. Figure 48 shows a DF image using the weak reflection between the (200) two-beam near the [001] zone as shown in the inset, which exhibits ultrafine precipitates with sizes < 5 nm and a density of 4.2×10^{21} m^{-3} in this condition, which are believed to be the Ti-rich MX.

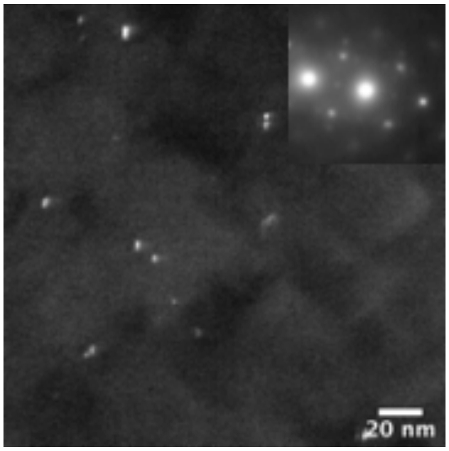

Figure 48. DF image showing MX type precipitates in FTT1 (TA) after 350°C ion irradiation at 0.6 µm depth.

In summary, the FTT1 (TA) sample retained lath sub-boundaries as the FTN1 (NA) sample after the irradiation. Dislocation loops were generated by the irradiation but appears not as dense as that generated in the FTN1 (NA) sample. The precipitates of Cr-rich $M_{23}C_6$ and Ti-rich MX retained after the irradiation without noticeable changes. The Ti-rich MX precipitates have ultrafine sizes < 5 nm with a density of 4.2×10^{21} m^{-3} in one of the four imaging conditions of {200} two-beam near the [100] zone axis.

6.4.3 T91 irradiated at 350°C

Figure 49 shows the cross-sectional ABF images of T91 irradiated up to 250 dpa at 350°C. Irradiation damaged the ~1.5 µm deep surface region and created dislocation loops, which eliminated nearly all the lath/block/packet sub-boundaries. Figure 49b shows an image of dislocation loops along <111> zone. The size of loops that are visible along <111> is 5.5 ± 2.6 nm, which have a density of 4.0×10^{22} m^{-3}.

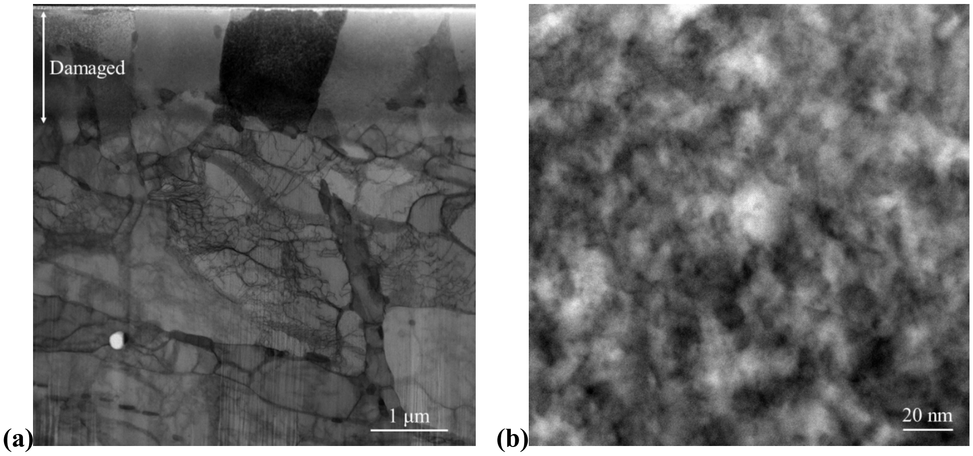

Figure 49. Cross-sectional ABF images of T91 after irradiation at 350°C: (a) Overview and (b) Dislocation loops under <111> zone at an irradiation depth of 0.55 µm.

Precipitates in T91 are shown in Figure 50. Three types of precipitates were observed in the undamaged T91: Cr-rich $M_{23}C_6$ (about 97Cr-2.8Mo-0.2V metal components, at. %), V-rich M(C,N) (about 97V-3Nb metal components, at. %), and Nb-rich M(C,N) (about 80Nb-20V metal components, at. %). In the damaged region, (V,Cr,Nb)(C,N) precipitates were found: one about 69V-29Cr-2Nb metal components at 0.84 µm depth, one 26V-60Cr-14Nb at 0.67 µm depth, and one 18.6Nb-80Cr-1.4V at 0.97 µm. The significant Cr partition in the M(C,N) type precipitates suggest the occurrence of phase transformation from MX to Z-phase, e.g., simple phase of CrVN and/or CrNbN.

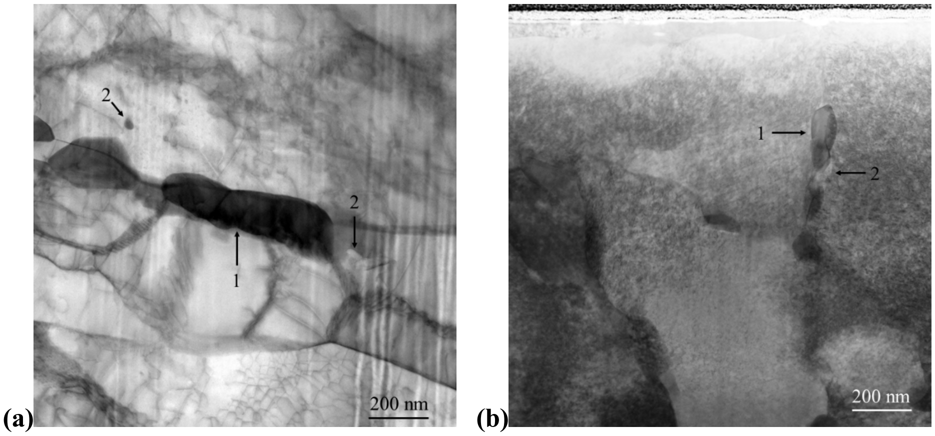

Figure 50. Precipitates in T91. (a) Undamaged. (b) 350 °C irradiation damaged region. 1 is $M_{23}C_6$. 2 is V, Nb-rich MX.

In summary, irradiation up to 250 dpa at 350°C generated dislocation loops in T91. The loops have sizes of 5.5 ± 2.6 nm at 0.55 µm depth under <111> zone with a density of 4.0×10^{22} m^{-3}. T91 has larger dislocation loops and a smaller density than FTN1 (NA). There are Cr-rich $M_{23}C_6$ and (V,Nb)(C,N) in T91. Irradiation appears to attract Cr into the MX particles (V,Nb)(C,N) to 30 – 80 at. % Cr in the metal component of the particles, suggesting phase transformation into Z-phase. No cavities were found in the irradiated T91.

6.4.4 FTN1 (NA) irradiated at 475°C

Figure 51 shows cross-sectional ABF images of ion-irradiated FTN1 (NA) up to 250 dpa at 475°C. The dark dispersed features near the end of the irradiation zone are Cu precipitates, with a higher magnification image shown in Figure 41a. Type <100> dislocation loops were present in the damaged region (Figure 51b, 0.55 µm depth). The loops have sizes of 4.0 ± 2.7 nm with a density of 4.1×10^{22} m^{-3}. No cavities were found in the 475°C irradiated FTN1 (NA) sample.

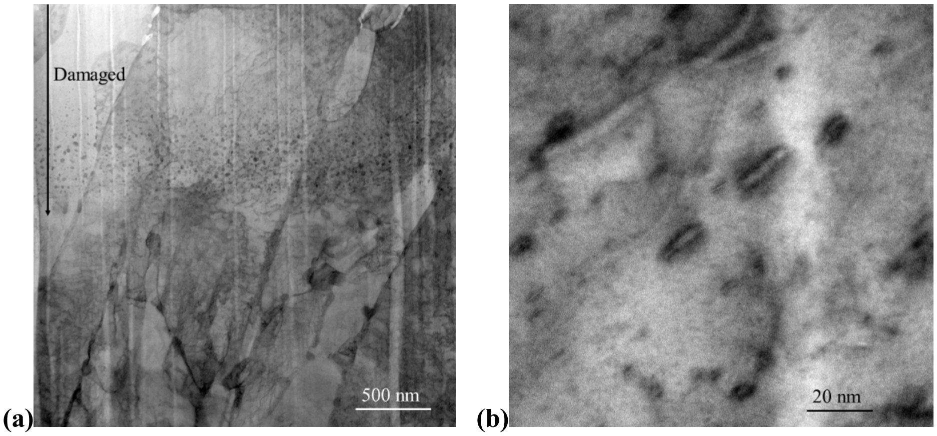

Figure 51. Cross-sectional ABF images of FTN1 (NA) irradiated at 475°C: (a) Overview of damaged (top part) and undamaged structure; (b) <100> dislocation loops at 0.55 µm depth.

6.4.5 FTT1 (TA) irradiated at 475°C

Figure 52 shows cross-sectional ABF images of ion-irradiated FTT1 (TA) up to 250 dpa at 475°C. Similar to FTN1 (NA) in Figure 51a, Cu precipitates are dispersed at ~1.1 µm depth in Figure 52a. A dense dislocation loops are shown in Figure 52b at 0.7 µm depth. Precipitates are also believed to be present in Figure 52b as suggested by the satellite secondary reflections in Figure 52c taken from the same area of Figure 52b. The layout of the secondary reflections from precipitates in Figure 52c is different from that in the inset of Figure 48, which may suggest different types of precipitates. The precipitates are generally difficult to be distinguished because of the presence of dislocation loops. Therefore, conclusive statistical analysis for the sizes and densities of dislocation loops and precipitates are not achievable. Further investigations are needed to clarify the features. No cavities were found in the sample.

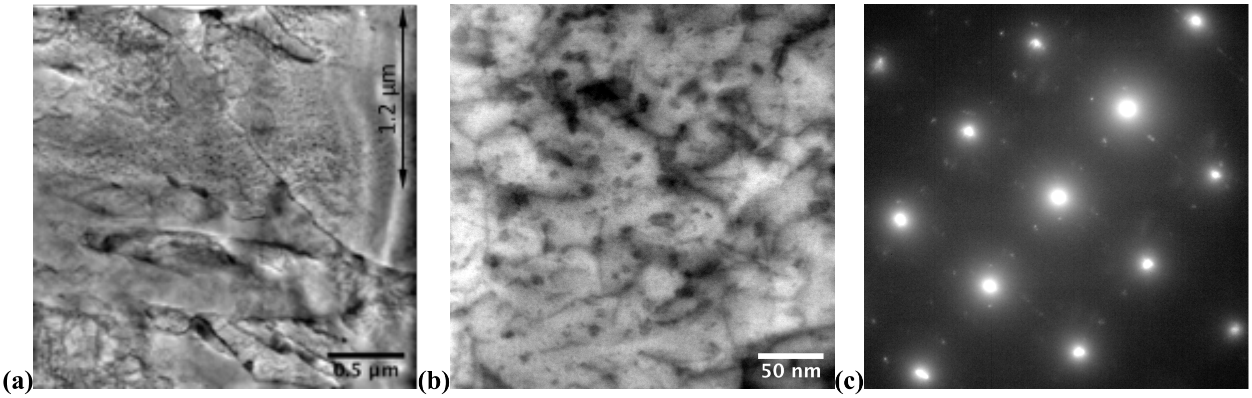

Figure 52. Cross-sectional ABF images of FTT1 (TA) irradiated at 475°C: (a) Overview of damaged (top part) and undamaged structure; (b) Dislocation loops at 0.7 µm depth and (c) corresponding SAED pattern.

6.4.6 T91 irradiated at 475°C

Figure 53 shows a cross-sectional HAADF image of T91 irradiated up to 250 dpa at 475°C under the <111> zone axis. Dislocations are shown in the damaged region, but no cavities were found.

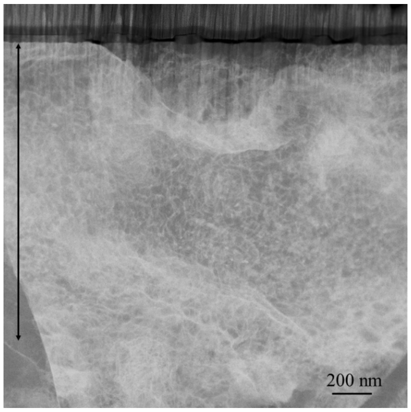

Figure 53. Cross-sectional HAADF image of T91 irradiated at 475°C along the <111> zone. Arrow indicates damage depth.

6.4.7 TTZ2M irradiated at 475°C (rastering beam)

Figure 54 shows the microstructures of TTZ2M irradiated up to 220 pda at 475°C using a rastering beam. The irradiated generated ~1.7 µm depth of damage layer as shown in Figure 54a. At ~0.6 µm depth, corresponding to ~120 dpa, a high-density dislocation loops are shown in Figure 54b, together with ultrafine (11.5 ± 7.3 nm) precipitates with a density of 3×10^{21} m^{-3} as shown in Figure 54c.

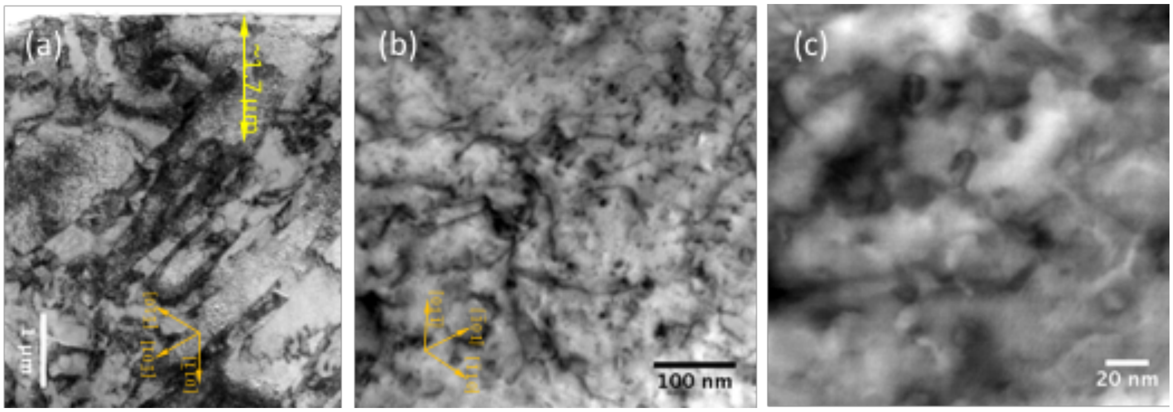

Figure 54. TTZ2M irradiated at 475°C along the <111> zone: (a) BF-TEM overview image and (b-c) ABF-STEM images at ~0.6 µm depth.

6.4.8 BL-Nb irradiated at 475°C (rastering beam)

Figure 55 shows B2 precipitates in the unirradiated region of the sample. The DF TEM image in Figure 55a was taken from a [100] zone axis as shown in the inset, which reveals the B2 phase as bright particles with sizes < 20 nm uniformly dispersed in the matrix. The diffraction pattern indicates the coherency between the B2 phase (simple cubic with one element on the corner and the other element in the body center) and the bcc matrix. The high magnification HAADF image in Figure 55b shows the B2 particles in dark shade with a white peripheral halo. The HAADF contrast suggests low-Z (mass) nature of the B2 particles, which is confirmed by its Ni and Al enrichment from the EDS line scan (Figure 55c) across a representative B2 particle pointed by an arrow in Figure 55b. Compositional values of Fe, Cr, W fluctuate around zero inside the particle possibly due to small particle size compared to the sample thickness. Averaging the concentration of seven B2 particles yielded Ni (53 ± 4) – Al (47 ± 4) in atomic percent. Scattered minor enrichment in Nb was observed at particles' center, which is consistent with the thermodynamically calculated composition of Ni(Al,Nb) type B2 phase. B2 particles show a periphery of white contrast in HAADF images and dark contrast in ABF images (not shown here), indicating strain at the particle/matrix interface.

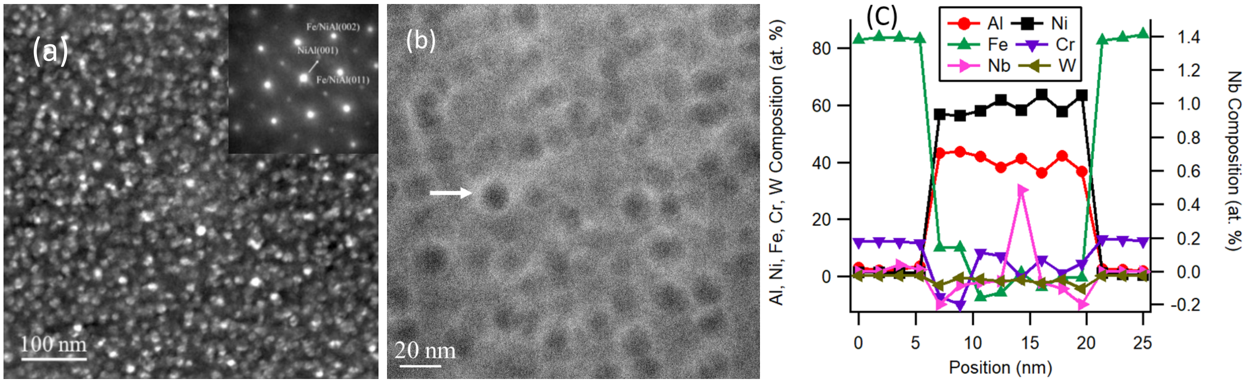

Figure 55. B2-NiAl precipitates in the unirradiated region: (a) DF-TEM image from the [100] zone as indicated in the electron diffraction pattern of the inset, (b) HAADF image, and (c) EDS line scan compositional profiles across the particle pointed by the arrow in (b).

The structure of B2-NiAl particles after Fe^{2+} ion irradiation at 475 °C is shown in Figure 56. The cross-sectional regions at depth of 0.15–0.6 µm and 1.15–1.6 µm, corresponding to about 68–115 dpa and 210–10 dpa, respectively, are shown in Figure 56a and b. The top side of the images is close to the irradiated surface. The micrographs were imaged using the (001)$_{\mathrm{NiAl}}$ reflection from the [100] zone as shown in the inset of Figure 56a. The irradiation did not alter the crystallinity of the B2 phase particles. Some coarser particles are seen in the top part of Figure 56a from 0.15 to ~0.3 µm depth, which might be influenced by irradiation surface effects [11,12]. The average size of B2-NiAl particles in the region encompassing 0.3 to 0.6 µm depth was characterized to be 11.3 ± 0.2 nm with a number density of 1.5×10^{22} m^{-3} in Figure 56a (~81–115 dpa), which suggests that the particles experienced slight diminution and an increase in number density compared to that in the unirradiated condition (Figure 55a) where the corresponding values were, a size of 12.3 ± 0.1 nm and number density of 9.3×10^{21} m^{-3}. In contrast, the B2-NiAl particles appeared with lower contrast at the top part of Figure 56b which is taken at a greater depth of 1.15 to 1.3 µm approximately corresponding to the range from peak damage to peak implanted Fe. Beyond this, B2-NiAl particle size became 14.0 ± 0.2 nm, which is larger than that in the unirradiated region, with number density of 7.1×10^{21} m^{-3}. Figure 56c shows a high-resolution HAADF image of a B2-NiAl particle, taken along the [100] zone illustrated in the inset for a fast Fourie transform (FFT) of the original image, at depth of 0.86 µm where the damage level was about 170 dpa. The HAADF image was smoothed, together with an applied mask to emphasize atomic columns, which shows Ni columns in a brighter contrast compared to the neighboring Al inside the particle. All the columns of the particle aligned well with the matrix {002} planes, verifying full coherency between the irradiated particle and matrix. The wavering contrast in the particle and matrix was induced by local strains.

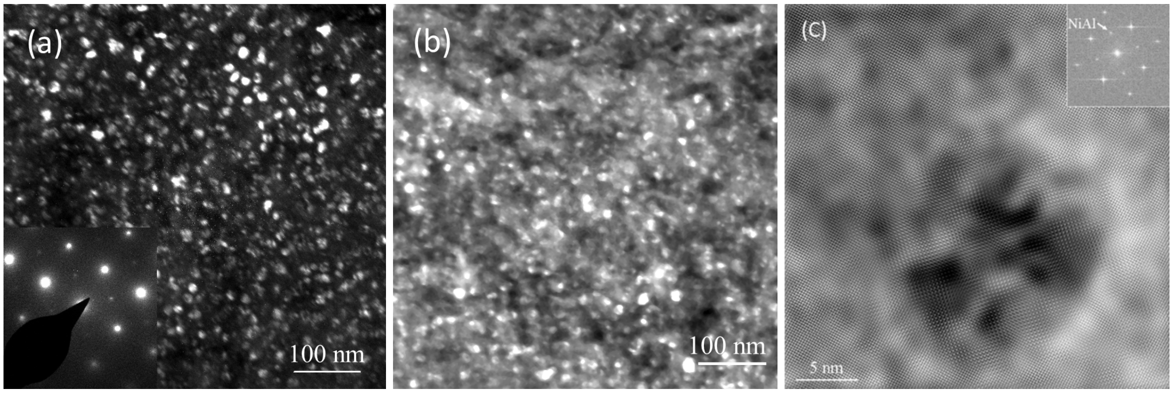

Figure 56. Images of B2-NiAl particles in the irradiated region: DF-TEM images at (a) 0.15–0.6 µm depth and (b) 1.15–1.6 µm depth. The images were taken with the (001)$_{\mathrm{NiAl}}$ diffraction from the [100] zone axis as shown in the inset of (a); (c) HAADF image at 0.86 µm from surface with the inset of an FFT of the original image.

Figure 57 shows cross sectional ABF images of BL-Nb irradiated up to 220 dpa at 475°C. The irradiation generation a damage layer ~1.6 µm thick in Figure 57a, close to SRIM calculation result shown in Figure 42. Coarse micron-scale particles and small particles ~100 nm large are present both inside grains and along grain boundaries. Figure 57b-d show electron diffraction and EDS characterization of undamaged particles. Nanobeam diffraction on particle A in Figure 57b-c shows a Fe$_2$Nb-like crystalline phase. The particle is coherent with matrix and is oriented as particle <011> // matrix <100>, particle (100) // matrix (01$\bar{1}$), and particle ($\bar{1}2\bar{2}$) // matrix (011). The composition of particle B in Figure 57b is Fe (55.4 ± 3.4) – Cr (11.9 ± 1.9) – Nb (21.4 ± 2.1) – W (11.3 ± 1.8) (at. %), correspond to a Laves phase (FeCr)$_2$(NbW).

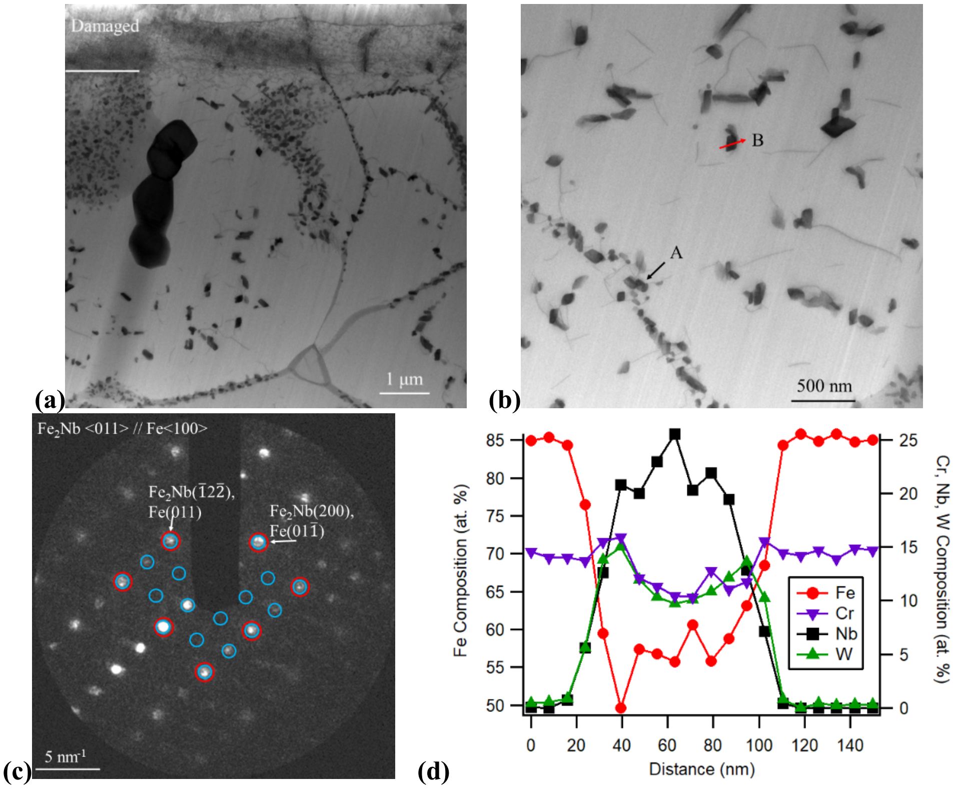

Figure 57. TEM characterization of BL-Nb after Fe^{2+} ion irradiation at 475°C: (a-b) Cross-sectional ABF images along <100>; (c) Nanobeam SAED pattern of particle A in (b) with red and blue circles indicating matrix and particle diffraction spots, respectively; (d) EDS measured compositional profile along particle B in (b).

Figure 58a shows a cross-sectional image of BL-Nb near the boundary of damaged region. Damage level is ~200 dpa at the image center. Irradiation induced pronounced dislocations and dislocation loops. The three particles pointed by arrows do not have distinctive boundaries, unlike the undamaged particles in lower part of the image. Surrounding the 100 nm-scale damaged particles are nanometer-scale fine precipitates, as shown in Figure 58b. The damaged particle in Figure 58b is ~130 nm wide. Figure 58c-d show that it has a core ~50 nm wide enriched in Cr, Nb, W, and C. It has a remaining core of Laves phase $(FeCr)_2(NbW)$.

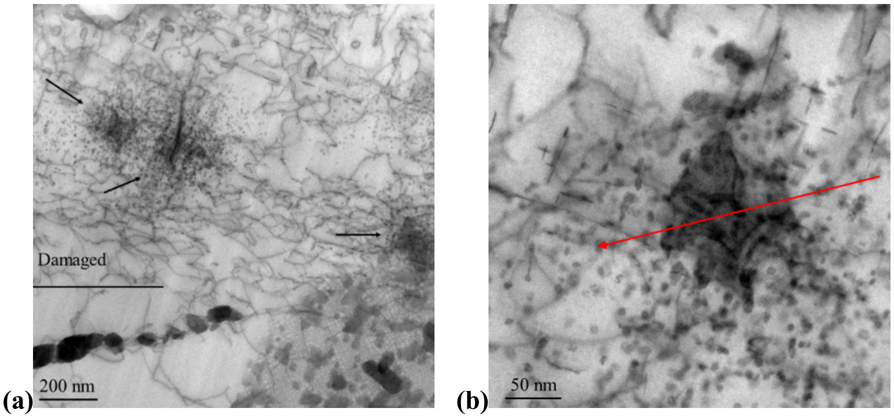

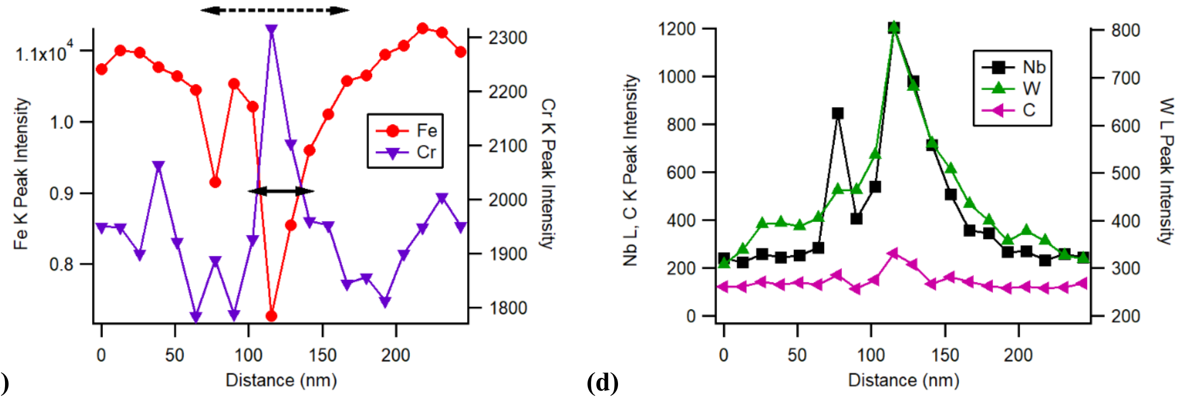

Figure 58. TEM characterization of irradiated particles in BL-Nb after Fe^{2+} ion irradiation at 475°C: (a) ABF image along <100> with the image center at 1.2 µm depth (~200 dpa); (b) ABF image along <100> with the image center at 0.83 µm depth (~164 dpa); (c-d) EDS peak intensity profile along the arrow line cross the damaged particle in (b). Dashed and solid arrows in (c) indicate widths of particle and core, respectively.

Figure 59 shows nanometer-sized precipitates surrounding damaged Laves phase particles as shown in Figure 58b. Figure 59a-b examine one precipitate 300 nm away from the damaged Laves phase particle. The damage level at Figure 59a area is ~180 dpa. EDS analysis shows the particle is composed of Nb, Cr, N and C (Carbon EDS intensity is not shown here). Figure 59c is a HAADF image of another particle along matrix <100> orientation at ~150 dpa. Two major atomic column plane spacings in the particle are 0.30 nm and 0.26 nm with 55° between planes. It matches with MX phases NbC <110>, NbN <110>, or Z-phase CrNbN <221>. Combined with the EDS analysis, CrNbN phase is suggested.

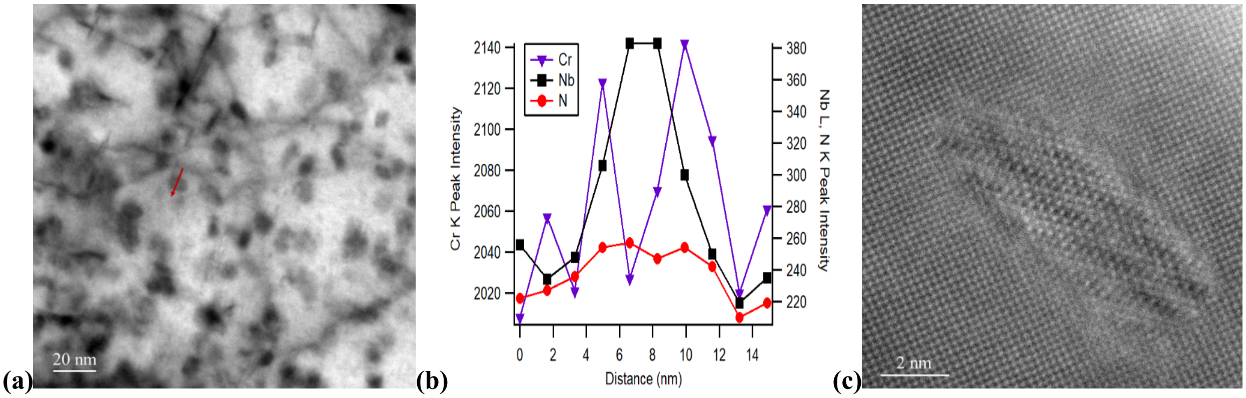

Figure 59. Irradiation induced particles. (a) ABF image at 0.9 µm depth, about 180 dpa. (b) EDS peak intensity profile along the arrow in (a). (c) HAADF image of a particle at 0.78 µm depth, about 150 dpa.

Irradiation damage to big micron-size particles is exemplified in Figure 60. The particle in Figure 60a was partially damaged. A and B are two points, undamaged and damaged, respectively. The undamaged part of the particle shows a Fe_2Nb <$42\bar{3}$> electron diffraction pattern as shown in Figure 60b. EDS verifies the Laves particle to be $(FeCr)_2(NbW)$. Irradiated part is amorphous, as shown by the lower diffraction in Figure 60b. The boundary of crystalline/amorphous regions is at 1.5 µm depth where damage level is ~30 dpa. Composition of the particle is Fe (66.7 ± 0.9) – Cr (8.3 ± 0.5) – Nb (20.0 ± 0.8) – W (5.0 ± 0.1) (at. %) for the crystalline phase, and Fe (67.5 ± 0.4) – Cr (8.5 ± 0.3) – Nb (19.0 ± 0.6) – W (5.0 ± 0.2) (at. %) for the amorphous phase.

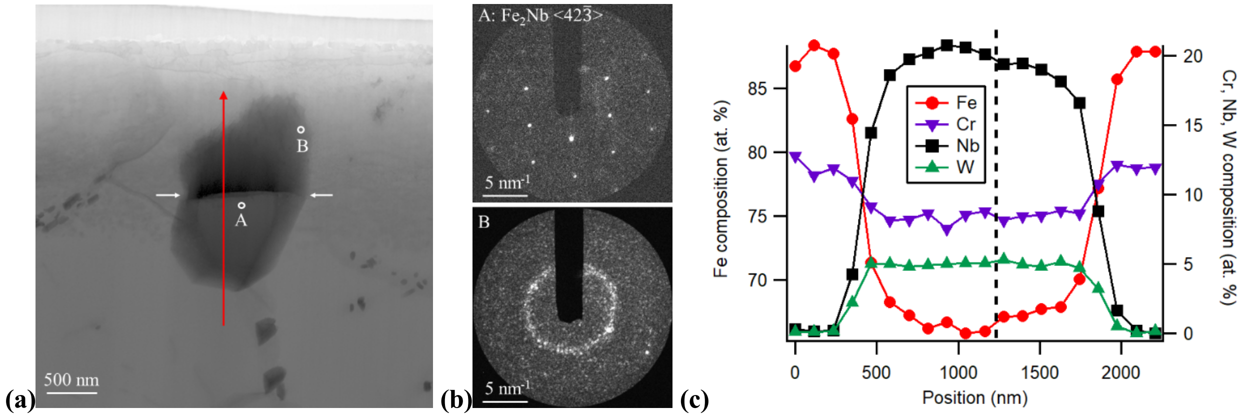

Figure 60. TEM characterization of a partially damaged micron-scale particle: (a) ABF image showing a contrast line inside the particle, as indicated by two short white arrows, at 1.5 µm depth (~30 dpa near the end of damage range); (b) Nanobeam electron diffraction patterns of points A and B labeled in (a); (c) EDS measured compositional profile along red arrow line in (a), with a dashed line indicating the ABF contrast line location.

In summary, rastering-beam Fe^{2+} ion irradiation of BL-Nb up to 220 dpa at 475°C induced dislocation loops at lower doses and tangled dislocations at higher doses. B2-NiAl precipitates were relatively stable under the irradiation and had a size of 11-14 nm and a number density of $1.5 \times 10^{22} - 7 \times 10^{21}$ m^{-3} from the irradiation depth of 0.3 – 0.6 µm to 1.3 – 1.6 µm. The alloy contains both coarse micron-scale and fine (~100 nm) Laves phase particles. The coarse Laves phase particles were amorphized, along with a slight composition change, at irradiation doses greater than ~30 dpa. In contrast, disintegration of the finer Laves particles was observed to occur at doses greater than ~70 dpa (≥ ~0.2 µm depth). The disintegration resulted in a noticeable composition change and also resulted in the nucleation of many new ultra-fine particles in ~8 nm, identified to be CrNb(N,C)-type Z-phase, which precipitated within a few hundreds of nanometers from the disintegrated finer Laves phase particles.

6.5 SUMMARY

The implantation of Al and Cu was revealed in the samples irradiated with a defocused beam at 350 and 475°C, respectively. The unexpected contamination prevents the direct comparison between this work and literatures. However, it is feasible to have direct comparisons between the samples under the same irradiation campaign in this work. The new ferritic-martensitic steels FTN1 and FTT1 showed comparable radiation resistance, superior to T91 irradiated under the same conditions. Although a direct comparison between the rastered-beam (TTZ2M and BL-Nb) and the defocused-beam (FTN1, FTT1, and T91) irradiated samples is not available, the radiation resistance of TTZ2M and BL-Nb was not significantly different from FTN1 and FTT1. A few points can be concluded below based on the post-irradiation examinations:

- **Grain structures:** Martensitic sub-boundaries were noticeably diminished in T91 by ion irradiation at 350°C and may also at 475°C that needs to be confirmed. In contrast, the grain structures in the other alloys, such as FTN1 (NA), FTT1 (TA), TTZ2M, and BL-Nb, were retained after the irradiations.
- **Dislocations:** Ion irradiation up to 250 dpa at 350°C generated larger dislocation loops in T91 (5.5 ± 2.6 nm) than that in FTN1 (NA) (3.0 ± 1.5 nm). The loop density in T91 (4.0×10^{22} m^{-3}) is lower than that in FTN1 (NA) (9×10^{22} m^{-3}). Larger but less dislocation loops (4.0 ± 2.7 nm, 4.1×10^{22} m^{-3}) were created in FTN1 (NA) by irradiation up to 250 dpa at 475°C. Dislocation loops were also observed in FTT1 (TA) irradiated under the same conditions, which were either comparable to

FTN1 (NA) or not able to be statistically quantified. Rastering-beam irradiation up to 220 dpa at 475°C generated similar dislocation loops in TTZ2M but more pronounced line dislocations than dislocation loops in BL-Nb.

- **Precipitates:** $M_{23}C_6$ and MX types of precipitates exist in the ferritic-martensitic steels FTN1, FTT1, TTZ2M, and T91, which did not show noticeable changes after ion irradiation up to 250 dpa at 350 and 475°C. However, Cr incorporation into (V,Nb)(C,N) MX-type precipitates was observed in T91 irradiated up to 250 dpa at 350°C, suggesting Z-phase formation. In contrast, precipitates of B2-NiAl and Laves phases exist in BL-Nb. The B2-NiAl was relatively stable after irradiation up to 220 dpa at 475°C. However, amorphization occurred in coarse Laves precipitates at damages > ~30 dpa and disintegration occurred in fine (~100 nm) Laves precipitates at damages > ~70 dpa. The disintegration of the fine Laves phase resulted in a noticeable composition change to the Laves phase and the formation of many new ultrafine (~8 nm) Z-phase type particles within a few hundreds of nanometers from the disintegrated fine Laves phase precipitates.
- **Cavities:** No cavities were found in all the samples irradiated under a defocused beam, e.g., FTN1 (NA), FTT1 (TA), and T91 irradiated up to 250 dpa at 350 and 475°C, or under a rastering beam, e.g., TTZ2M and BL-Nb irradiated up to 220 dpa at 475°C.
- **Radiation-hardening:** FTN1 (NA) showed better resistance to radiation-hardening at 350°C. Irradiation up to 250 dpa at 350°C increased nanoindentation hardness by 26.4 ± 7.8 % in FTN1 (NA), which is about half of the hardening by 55.7 ± 7.5 % in T91 (at indent displacement of 0.5 µm). In contrast, irradiation at 475°C did not noticeably change the hardness in either FTN1 (NA) or T91 under a defocused beam, while TTZ2M and BL-Nb showed slightly hardening, e.g., ~6 % at 1 µm, after irradiation up to 220 dpa at 475°C using a rastering beam.

7. CONCLUSIONS

After the justification and optimization of the developed thermodynamic database, five ferritic alloys and three ferritic-martensitic steels were designed. Property screening of their Vickers hardness, tensile properties, creep resistance, and ion irradiation hardening, together with microstructural characterization, led to the down-selection of one ferritic steel BL-Nb and one ferritic-martensitic steel TTZ2M for further investigation. Based on the TTZ2M, two large-scale ferritic-martensitic heats, i.e., FTT1 and FTN1, were produced at industrial steelmaking facilities, which are in contrast to the small laboratory heats BL-Nb and TTZ2M. Other than the standard normalization and tempering condition of the ferritic-martensitic steels, a heat-treated condition was explored for the FTT1 and FTN1, which is named as FTT1-T and FTN1-T, respectively. Two-step aging was applied to BL-Nb to favor the precipitation of Laves and B2-NiAl phases. The alloy compositions and heat treatment temperatures were guided by computational thermodynamics, as well as dilatometry for phase transformation temperature determination. Tensile, Charpy impact, and creep tests were conducted on samples of the steels in air, using a commercial heat of T91 as a reference. Microstructural characterization was primarily conducted using TEM and EDS with occasional uses of optical microscopy and SEM.

Tensile of the four steels indicated yield and tensile strength significantly higher than T91, which has up to ~170–350 MPa increases in yield strength at test temperatures from ~23 to 700°C. The strength enhancement was compromised by ductility with BL-Nb having the lowest total elongation at room temperature. The heat-treated condition FTT1-T and FTN1-T exhibited comparable tensile properties, with strength lower than the standard condition. The DBTT of TTZ2M, FTT1 and FTN1 are 20 to 60°C lower than that of Grade 91 (–47°C), while the DBTT of FTT1-T and FTN1-T are significantly below –150°C. The USE of the steels is ~23–50 J higher than that of Grade 91 (27 J). Ferritic steel BL-Nb exhibited the lowest impact toughness. Creep tests indicated the superior creep resistance of the four steels at 650°C compared to T91. The creep-rupture life ratio of the four steels over T91 at 650°C was in the range of 2.60 to 7.29 for the creep stresses of 100 and 120 MPa.

Microstructure characterizations of the creep-ruptured samples indicate noticeable recovery of T91 with diminished lath/block/packet sub-structures and reduced dislocations to the order of 10^{13} m^{-2}. The limited precipitates with a density on the order of 10^{19} m^{-3} in T91 would not effectively help retain the dislocations and the sub-structures at 650°C. In contrast, the large number of B2-NiAl and Laves $Fe_2(W,Nb)$ with comparable sizes on the order of 100 nm and a combined density on the order of 10^{20} m^{-3} after the creep tests helped retain sub-grain structures of BL-Nb, although the size/density and the chemistry of the precipitates slightly evolved during the creep tests. Similarly, the high-density (on the order of 10^{21} m^{-3}) of ultrafine (< ~20 nm) Ti-rich precipitates in TTZ2M and FTT1 helped retain the sub-structures and dislocations during the creep tests. Although the microstructure of FTN1 was not characterized because the sample is still running, FTN1 is expected to have a microstructure similar to FTT1 because of the superior creep resistance of FTN1. The microstructures of the untested condition indicated refined grains (~10 μm) for the heat-treated condition FTN1-T and FTT1-T compared to the general ~50 μm or larger prior-austenite grains of the standard condition (FTN1 and FTT1) with tempered martensite structures. The refined grains would explain the enhanced Charpy impact toughness of the heat-treated condition with compromised yield/tensile strength and creep resistance.

FTN1 and FTT1 showed comparable radiation resistance, superior to T91 irradiated under the same conditions at 350 and 475°C to a peak dose of 250 dpa, in terms of stabilities of grain structures, dislocations, precipitates, and radiation-hardening. For example, noticeably diminished martensitic sub-boundaries, formation of Z-phase by transformation from MX precipitates, and the greatest radiation-hardening were observed in T91. Although a direct comparison between the rastered-beam (TTZ2M and BL-Nb) and defocused-beam (FTN1, FTT1, and T91) irradiated samples is not available, the radiation resistance of TTZ2M and BL-Nb was not significantly different from the FTN1 and FTT1. However, BL-Nb did show instability of Lave phase, e.g., amorphization of coarse Laves precipitates and disintegration of fine (~100 nm) Laves precipitates to form ultrafine (~8 nm) Z-phase particles. Radiation induced cavities were not observed in the samples in this study.

The large-scale industrial heats FTN1 and FTT1 showed comparable or superior mechanical properties compared with the small laboratory heat TTZ2M, which suggest the property sustainability and scale-up fabrication feasibility of the developed ferritic-martensitic steels. The systematic study indicates the successful development of the new ferritic-martensitic steels FTN1 and FTT1.

REFERENCES

---

[1] S.J. Zinkle, L.L. Snead, Designing radiation resistance in materials for fusion energy, *Annual Review of Materials Research* 44 (2014) 241.

[2] B. Raj, M. Vijayalakshmi, R.J.M. Konings, T.R. Allen, R.E. Stoller, S. Yamanaka, Comprehensive Nuclear Materials, Elsevier, 2012.

[3] L. Tan, Y. Yang, Microstructure and mechanical properties of Laves phase-strengthened Fe-Cr-Zr alloys, *Metall. Mater. Trans. A* 46A (2015) 1188.

[4] L. Kaufman, H. Bernstein, Computer Calculations of Phase Diagrams, (New York: Academic Press), 1970.

[5] L. Tan, Development and Mechanical Results of Zr-Bearing Ferritic Steels, Oak Ridge National Laboratory (ORNL), ORNL/TM-2015/595, 2015.

[6] Y. Yang, T. Chen, L. Tan, Computational Thermodynamic Aided Design of Novel Ferritic Alloys, ORNL/TM-2016/229, June 30, 2016.

[7] T. Chen, Y. Yang. L. Tan, Phase stability in the Fe-rich Fe-Cr-Ni-Zr alloys, *Metall. Mater. Trans. A* 48A (2017) 5009.

[8] L. Tan, Y. Yang, K. Sridharan, Accelerated Development of Zr-Containing New Generation Ferritic Steels for Advanced Nuclear Reactors, ORNL/TM-2015/727, December 2015.

[9] NRIM Creep Data Sheet, No. 43, National Research Institute for Metals, Japan, 1996.

[10] W.R. Corwin, A.M. Hougland, Effect of specimen size and material condition on the Charpy impact properties of 9Cr-1Mo-V-Nb steel, in: W.R. Corwin, G.E. Lucas (Eds.), The Use of Small-scale Specimens for Testing Irradiated Material, ASTM STP 888, American Society for Testing and Materials, Philadelphia, 1986, p. 325.

[11] G.S. Was, Z. Jiao, E. Getto, K. Sun, A.M. Monterrosa, S.A. Maloy, O. Anderoglu, B.H. Sencer, M. Hackett, Emulation of reactor irradiation damage using ion beams, *Scripta Mater.* 88 (2014) 33.

[12] S.J. Zinkle, L.L. Snead, Opportunities and limitations for ion beams in radiation effects studies: bridging critical gaps between charged particle and neutron irradiations, *Scripta Mater.* 143 (2018) 154.

APPENDIX A. PUBLICATIONS

Journal Publications

Published

- T. Chen, C.M. Parish, Y. Yang, L. Tan, High-temperature strengthening mechanisms of Laves and B2 precipitates in a novel ferritic alloy, *Materials Science & Engineering A* 720 (2018) 110-116.
- T. Chen, Y. Yang, L. Tan, Phase Stability in the Fe-Rich Fe-Cr-Ni-Zr alloys, *Metallurgical and Materials Transactions A*, 48A (2017) 5009-5016.

Submitted

- L. He, L. Tan, K. Sridharan, Evolution of B2 and Laves phases in a ferritic steel under Fe^{2+} ion irradiation at 475°C, submitted to *Journal of Nuclear Materials* (2019).

Being prepared

- T. Chen, M. He, L. Tan, Y. Yang, B. Tyburska-Püschel, K. Sridharan, Evolution of microstructures and mechanical properties of Zr-containing ferritic alloys under self-ion irradiation.
- T. Chen, L. He, C.M. Parish, L. Tan, Y. Yang, Development of Laves and B2 manipulated advanced ferritic alloys.

Conference Presentations

- T. Chen, L. Tan, Y. Yang, R. He, B. Tyburska-Püschel, K. Sridharan, Correlation between the microstructure of precipitates and their mechanical contributions with and without radiation damage, TMS 2019.
- Y.-R. Lin, D.T. Hoelzer, L. Tan, S.J. Zinkle, Bubble formation in helium-implanted nanostructured 14YWT and CNA ferritic alloys at elevated temperatures, NuMat2018: The Nuclear Materials Conference, Seattle, WA, USA, Oct. 14–18, 2018.
- S.J. Zinkle, L. Tan, Y. Yang, Experimentally validated computational modeling of advanced alloys and radiation effects for nuclear energy applications, 2018 TMS Annual Meeting & Exhibition, Phoenix, AZ, USA, Mar. 11–15, 2018.
- T. Chen, L. Tan, Y. Yang, M. He, K. Sridharan, Development of Laves and B2 Manipulated Advanced Ferritic Alloys, 2018 TMS Annual Meeting & Exhibition, Phoenix, AZ, USA, Mar. 11–15, 2018.
- T. Chen, M.-R. He, L. Tan, Y. Yang, B. Tyburska-Püschel, K. Sridharan, Evolution of microstructures and mechanical properties of Zr-containing ferritic alloys under self-ion irradiation, TMS 2017 146th Annual Meeting & Exhibition, San Diego, CA, USA, Feb. 26 – Mar. 2, 2017.
- T. Chen, M.-R. He, L. Tan, Y. Yang, B. Tyburska-Püschel, K. Sridharan, Radiation response of a novel intermetallic-strengthened alloy, Materials Science & Technology 2016, Salt Lake City, UT, USA, Oct. 23–27, 2016.